UNIVERSIDAD POLITÉCNICA DE MADRID
ESCUELA TÉCNICA SUPERIOR DE INGENIEROS AERONÁUTICOS

TIME-RESOLVED EVOLUTION OF COHERENT STRUCTURES IN TURBULENT CHANNELS

Tesis Doctoral

Adrián Lozano Durán
Ingeniero Aeronáutico

Madrid, Junio 2015

DEPARTAMENTO DE MECÁNICA DE FLUIDOS Y PROPULSIÓN
AEROESPACIAL
ESCUELA TÉCNICA SUPERIOR DE INGENIEROS AERONÁUTICOS

TIME-RESOLVED EVOLUTION OF COHERENT STRUCTURES IN TURBULENT CHANNELS

Autor
Adrián Lozano Durán
Ingeniero Aeronáutico

Director de Tesis
Javier Jiménez Sendín
Doctor Ingeniero Aeronáutico

Madrid, Junio 2015

Sé breve en tus razonamientos, que ninguno hay gustoso si es largo.
Don Quijote de la Mancha

Index

Index **I**

Acknowledgments **V**

Nomenclature **VII**

Resumen **XV**

Summary **XIX**

1 Introduction **1**

- 1.1 Historical remarks 1
  - 1.1.1 The beginnings of turbulence 1
  - 1.1.2 Kolmogorov's theory 4
  - 1.1.3 Advances following Kolmogorov 6
- 1.2 Wall-bounded turbulence 7
- 1.3 Structural models in wall-bounded turbulence 11
- 1.4 Aims 15
- 1.5 Contents and organization of the thesis 16

2 Direct numerical simulations of turbulent channels up to $Re_\tau = 4200$ **19**

- 2.1 Introduction 19
- 2.2 Numerical experiments 20
- 2.3 Results 23
- 2.4 Conclusions 27

3 The 3D structure of momentum transfer in turbulent channels **29**

- 3.1 Introduction 29
- 3.2 Numerical experiments and identification method 32

3.3 Wall-attached and detached objects 37
  3.3.1 Detached structures. 39
  3.3.2 Attached structures. 43
3.4 Size and intensity of the attached Q^-s 44
  3.4.1 Effect of the computational domain 50
3.5 Shape of individual objects 51
  3.5.1 Topology of the coherent structures 56
3.6 Spatial organization 58
  3.6.1 Sweep-ejection pairs 62
  3.6.2 Large-scale organization 64
3.7 Conclusions 66

4 Time-resolved evolution of coherent structures 69
4.1 Introduction 69
4.2 Numerical experiments and identification of coherent structures 74
  4.2.1 Numerical experiments 74
  4.2.2 Identification of coherent structures 75
4.3 Tracking method 79
  4.3.1 Temporal sampling 79
  4.3.2 Steps of the tracking method 80
  4.3.3 Classification of branches according to their endpoints 84
4.4 Classification and geometry of branches 85
4.5 Temporal evolution. 89
  4.5.1 Lifetimes 89
  4.5.2 Birth and death, and vertical evolution 93
  4.5.3 Relative position of branch creation 96
  4.5.4 Advection velocities 100
4.6 Conclusions 103
4.A Details and validation of the tracking method 105
  4.A.1 Spurious connections and branches 105
  4.A.2 Validation of the tracking method 107
4.B Effect of the threshold and time step 107

5 The turbulent cascade in terms of coherent structures 111
5.1 Introduction 111
5.2 Secondary branches and graphs 112

5.3 Definition of a cascade of eddies 113
5.4 Results 114
5.5 Conclusions 120

6 Conclusions and future work **123**

References **129**

Acknowledgments

Now that I stand in front of this finished work, I realize how important is to be surrounded by those who support you both academically and emotionally.

First, I am very grateful to my advisor Javier Jiménez. Javier did not teach me turbulence, that I learned it from the books. He taught me something much more valuable, something I never found in books. He taught me to think.

I am deeply indebted to my family, my parents Carmen and Victor, my brother Alberto, and Pili, for their support and always believe that I am able to achieve any goal that I pursue. Alba has always stood by my side and this work would not be the same if it was not for her. She knows that I do not share my concerns very often but, for some magical reason, she does know when I need her love and support.

During these years, I have been accompanied by colleagues and visitors in the Fluid Mechanics Lab., who were always willing to encourage me, have interesting discussions, or simply lend me a hand when I needed it. They were Guillem, Yoshi, Pablo, Juan, Ricardo, Ayse, Florian, Julio, Alberto, Miguel P., Fer, Siwei, Kike, Miguel H., Jose, Atsushi, Yvan, Jason, Cecilia, Markus, Marios... I am grateful to them for sharing many wonderful moments with me during all these years. I would also like to mention my flatmates and good friends Carlos, Jose Alberto and Aleix who, maybe without knowing it, motivated me to strive and work harder.

The present research was developed in the Department of Fluid Mechanics and Aerospace Propulsion at the Technical University of Madrid, and was made possible thanks to the support by CICYT, under grant TRA2009-11498, and by the European Research Council, under grant ERC-2010.AdG-20100224. I would also like to acknowledge the financial support of the Spanish Ministry of Education through an FPI scholarship. The computations were made possible by generous grants of computer time from CeSViMa (Centro de Supercomputación y Visualización de Madrid) and BSC (Barcelona Supercomputing Centre).

Nomenclature

Mathematical operators

$(\cdot)^+$	Variable in wall-units, normalized using u_τ and ν
$(\cdot)'$	Root mean square of $(\cdot)$
$\langle(\cdot)\rangle$	Average of $(\cdot)$ in time and in the homogeneous spatial directions
$\overline{(\cdot)}$	Ensemble average of $(\cdot)$
$\langle\cdot\rangle_B$	Time-average over the branch lifetime of $(\cdot)$
∇	Nabla operator

Greek symbols

α	Fractal dimension for coherent structures
α_t	Thresholding parameter for vortex clusters
α_c	Fractal dimension for vortex clusters
α_Q	Fractal dimension for Qs
$\overline{\delta(u^n)}$	Second-order structure function of the velocity increments
δ_x	Streamwise relative position of different structures
δ_z	Spanwise relative position of different structures
Δ	Diagonal length of the circumscribed box to a structure
Δ_b	Diagonal length of the circumscribed box to the largest structure involved in a merger or a split
Δ_m	Diagonal length of the circumscribed box to the medium-size structure involved in a merger or a split
Δ_s	Diagonal length of the circumscribed box to the smallest structure involved in a merger or a split
Δt_s	Time step between contiguous snapshots to track structures in time

ΔU	Difference between the phase velocities at the top and at the bottom of an attached eddy
ΔV	Volume difference between intersecting structures
Δ_x	Streamwise length of the coherent structure
Δx	Grid size in the streamwise direction
Δ_y	Wall-normal length of the coherent structure
Δy	Grid size in the wall-normal direction
Δ_z	Spanwise length of the coherent structure
Δz	Grid size in the spanwise direction
ε	Kinetic-energy dissipation rate
η	Kolmogorov length scale
θ	Boundary layer momentum thickness
κ	von Kármán constant
λ	Taylor microscale
λ_x	Wavelength in the streamwise direction
λ_z	Wavelength in the spanwise direction
ν	Kinematic viscosity
Ξ	Logarithmic layer diagnostic function
ρ	Density of the fluid
ρ_h	Density of holes per unit volume in a structure
τ	Tangential Reynolds stress
τ_m	Average tangential Reynolds stress of the flow within the coherent structure $(uv)_m$
τ_w	Tangential Reynolds stress at the wall
ϕ_{uu}	Premultiplied spectrum of the streamwise velocity
Ω	Domain of the constituent points of the structure

Roman symbols

B and B_1	Constants for the law of the wall
D	Discriminant of the velocity gradient tensor
d	Wall-parallel diagonal length of the circumscribed box to a structure
D_f	Fractal dimension of the coherent structures
E	Spectral density of the turbulent kinetic energy
E_{uu}	Spectral density of the streamwise velocity

E_{uv}	Cospectrum density of u–v
f	Fraction of the number of primary branches that split or merge at least once in their lives
f_A	Fraction of the volume of cluster boxes that is filled by intersecting boxes of Qs
g	Genus of a coherent structure
h	Channel half-height
H	Hyperbolic-hole size associated with $u'(y)v'(y)$
$\widetilde{H}$	Hyperbolic-hole size associated with $\lvert\bar{\tau}\rvert(y)$
$\hat{H}$	Hyperbolic-hole size associated with $\tau'(y)$
J	Probability density function
k	Wavenumber for isotropic turbulence
K	Turbulent kinetic energy
k_x	Streamwise wavenumber
k_z	Spanwise wavenumber
l	Diagonal length of the circumscribed box to a structure averaged over its branch
l_C	Corrsin's length scale
l_x	Time-averaged streamwise length of the structures over the branch lifetime
l_y	Time-averaged wall-normal length of the structures over the branch lifetime
l_z	Time-averaged spanwise length of the structures over the branch lifetime
L_x	Length of the channel in the streamwise direction
L_z	Length of the channel in the spanwise direction
L_ε	Integral length scale
L_Q	Length of Qs fragments
L_{tot}	Total length of Qs fragments
n	Average number of splits or mergers in a branch
n_{br}	Number density per unit height, wall area and total time, of branches belonging to tall attached Q^- branches
n_I	Number of intersecting structures with random streamwise lines
n_{ob}	Number density per unit height, wall area and total time,

	of structures belonging to tall attached Q$^-$ branches
N	Total number of structures identified
N_b	Number of branches per graph
N_c	Number of boxes counted with the box-counting method
N_F	Number of fields used to accumulate statistics
N_{fk}	Fraction of the number of Qk
N_Q	Numbers of Q$^-$s
N_V	Numbers of vortex clusters
N_B^Q	Number of branches for Qs
N_G^Q	Number of graphs for Qs
N_S^Q	Number of splits for Qs
N_M^Q	Number of mergers for Qs
N_I^Q	Number of isolated Qs
N_x	Number of collocation points in the streamwise direction
N_y	Number of collocation points in the wall-normal direction
N_z	Number of collocation points in the spanwise direction
p	Pressure
P	Average pressure
q	Magnitude of the velocity fluctuations
r	Ratio of the volumes of direct and inverse cascade as a function of Δ_s and Δ_b
r_B	Ratio of the number of events for direct and inverse cascade
r_1	Inner length of the coherent structures or estimated thickness
r_2	Intermediate length of the coherent structures
r_3	Outer length of the coherent structures
$R_{\tau\tau}$	Correlation function of τ
Re	Reynolds number
Re_τ	Friction Reynolds number, $Re_\tau = h^+$
Re_l	Reynolds number of an eddy of size l
Re_λ	Taylor-microscale Reynolds number

RS_τ	Fraction of the total tangential Reynolds stress carried by the coherent structures
S	Mean shear, $\partial_y U$
t	Time
t_n	Time at the snapshot number n
t_η	Kolmogorov time-scale
T	Lifetime of coherent structures
T_I	Time elapsed before structures split (or merge) into two similar fragments
T_s	Total time simulated to accumulate statistics
u	Fluctuating velocity in the streamwise direction
u_c	Centerline fluctuating streamwise velocity
u_l	Characteristic velocity of an eddy of size l
u_L	Characteristic velocity of the large scale eddies
u_m	Average streamwise velocity of the flow within the coherent structure
u_t	Streamwise velocity of the flow
u_η	Kolmogorov velocity-scale
$\vec{u}$	Fluctuating velocity vector containing u, v, and w
u_τ	Friction velocity
$(uv)_m$	Average tangential Reynolds stress of the flow within the coherent structure
U	Mean streamwise velocity profile
U_c	Mean centerline streamwise velocity
U_s	Streamwise advection velocity of the coherent structures
U_∞	Free-stream velocity for boundary layers
v	Fluctuating velocity in the wall-normal direction
v_m	Average wall-normal velocity of the flow within the coherent structure
v_t	Wall-normal velocity of the flow
V	Volume of a coherent structure
V_{lar}	Volume of the largest structure identified
V_{tot}	Total volume of the structures identified

V_I^Q	Volume occupied by all isolated Qs
V_T^Q	Volume occupied by all Qs
V_i	Overlapped volume between structures at contiguous times
V_{fk}	Fraction of the channel volume occupied by Qk
v_s	Wall-normal advection velocity of the coherent structures
V_b	Time-averaged volume of the structures over the branch lifetime
V_Q	Volume of Qs
V_{sd}	Volume of direct cascade in a branch
V_{si}	Volume of inverse cascade in a branch
w	Fluctuating velocity in the spanwise direction
w_t	Spanwise velocity of the flow
x	Streamwise direction
x_b	Streamwise coordinates of the center of a newborn structure
x_c	Streamwise coordinate of the center of an existing structure
$\boldsymbol{x}$	Position vector containing x, y and z
y	Wall-normal direction
y_b	Wall-normal height of death tall attached primary branches
y_c	Time-averaged wall-normal center of gravity over the branch lifetime
y_d	Wall-normal height of newborn tall attached primary branches
y_{min}	Minimum distance to the wall of a structure
y_{max}	Maximum distance to the wall of a structure
Y_c	Center of gravity of a structure, $(y_{min} + y_{max})/2$
z	Spanwise direction
z_c	Spanwise coordinate of the center of an existing structure
z_b	Spanwise coordinates of the center of a newborn structure

Abbreviations

ASL	Atmospheric surface layer
CFL	Courant-Friedrichs-Lewy number
DNS	Direct numerical simulation
LES	Large-eddy simulation
p.d.f.	Probability density function
Q1	Outward interaction
Q2	Ejections
Q3	Inward interaction
Q4	Sweeps
Qs	Coherent structures based on uv
Q^-s	‘Gradient’ structures Q2 and Q4
Q^+s	‘Counter-gradient’ structures Q1 and Q3
r.m.s.	Root-mean-square

Resumen

El objetivo de esta tesis es estudiar la dinámica de la capa logarítmica de flujos turbulentos de pared. En concreto, proponemos un nuevo modelo estructural utilizando diferentes tipos de estructuras coherentes: *sweeps*, eyecciones, grupos de vorticidad y *streaks*. La herramienta utilizada es la simulación numérica directa de canales turbulentos.

Desde los primeros trabajos de Theodorsen (1952), las estructuras coherentes han jugado un papel fundamental para entender la organización y dinámica de los flujos turbulentos. A día de hoy, datos procedentes de simulaciones numéricas directas obtenidas en instantes no contiguos permiten estudiar las propiedades fundamentales de las estructuras coherentes tridimensionales desde un punto de vista estadístico. Sin embargo, la dinámica no puede ser entendida en detalle utilizando sólo instantes aislados en el tiempo, sino que es necesario seguir de forma contínua las estructuras. Aunque existen algunos estudios sobre la evolución temporal de las estructuras más pequeñas a números de Reynolds moderados, por ejemplo Robinson (1991), todavía no se ha realizado un estudio completo a altos números de Reynolds y para todas las escalas presentes de la capa logarítmica. El objetivo de esta tesis es llevar a cabo dicho análisis.

Los problemas más interesantes los encontramos en la región logarítmica, donde residen las cascadas de vorticidad, energía y momento. Existen varios modelos que intentan explicar la organización de los flujos turbulentos en dicha región. Uno de los más extendidos fue propuesto por Adrian *et al.* (2000) a través de observaciones experimentales y considerando como elemento fundamental paquetes de vórtices con forma de horquilla que actúan de forma cooperativa para generar rampas de bajo momento. Un modelo alternativo fué ideado por del Álamo & Jiménez (2006) utilizando datos numéricos. Basado también en grupos de vorticidad, planteaba un escenario mucho más desorganizado y con estructuras sin forma de horquilla. Aunque los dos modelos son cinemáticamente similares, no lo son desde el punto de vista dinámico, en concreto en lo que se refiere a la importancia que juega la pared en la creación y vida de las estructuras. Otro punto importante aún sin resolver se refiere al modelo de cascada turbulenta propuesto por Kolmogorov (1941*b*), y su relación con estructuras coherentes medibles en el flujo.

Para dar respuesta a las preguntas anteriores, hemos desarrollado un nuevo método que permite seguir estructuras coherentes en el tiempo y lo hemos aplicado a simulaciones numéricas de canales turbulentos con números de Reynolds lo suficientemente altos como para tener un rango de escalas no trivial y con dominios computacionales lo suficientemente grandes como para representar de forma correcta la dinámica de la capa logarítmica. Nuestros esfuerzos se han desarrollado en cuatro pasos.

En primer lugar, hemos realizado una campaña de simulaciones numéricas directas a diferentes números de Reynolds y tamaños de cajas para evaluar el efecto del dominio computacional en las estadísticas de primer orden y el espectro. A partir de los resultados obtenidos, hemos concluido que simulaciones con cajas de longitud 2π y ancho π veces la semi-altura del canal son lo suficientemente grandes para reproducir correctamente las interacciones entre estructuras coherentes de la capa logarítmica y el resto de escalas. Estas simulaciones son utilizadas como punto de partida en los siguientes análisis.

En segundo lugar, las estructuras coherentes correspondientes a regiones con esfuerzos de Reynolds tangenciales intensos (Qs) en un canal turbulento han sido estudiadas extendiendo a tres dimensiones el análisis de cuadrantes, con especial énfasis en la capa logarítmica y la región exterior. Las estructuras coherentes han sido identificadas como regiones contiguas del espacio donde los esfuerzos de Reynolds tangenciales son más intensos que un cierto nivel. Los resultados muestran que los Qs separados de la pared están orientados de forma isótropa y su contribución neta al esfuerzo de Reynolds medio es nula. La mayor contribución la realiza una familia de estructuras de mayor tamaño y autosemejantes cuya parte inferior está muy cerca de la pared (ligada a la pared), con una geometría compleja y dimensión fractal ≈ 2. Estas estructuras tienen una forma similar a una 'esponja de placas', en comparación con los grupos de vorticidad que tienen forma de 'esponja de cuerdas'. Aunque el número de objetos decae al alejarnos de la pared, la fracción de esfuerzos de Reynolds que contienen es independiente de su altura, y gran parte reside en unas pocas estructuras que se extienden más allá del centro del canal, como en las grandes estructuras propuestas por otros autores. Las estructuras dominantes en la capa logarítmica son parejas de sweeps y eyecciones uno al lado del otro y con grupos de vorticidad asociados que comparten las dimensiones y esfuerzos con los remolinos ligados a la pared propuestos por Townsend.

En tercer lugar, hemos estudiado la evolución temporal de Qs y grupos de vorticidad usando las simulaciones numéricas directas presentadas anteriormente hasta números de Reynolds $Re_\tau = 4200$ (Reynolds de fricción). Las estructuras fueron identificadas siguiendo el proceso descrito en el párrafo anterior y después seguidas en el tiempo. A través de la intersećión geométrica de estructuras pertenecientes a instantes de tiempo contiguos, hemos creado grafos de conexiones temporales entre todos los objetos y, a partir de ahí, definido ramas primarias y secundarias, de tal forma que cada rama representa la evolución temporal de una estructura coherente. Una vez que las evoluciones están adecuadamente organizadas, proporcionan toda la información necesaria para caracterizar la historia de las estructuras desde su nacimiento hasta su muerte. Los resultados muestran que las estructuras nacen a todas las distancias de la pared, pero con mayor probabilidad cerca de ella, donde la cortadura es más intensa. La mayoría mantienen tamaños pequeños y no viven mucho tiempo, sin embargo, existe una familia de estructuras que crecen lo suficiente como para ligarse a la pared y extenderse a lo largo de la capa logarítmica convirtiéndose en las estructuras observas anteriormente y descritas por Townsend. Estas estructuras son geométricamente autosemejantes con tiempos de vida proporcionales a su tamaño. La mayoría alcanzan tamaños por encima de la escala de Corrsin, y por ello, su dinámica está controlada por la cortadura media. Los resultados también muestran que las eyecciones se alejan de la pared con velocidad media u_τ (velocidad de fricción) y su base se liga a la pared muy rápidamente al inicio de sus vidas. Por el contrario, los sweeps se mueven hacia la pared con velocidad $-u_\tau$ y se ligan a ella más tarde. En ambos casos, los objetos permanecen ligados a la pared durante 2/3 de sus vidas. En la dirección de la corriente, las estructuras se desplazan a velocidades cercanas a la convección media del flujo y son deformadas por la cortadura.

Finalmente, hemos interpretado la cascada turbulenta, no sólo como una forma conceptual de organizar el flujo, sino como un proceso físico en el cual las estructuras coherentes se unen y se rompen. El volumen de una estructura cambia de forma suave, cuando no se une ni rompe, o lo hace de forma repentina en caso contrario. Los procesos de unión y rotura pueden entenderse como una cascada directa (roturas) o inversa (uniones), siguiendo el concepto de cascada de remolinos ideado por Richardson (1920) y Obukhov (1941). El análisis de los datos muestra que las estructuras con tamaños menores a 30η (unidades de Kolmogorov) nunca se unen ni rompen, es decir, no experimentan el proceso de cascada. Por el contrario, aquellas mayores a 100η siempre se rompen o unen al menos una vez en su vida. En estos casos, el volumen total ganado y perdido es una fracción importante del volumen medio de la estructura implicada, con una tendencia ligeramente mayor a romperse (cascada directa) que a unirse (cascade inversa). La mayor parte de interacciones entre ramas se debe a roturas o uniones de fragmentos muy pequeños en la escala de Kolmogorov con estructuras más grandes, aunque el efecto de fragmentos de mayor tamaño no es despreciable. También hemos encontrado que las roturas tienen a ocurrir al final de la vida de la estructura y las uniones al principio. Aunque los resultados para la cascada directa e inversa no son idénticos, son muy simétricos, lo que sugiere un alto grado de reversibilidad en el proceso de cascada.

Summary

The purpose of the present thesis is to study the dynamics of the logarithmic layer of wall-bounded turbulent flows. Specifically, to propose a new structural model based on four different coherent structures: sweeps, ejections, clusters of vortices and velocity streaks. The tool used is the direct numerical simulation of time-resolved turbulent channels.

Since the first work by Theodorsen (1952), coherent structures have played an important role in the understanding of turbulence organization and its dynamics. Nowadays, data from individual snapshots of direct numerical simulations allow to study the three-dimensional statistical properties of those objects, but their dynamics can only be fully understood by tracking them in time. Although the temporal evolution has already been studied for small structures at moderate Reynolds numbers, e.g., Robinson (1991), a temporal analysis of three-dimensional structures spanning from the smallest to the largest scales across the logarithmic layer has yet to be performed and is the goal of the present thesis.

The most interesting problems lie in the logarithmic region, which is the seat of cascades of vorticity, energy, and momentum. Different models involving coherent structures have been proposed to represent the organization of wall-bounded turbulent flows in the logarithmic layer. One of the most extended ones was conceived by Adrian *et al.* (2000) and built on packets of hairpins that grow from the wall and work cooperatively to generate low-momentum ramps. A different view was presented by del Álamo & Jiménez (2006), who extracted coherent vortical structures from DNSs and proposed a less organized scenario. Although the two models are kinematically fairly similar, they have important dynamical differences, mostly regarding the relevance of the wall. Another open question is whether such a model can be used to explain the cascade process proposed by Kolmogorov (1941*b*) in terms of coherent structures. The challenge would be to identify coherent structures undergoing a turbulent cascade that can be quantified.

To gain a better insight into the previous questions, we have developed a novel method to track coherent structures in time, and used it to characterize the temporal evolutions of

eddies in turbulent channels with Reynolds numbers high enough to include a non-trivial range of length scales, and computational domains sufficiently long and wide to reproduce correctly the dynamics of the logarithmic layer. Our efforts have followed four steps.

First, we have conducted a campaign of direct numerical simulations of turbulent channels at different Reynolds numbers and box sizes, and assessed the effect of the computational domain in the one-point statistics and spectra. From the results, we have concluded that computational domains with streamwise and spanwise sizes 2π and π times the half-height of the channel, respectively, are large enough to accurately capture the dynamical interactions between structures in the logarithmic layer and the rest of the scales. These simulations are used in the subsequent chapters.

Second, the three-dimensional structures of intense tangential Reynolds stress in plane turbulent channels (Qs) have been studied by extending the classical quadrant analysis to three dimensions, with emphasis on the logarithmic and outer layers. The eddies are identified as connected regions of intense tangential Reynolds stress. Qs are then classified according to their streamwise and wall-normal fluctuating velocities as inward interactions, outward interactions, sweeps and ejections. It is found that wall-detached Qs are isotropically oriented background stress fluctuations, common to most turbulent flows, and do not contribute to the mean stress. Most of the stress is carried by a self-similar family of larger wall-attached Qs, increasingly complex away from the wall, with fractal dimensions ≈ 2. They have shapes similar to 'sponges of flakes', while vortex clusters resemble 'sponges of strings'. Although their number decays away from the wall, the fraction of the stress that they carry is independent of their heights, and a substantial part resides in a few objects extending beyond the centerline, reminiscent of the very large scale motions of several authors. The predominant logarithmic-layer structures are side-by-side pairs of sweeps and ejections, with an associated vortex cluster, and dimensions and stresses similar to Townsend's conjectured wall-attached eddies.

Third, the temporal evolution of Qs and vortex clusters are studied using time-resolved DNS data up to $Re_\tau = 4200$ (friction Reynolds number). The eddies are identified following the procedure presented above, and then tracked in time. From the geometric intersection of structures in consecutive fields, we have built temporal connection graphs of all the objects, and defined main and secondary branches in a way that each branch represents the temporal evolution of one coherent structure. Once these evolutions are properly organized, they provide the necessary information to characterize eddies from birth to death. The results show that the eddies are born at all distances from the wall, although with higher probability near it, where the shear is strongest. Most of them stay small and do not last for long times. However, there is a family of eddies that become large enough to attach to the wall while they reach into the logarithmic layer, and become the wall-attached structures previously observed in instantaneous flow fields. They are geometrically self-similar, with sizes and lifetimes proportional to their distance from the wall. Most of them achieve lengths well above the Corrsin' scale, and hence, their dynamics are controlled by the mean shear. Eddies associated with ejections move away from the wall with an average velocity u_τ (friction velocity), and their base attaches very fast at the beginning of their lives. Conversely, sweeps move towards the wall at $-u_\tau$, and attach later. In both cases, they remain attached for 2/3 of their lives. In the streamwise direction, eddies are advected and deformed by the local mean velocity.

Finally, we interpret the turbulent cascade not only as a way to conceptualize the flow, but as an actual physical process in which coherent structures merge and split. The volume of an eddy can change either smoothly, when they are not merging or splitting, or through sudden changes. The processes of merging and splitting can be thought of as a direct (when splitting) or an inverse (when merging) cascade, following the ideas envisioned by Richardson (1920) and Obukhov (1941). It is observed that there is a minimum length of 30η (Kolmogorov units) above which mergers and splits begin to be important. Moreover, all eddies above 100η split and merge at least once in their lives. In those cases, the total volume gained and lost is a substantial fraction of the average volume of the structure involved, with slightly more splits (direct cascade) than mergers. Most branch interactions are found to be the shedding or absorption of Kolmogorov-scale fragments by larger structures, but more balanced splits or mergers spanning a wide range of scales are also found to be important. The results show that splits are more probable at the end of the life of the eddy, while mergers take place at the beginning of the life. Although the results for the direct and the inverse cascades are not identical, they are found to be very symmetric, which suggests a high degree of reversibility of the cascade process.

Chapter 1

Introduction

The key role of turbulence in both science and engineering is doubtless. From a practical point of view, turbulent flows have a wide range of applications that are found in many technological problems, such as the flow in turbines, meteorological predictions, combustion or transport of fluid through ducts. Turbulence results in drag on vehicles such as planes, cars or ships, and controls the heat transfer and mixing of pollutants in machines and the environment.

The present thesis addresses a number of outstanding questions about the physics of turbulence that are crucial to improve our understanding about such an important phenomena.

1.1 Historical remarks

1.1.1 The beginnings of turbulence

Turbulence was recognized as a different flow regime several centuries ago. There are even prehistorical paintings where water and wind are represented by spirals which mimic the disorganized nature of these two elements. In both ancient Greek ($\tau\acute{\upsilon}\rho\beta\eta$) and Latin (*turba-æ*) existed specific words from where the current concept of turbulence derived. However, these former words were related to chaos and turmoil rather than to a flow regime. In Spanish, Gonzalo de Berceo (1197–1264) used the term *turbare* to describe adverse weather, and Leonardo da Vinci (1452–1519) sketched disordered water and wind in many of his paintings. The chaotic nature of fluids has been recurrent in art. Two representative examples are the *Starry Night* (1889) by Vicent Van Gogh and *The Great Wave Off Kanagawa* (1832) by Katsushika Hokusai (see figure 1.1).

The scientific study of turbulence began in the mid-nineteenth century with Poiseuille

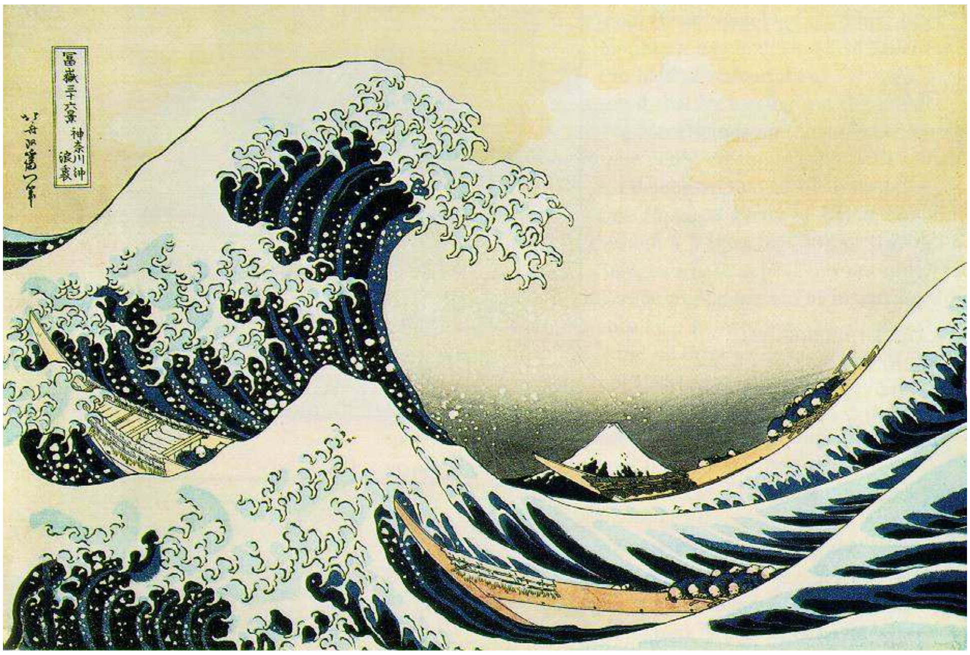

Figure 1.1: *The Great Wave Off Kanagawa* by Katsushika Hokusai.

(1846) and Hagen (1839), who analyzed the laminar regime of simple flows and measured the relation between viscosity and temperature. Hagen (1854) and Darcy (1857), independently, studied the pressure drop in ducts and found two separate components. The former changed linearly with the flow velocity and was proportional to the kinematic viscosity of the fluid. The second changed quadratically with the velocity and was independent of the viscosity. The latter component caused some controversy since it suggested that the flow was able to organize in such a way that the dissipation of energy was never zero even if the viscosity was. This posed a paradox inasmuch as the dissipation of energy per units mass and time in an incompressible flow is

$$\varepsilon = \nu \overline{|\nabla u|^2}, \tag{1.1}$$

where ν is the kinematic viscosity, u the velocity of the flow, ∇ the gradient operator, and the overline denotes ensemble average. The observations of Hagen (1854) and Darcy (1857) and relation (1.1) implied that, in a turbulent flow, the velocity gradients become singular when the viscosity tends to zero, and hence, a certain amount of dissipation remains. This finding turned out to be a fundamental feature of turbulent flows.

In 1877, Boussinesq classified the flow regimes for the first time as turbulent or laminar, and noticed that the momentum transport was larger in the former. Based on his observations, he proposed a linear relation between terms responsible for the momentum transfer and the strain through a certain coefficient referred to as eddy viscosity. This understanding was crucial and the enhanced transport of momentum was recognized as a distinctive property of turbulence.

The experiments by Reynolds (1894) are considered among the most influential results in the study of turbulence. Using experimental data, Reynolds identified the non-dimensional parameter responsible for the transition from laminar to turbulence in incompressible flows and simple geometries. The parameter is now known as the *Reynolds number* and represents the ratio of inertial and viscous effects of the flow. Reynolds went one step further and realized that attempting to understand turbulence in all its detail was not a very fruitful approach. For that reason, he made use of statistical tools and separated the flow velocity in two parts, the average component and the fluctuating one. The average component obeys the *Reynolds–averaged Navier–Stokes equations* which, compared to the Navier–Stokes ones, contain additional terms known as *Reynolds stresses.* These terms depend on the fluctuating velocities and can not be obtained directly from the average quantities. Nevertheless, they have been modeled on many occasions resulting in the so called *closure problem.* The Reynolds' decomposition introduced a great simplification and its use persist up to this day.

About the same time that Reynolds proposed a statistical description of turbulence, Poincaré (1899) found that simple non-linear systems were able to show chaotic behaviors even if they were governed by deterministic differential equations. It was later on when Lorenz (1963) proposed a link between deterministic chaos and turbulence after his work on weather prediction in 1961.

After the works by Reynolds, most of the studies tackled the closure problem using different statistical models with varying degrees of success. The first important breakthrough was obtained by Prandtl (1925) with the so-called *mixing length theory* first introduced by Boussinesq (1877). The theory followed the ideas of the successful Kinetic Theory of Gases and proposed the analogy between turbulent eddies and molecules, which allowed to build the length and velocity scales required to estimate the eddy viscosity. At the same time, Richardson (1920) suggested a multiscale description of turbulence and postulated that the energy is injected in the largest scales or eddies, that break into smaller ones due to flow instabilities. The process is self-similarly repeated, producing eddies smaller and smaller until they are dissipated by viscosity. He famously summarized turbulence in rhyming verse in *Weather Prediction by Numerical Process* (p 66):

> Big whirls have little whirls that feed on their velocity,
> and little whirls have lesser whirls and so on to viscosity.

Although little rigorous, this phenomenological picture has been very influential on later works.

Some of the most relevant advances during the 1930s were due to G. I. Taylor, who introduced more sophisticated and rigorous mathematical tools such as velocity correlations and Fourier transforms, both of them intensively used up to the present day. In his work, Taylor (1935) introduced the concept of isotropic turbulence and showed that its statistical properties resemble those of a flow moving across a grid in a experimental wind tunnel. The idea of isotropic turbulence have played a key role in the understanding of turbulence since it is the most simplified turbulence set-up that can be considered reasonable realistic. A significant theoretical result related to isotropic turbulence was published by von Kármán & Howarth (1938), who derived the equation describing the energy transfer among eddies located at difference scales known as the *Kármán-Howarth equation*. Another important contribution due to Taylor was the *frozen turbulence hypothesis*, which allows conversion between spatial and temporal data, and was especially relevant for analyzing one-point experimental measurements.

1.1.2 Kolmogorov's theory

A.N Kolmogorov developed a statistical theory in a series of short papers (Kolmogorov, 1941*b*,*a*) that has become one of the major achievements in turbulence. Its simplicity and ability to make simple but fundamental predictions have contributed enormously to its success.

Kolmogorov considered an isotropic turbulent flow, and hypothesize that the Reynolds number of the largest scales with characteristic length L_ε and velocity u_L is so high that they are barely affected by the viscous terms. He argued that the external forces act on the largest scales, that serves as the energy input to the flow. Since these scales can not dissipate the energy, this has to be entirely transfer to the smaller ones. Therefore, following the ideas proposed by Richardson (1920), Kolmogorov considered turbulence as a multiscale phenomena where the energy is transfer among eddies which repeatedly break into smaller ones until the effect of the viscosity acts on them. The energy is finally dissipated in this last step. This transfer of energy among scales is known as the *turbulent energy cascade.*

In particular, the theory states that the energy transfer per unit mass and time is proportional to u_l^2/t_l, where u_l and t_l are respectively the characteristic velocity and time-scale of an eddy of size l. Assuming that the characteristic time-scale is $t_l \sim l/u_l$, the energy flux at scale l is $\sim u_l^3/l$. For a statistically stationary state and for eddies large enough to be independent of the viscosity, the cascade is in equilibrium and the energy flux must balance the dissipation

$$\varepsilon \sim u_l^3/l. \tag{1.2}$$

Following the previous definitions, the characteristic velocity of eddies with size l is

$$u_l \sim (u_L^3 l/L_\varepsilon)^{1/3} \sim (\varepsilon l)^{1/3}, \tag{1.3}$$

and from dimensional arguments, the associated one-dimensional energy spectrum follows

$$E_{uu}(k) \sim \varepsilon^{2/3} k^{-5/3}, \tag{1.4}$$

which is known as Kolmogorov's 5/3 law, with $k \sim 1/l$ the wavenumber.

On the basis of the arguments above, the theory defines three different regions associated with four characteristic length-scales. From large to small:

- Integral scale L_ε: represents the largest characteristic length of the flow where the injection of energy from the external forces to the flow occurs.

- Inertial range l: all the intermediate scales which are not directly influenced by the injection of energy nor the dissipation, $L_\varepsilon \gg l \gg \eta$, where η is defined below. In this range, equation (1.2) is satisfied and the energy is transferred without loss.

- Kolmogorov's length scale η: length at which the viscous and inertial effects are of the same order, i.e., the Reynolds number of the eddies is $Re_l \sim (\varepsilon l^4/\nu^3)^{1/3} \sim 1$ resulting in $\eta = \left(\frac{\nu^3}{\varepsilon}\right)^{1/4}$.

- Dissipative range: those scales below the Kolmogorov's scale, and hence, dominated by the viscous effects.

The characteristic velocity associated with the Kolmogorov' length-scale is

$$u_\eta = (\nu\varepsilon)^{1/4}, \tag{1.5}$$

and the velocity gradient, $u_\eta/\eta \sim (\varepsilon/\nu)^{1/2}$, becomes infinite when ν tends to zero. Substituting the previous gradient in equation (1.1) results in a dissipation rate independent of the viscosity as predicted by Hagen and Darcy.

It is important to note that Kolmogorov derived the statistical consequences of the energy cascade, but that does not imply that the phenomenological view presented above is actually followed by the flow, even if the predictions are reasonable well satisfied when compared with experiments.

1.1.3 Advances following Kolmogorov

The theory by Kolmogorov (1941*b*,*a*) is considered a great success but it also presents serious shortcomings. For instance, it assumes that the velocity gradients are uniformly distributed in space as the scale decreases, but Batchelor & Townsend (1949) observed that this hypothesis is not completely fulfilled, which was referred to as *intermittency*. Kolmogorov (1962) himself modified his theory to account for this effect. More refined models appeared to explain this phenomenon. One of the most widespread ones was proposed by Frisch *et al.* (1978) and later improvements were developed by Frisch (1995) and Jiménez (2000). These models rely on multiplicative cascades where the size of the structures decreases by a constant factor and velocities are multiplied by a random one.

The experimental techniques developed very fast during 1960s and thereafter, which allowed more sophisticated experiments and results. The experiments and flow visualizations by Kline *et al.* (1967), Corino & Brodkey (1969), and Brown & Roshko (1974) are a milestone in the way turbulent flows are understood, and were the beginning of a new deterministic approach to turbulence based on coherent structures in contrast to the statistical theories that dominated since Kolmogorov's papers. All these new works identified spatial and temporal coherent regions in the flow of mixing and boundary layers, which were promptly considered essential features present in all turbulent flows. Nowadays, coherent structures play a fundamental role in our understanding of turbulence and there are several structural models that attempt to explain the dynamics of the flow. Some of these models are discussed in the next section for wall-bounded turbulence.

With the emergence and quick development of computers in the last decades, numerical solutions of the Navier–Stokes equations have become one of the most important tools available to unravel the dynamics of turbulence. The advantage of numerical simulations compared to experimental techniques resides in their ability to resolved the full three-dimensional velocity field. However, the computational cost increases rapidly as a power of the Reynolds number simulated with an exponent between 3 and 4. Thereby, the first simulations were performed for simplified systems where only a limited range of scales were resolved and the rest were modeled as in the pioneer work by Deardorff (1970). These approaches are called *Large-Eddy Simulations* (LES) and remain important nowadays owing to its cheaper computational cost. It was only a few years later when the first *Direct Numerical Simulation* (DNS) of isotropic turbulence was carried out by Orszag & Patterson (1972), i.e., a simulation where all the dynamically relevant scales of the flow are resolved directly without any model aside from the Navier–Stokes equations. The first DNS of a turbulent channel flow was presented by Kim *et al.* (1987) and the first

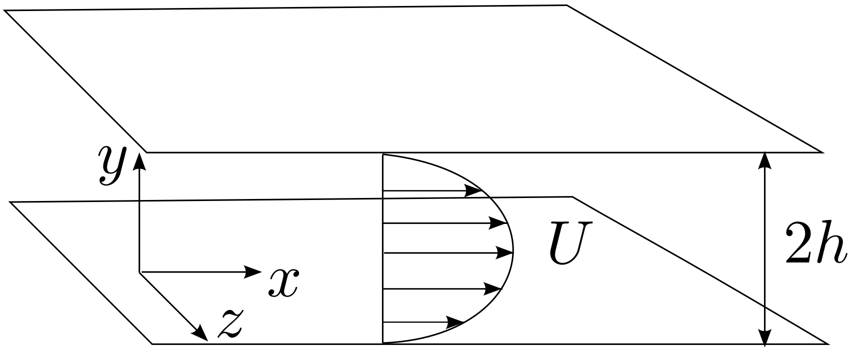

Figure 1.2: Sketch of the geometry of a turbulent channel.

boundary layer by Spalart (1988). In both cases, the outstanding results proved the great potential of DNS as a tool to understand turbulence with a level of detail never achieved before.

1.2 Wall-bounded turbulence

Most technologically relevant turbulent flows are bounded by walls and their study is of paramount importance. One of the most widely used and successful theories is the so called *classical theory for wall-bounded turbulence* found in many monographs (for instance Tennekes & Lumley, 1972; Kuglin & Hines, 1975; Townsend, 1976; McComb, 1990; Lesieur, 1991; Schlichting & Gersten, 2000; Pope, 2000; Jiménez, 2000) and usually valid for three canonical geometries: boundary layers, channels and pipes.

In this section, we summarize the main results of the classical theory particularized for turbulent channel flows. Let us consider a turbulent channel as the one shown in figure 1.2, with two walls separated by a distance $2h$ and the other two directions extending to infinity. Let us consider a statistically stationary incompressible turbulent flow with density ρ and kinematic viscosity ν, which moves on average along one direction. The streamwise, spanwise and wall-normal directions are denoted by x, z and y, respectively, and the instantaneous velocity of the flow by u_t v_t and w_t, which are functions of x, y, z and time, t. The only non-zero mean velocity is obtained by averaging u_t in the homogeneous directions (x and z) and time, and is denoted by $\langle u_t \rangle = U(y)$.

The streamwise velocity may be decomposed in the mean and fluctuating components as,

$$u_t(x, y, z, t) = u(x, y, z, t) + U(y), \tag{1.6}$$

Note that v_t and w_t have zero mean and are equivalent to the fluctuating velocities v and

w, respectively. Introducing the previous decomposition in the Navier–Stokes equations, and averaging in the homogeneous directions and time results in

$$\partial_y(\overline{uv}) = -\frac{\partial_x P}{\rho} + \nu \partial_y^2 U, \tag{1.7}$$

$$\partial_y(\overline{v^2}) = -\frac{\partial_y P}{\rho}, \tag{1.8}$$

where P is the average pressure and the term $-\overline{uv}$ is known as the *tangential Reynolds stress*. Note that the average derivatives are zero along the homogeneous directions.

Relations (1.7) and (1.8) are usually called *Reynolds–averaged Navier–Stokes equations* and determine the shape of the mean velocity profile $U(y)$. The mean pressure gradient, $\partial_x P$, is responsible for sustaining the mass flux in the streamwise direction, as oppose as the viscous terms that work against.

Integrating equation (1.8) in the y direction yields

$$P_0(x) = P + \rho\overline{v^2}, \tag{1.9}$$

where P_0 is an integrating constant depending only on x. Since the flow is homogeneous in x, it is satisfied that $\partial_x \overline{v^2} = 0$ and

$$\frac{\mathrm{d}P_0(x)}{\mathrm{d}x} = \partial_x P \neq q(y), \tag{1.10}$$

and the average pressure gradient is independent of y. Integrating (1.7) in y and using relation (1.10) we obtain

$$\overline{uv} = -\frac{y}{\rho}\frac{\mathrm{d}P_o(x)}{\mathrm{d}x} + \nu \partial_y U - u_\tau^2, \tag{1.11}$$

where u_τ^2 is the constant of integration with dimensions of velocity squared. Evaluating the previous relation at $y = 0$ results in the friction stress at the wall, $\tau_w = \nu(\partial_y U)_{y=0}$, which is equal to the square of the *friction velocity*, u_τ. At $y = h$, the symmetry of the channel implies that $-\frac{h}{\rho}\frac{\mathrm{d}P_o(x)}{\mathrm{d}x} = u_\tau^2$. The total tangential stress is defined as

$$\tau = -\overline{uv} + \nu \partial_y U, \tag{1.12}$$

and can be expressed as a function of y/h and u_τ as

$$\tau = u_\tau^2 \left(1 - \frac{y}{h}\right), \tag{1.13}$$

that is, a linear relation between total stresses with the distance from the wall. The variables h, ν and u_τ characterize the channel flow, and define the non-dimensional group

$Re_\tau = u_\tau h/\nu$, namely, the *friction Reynolds number*. The corresponding velocity, length and time-scales built from the variables, u_τ, ν/u_τ, ν/u_τ^2 , are usually called *wall units* or *inner units*, and will be denoted by the superscript $+$. If the viscosity is not relevant, the quantities with units of velocity, length, and time may be non-dimensionalized by u_τ, h and h/u_τ, respectively, which are referred to as *outer units*. Note that in both inner and outer units, u_τ is considered the characteristic velocity of the flow.

Relation (1.13) is a fundamental property of turbulent channel flows and may be used to study the asymptotic behavior of different regions of the channel as $Re_\tau \to \infty$.

In the *inner region* (or region close to the wall) $y^+ \sim 1$ and $y/h \ll 1$. Assuming that the wall is smooth, equation (1.13) and its boundary conditions are

$$-\overline{uv^+} + \partial_{y^+} U^+ \simeq 1, \tag{1.14}$$

$$(\overline{uv^+})_{y=0} = 0, \tag{1.15}$$

$$(U^+)_{y=0} = 0. \tag{1.16}$$

The only independent variable in the relation above is y^+, and the solution has the functional form

$$U^+ = f(y^+), \tag{1.17}$$

$$\overline{uv^+} = g(y^+), \tag{1.18}$$

named as the *law of the wall* (Prandtl, 1925). Very close to the wall, $\overline{uv^+} \simeq 0$ and

$$\partial_{y^+} U^+ \simeq 1, \tag{1.19}$$

that results in a linear profile for the mean velocity,

$$U^+ \simeq y^+. \tag{1.20}$$

Experimental data from Nikuradse (1932) showed the validity of relations (1.17) and (1.18). Reichardt (1951) extended the experimental measurements to regions closer to the wall and found that for $y^+ \lesssim 5$ the tangential Reynolds stresses are practically zero and the law of the wall applies. The region $y^+ \lesssim 5$ is often called *viscous region*, and the layer delimited by $10 \leqslant y^+ \leqslant 100$, *region close to the wall* or *buffer layer*.

The exterior region of the channel is defined by $y/h \sim 1$. Assuming $Re_\tau \to \infty$, equation (1.13) becomes

$$-\,\overline{uv^+} = (1 - y/h)\,, \tag{1.21}$$

and the viscous stresses are negligible. Note that the previous relation can not satisfy the non-slip condition at the wall, which is not very relevant since it is intended to work at the center of the channel only. Equation (1.21) does not provide information about the particular shape of the mean profile. However, it points to y/h and u_τ as the only magnitudes involved in the outer region. From dimensional analysis, it follows

$$U^+ - U_c^+ = F(y/h), \tag{1.22}$$

where U_c is the mean centerline velocity of the channel. Equation (1.22) is known as the *velocity defect law* and was first obtained by von Kármán (1930).

The inner and outer solutions presented above are only valid for $y^+ \sim 1$ and $y/h \sim 1$, respectively. However, for high Reynolds numbers, there must be a region where both solutions coexist. This region is called the *intermediate region* or *logarithmic layer* for reasons that will become clear below. In such a region, $y^+ \to \infty$ and $y/h \ll 1$, and the solutions from equations (1.17) and (1.22) must match. By dimensional arguments, the velocities must be of the form

$$U = u_\tau f(y^+), \tag{1.23}$$

$$U = U_c + u_\tau F(y/h), \tag{1.24}$$

and both have to match in the intermediate region. To avoid the dependence with the parameter U_c, we can match their gradients instead,

$$\frac{u_\tau}{\nu} \partial_{y^+} f(y^+) = \frac{1}{h} \partial_{(y/h)} F(y/h), \tag{1.25}$$

and multiplying relation (1.25) by y results in

$$y^+ \partial_{y^+} f(y^+) = y/h \partial_{(y/h)} F(y/h), \tag{1.26}$$

where the right-hand side only depends on y^+ and the left-hand one on y/h. For that reason, both gradients must remain constant and equal to $1/\kappa$, where, κ is called the *Kármán constant* for historical reasons. The mean profile U is obtained integrating (1.26),

$$U^+ = \frac{1}{\kappa} \log(y^+) + B, \tag{1.27}$$

$$U^+ - U_c^+ = \frac{1}{\kappa} \log(y/h) - B_1, \tag{1.28}$$

that are valid for $y^+ \to \infty$ and $y/h \ll 1$. The constants κ and B are considered universal with values close to $\kappa \simeq 0.4$ and $B \simeq 5$, although a large scatter has been reported for B_1. Since the velocities above describe a logarithmic profile, the intermediate region is also called the *logarithmic layer*.

The procedure followed here to derive the logarithmic profile was proposed first by Millikan (1938), although there are other alternative approaches like the ones followed by von Kármán (1930) or Prandtl (1925).

Figure 2.2 in chapter 2 tests the logarithmic behavior of the mean velocity profile and shows an incipient logarithmic layer that is still quite small despite using one of the largest Reynolds numbers DNSs available nowadays.

The shape of the energy spectrum for the large scales may also be deduced for the logarithmic layer, assuming that u_τ and the distance to wall are the only relevant magnitudes. In that case, by dimensional analysis the spectrum has the form

$$E(k) \sim u_\tau^2 k^{-1}. \tag{1.29}$$

A more rigorous and detailed approach can be found in Perry *et al.* (1986). Equation (1.29) differs from the Kolmogorov spectrum and is only valid for the spectral range $k^+ \ll 1$ and $hk \gg 1$ in the logarithmic layer. For smaller scales, the Kolmogorov' spectrum is expected to be recovered.

1.3 Structural models in wall-bounded turbulence

The study of coherent structures in turbulence assumes that there is a group of coherent regions in the flow that are important enough to explain the dynamics of the whole flow. Of course, defining those regions is not trivial and its relevance compared to the rest of the flow is not guarantee and has to be proved.

In wall-bounded flows, the buffer layer is a relatively simple system since it only involves one-scale structures and it can be considered well understood nowadays. There are several works devoted to it and examples include the papers by Jiménez & Moin (1991), Jiménez & Pinelli (1999), Schoppa & Hussain (2002) and Kawahara *et al.* (2012) among others. In the present thesis, we focus on the structural models for the logarithmic layer in wall-bounded flows.

Attempts to describe wall-bounded turbulence in terms of coherent motions date at least to the work of Theodorsen (1952), who proposed a horseshoe vortex as the central structural element. Figure 1.3(a) sketches the structure elucidated by Theodorsen.

A seminal contribution was the attached-eddy model proposed by Townsend (1976) for the logarithmic layer and further developed by Head & Bandyopadhyay (1981), Perry & Chong (1982), Perry *et al.* (1986) and others. In such a model, wall turbulence was considered to be dominated by a forest of self-similar horseshoe wall-attached vortices of

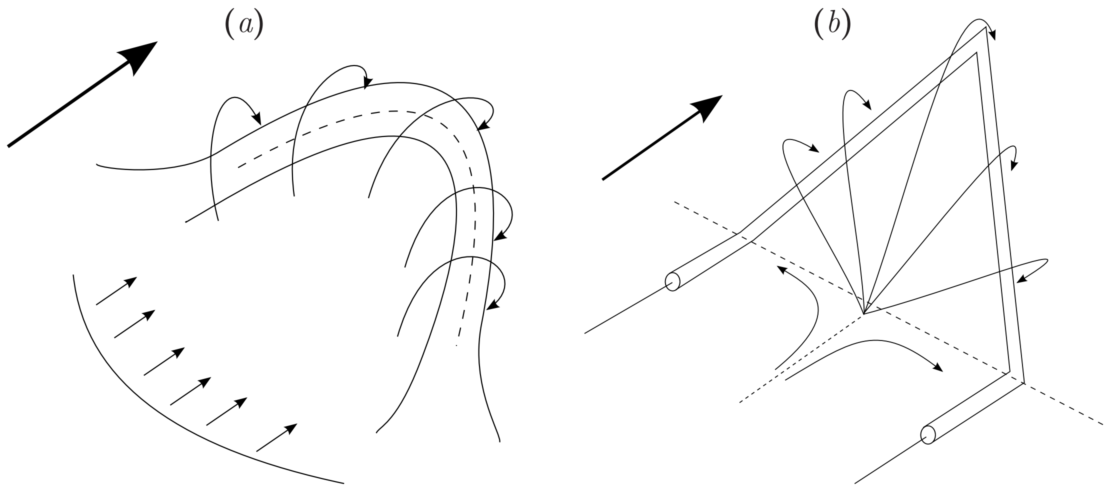

Figure 1.3: (*a*) Sketch of a horseshoe imagined by Theodorsen (1952). (*b*) Horseshoe proposed in the model by Perry & Chong (1982),

different sizes with characteristic velocity u_τ, leaned in the streamwise direction, and legs extending to the wall where they slip while convected by the mean flow. Townsend (1976) showed that a density of structures inversely proportional to the distance to the wall results in the well-known logarithmic profile for the mean velocity, and in logarithmic trends for the streamwise and spanwise mean-squared velocity fluctuations. From crude theoretical calculations, Perry & Chong (1982) proved that the shape of the structures changed from birth to death, and showed a linear growth of their height in time by applying the Biot-Savart law to an isolated horseshoe. The death of the structures would be caused by the decrease of the legs distance leading to an ultimate vorticity cancellation. However, most of these results were theoretical with little evidence from experimental data. Figure 1.3(*b*) sketches the hierarchy of self-similar eddies proposed by Perry & Chong (1982).

The visualization of sublayer streaks in boundary layers by Kline *et al.* (1967), of flow ejections by Corino & Brodkey (1969), and of large coherent structures in free-shear layers by Brown & Roshko (1974), increased the popularity of the structural view of turbulence. The quadrant analysis by Wallace *et al.* (1972) was proposed to study regions of intense tangential Reynolds stress in wall-bounded turbulent flows, and later used to define and characterize ejections (Bogard & Tiederman, 1986). Every new work introduced new potential candidates to describe turbulence in terms of coherent structures such as vortices, ejections, sweeps, streaks, etc. All these objects have played a role with a varying degree of relevance in most structural models proposed to explain how turbulent kinetic energy and momentum are redistributed in wall-bounded flows (see review by Robinson, 1991).

Followed by the rapid improvements of the experimental techniques and with the advent of DNS, a new iteration of the horseshoe vortex described by Theodorsen (1952) emerged called the *hairpin-packet paradigm.* Originally proposed by Adrian *et al.* (2000), the model conceived wall-bounded turbulence as a set of several hairpin vortices organized in coherent packets that grow from the wall into the outer region and with lifetimes much longer than their characteristic turnover times (Zhou *et al.*, 1999). The growth of the packets involves several mechanisms, including self-induction, auto-generation, and mergers with other packets, as discussed by Tomkins & Adrian (2003) and reviewed by Adrian (2007). The low-momentum regions observed in previous experiments would be produced by ejections contained within the hairpin packet and induced by the hairpins themselves. However, the evidence for hairpin vortices far from the wall is limited, and their origin and evolution remain unclear. The simulation by Wu & Moin (2010) showed experimental confirmation of a forest of hairpins in a transitional boundary layer. However, later simulations for well-developed turbulence at higher Reynolds numbers show no trace of hairpin shapes (Schlatter & Örlü, 2010; Sillero *et al.*, 2013). The hairpin-packet model is usually understood to involve relatively smooth vortex loops although, owing to the limitations mentioned above, recent discussions tend to include "canes, heads, legs and three-quarter hairpin shapes, generally asymmetric and distorted" into the class of 'hairpin-like' vortices (Dennis & Nickels, 2011*a*), making them hardly distinguishable from generic vortices. Figure 1.4(*a*) depicts all the important elements involved in the hairpin-packet model.

An alternative less organized model was proposed by del Álamo *et al.* (2006) and Flores & Jiménez (2010*a*), who analyzed the statistical properties of clusters of vortices in DNSs of turbulent channels with $h^+ = 550 - 1880$, and the temporal evolution of turbulent kinetic energy in minimal boxes for the logarithmic layer, respectively. Del Álamo *et al.* (2006) noticed that vortex clusters segregate into wall-attached and wall-detached families. The wall-detached clusters are dissipative objects, with sizes that scale with the local Kolmogorov scale. The attached ones form a self-similar family of objects that mark strong ejections. The average flow conditioned to an attached cluster consist on an elongated low-velocity streak extending downstream of the cluster, flanked by a pair of shorter high-velocity streaks. The authors concluded that such an organization suggests that the ejections marked by the clusters must be created at (or close to) their observed heights. While this average structure is consistent with the hairpin packet paradigm, del Álamo *et al.* (2006) pointed out that the instantaneous clusters are more complex, in agreement with earlier visualizations by Tanahashi *et al.* (2004). Moreover, while the

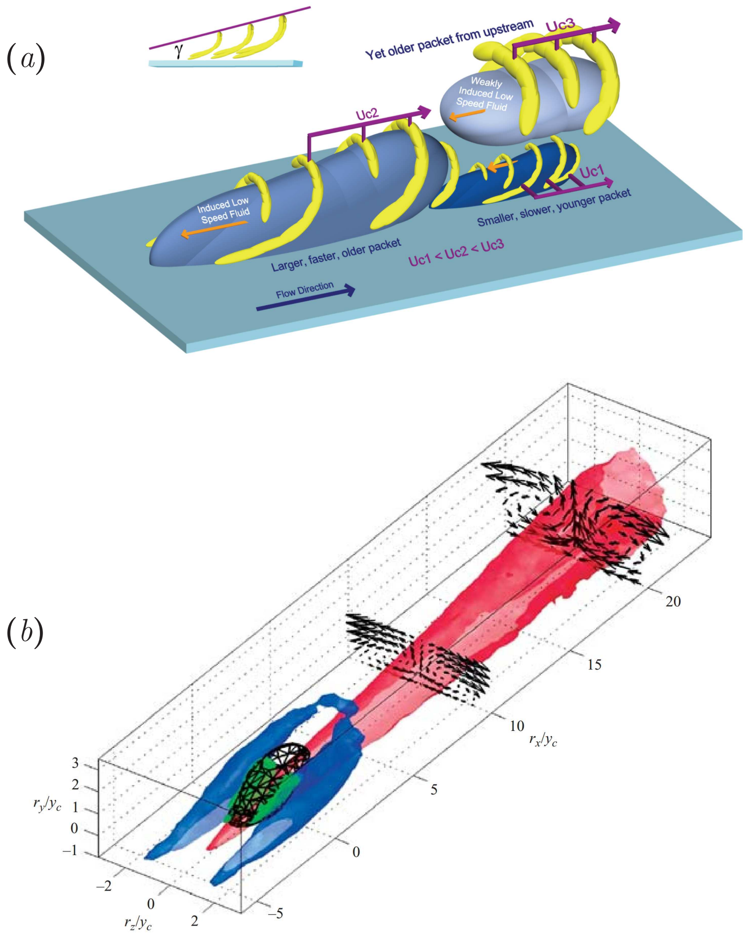

Figure 1.4: (*a*) Hairpin-packet paradigm by Adrian *et al.* (2000). From Adrian *et al.* (2000), copyright © 2000 Cambridge University Press. (*b*) Structural model proposed by del Álamo *et al.* (2006). From del Álamo *et al.* (2006), copyright © 2006 Cambridge University Press.

hairpin packets grow from the buffer region, there is evidence suggesting that the wall-normal velocity structures marked by the clusters do not.

Not only are the statistics of the clusters not affected when the buffer region is completely destroyed by an artificial forcing (Flores *et al.*, 2007), but their lifetimes are too short to account for their sizes (del Álamo *et al.*, 2006). The linear model of Flores & Jiménez (2010*b*) predicts that the disturbances of the wall-normal velocity grow little before being dissipated by the background turbulence, and again suggests that the ejections marked by the clusters must be created at, or close to, their observed heights. Figure 1.4(*b*) shows the flow structure proposed by del Álamo *et al.* (2006).

It is clear that the most interesting results are not the kinematic description of the structures in individual flow realizations, but the elucidation of how they relate to each other, and how and why they evolve in time. For example, how the energy or the momentum are exchanged among different structures and flow scales. Such dynamical studies have been difficult in the past, because it has been hard to obtain time-resolved information of three-dimensional structures, but that limitation is beginning to be relaxed. The early studies by Robinson (1991), the animations of a boundary layer by Spalart (1988), and the minimal-box simulations by Jiménez & Moin (1991), continued older experimental work using tracers in the buffer layer. More recently, it has become possible to extend time-dependent analysis to the logarithmic layer. Examples are the works in small-box simulations by Flores & Jiménez (2010*a*), or the recent analysis of vortex packets in a boundary layer by Lee & Sung (2011). However, in a continuous system such as a fluid, any such study depends on the choice of which structures to track. Most analyses of the buffer-layer, which is essentially a one-scale system, centered on vorticity, which is easily identifiable and representative of other quantities in that region. The initial extensions to the logarithmic layer followed the same method, although that region is multiscale and different quantities are associated with different scales. For example, it soon became clear that neither the vortex clusters in del Álamo *et al.* (2006) nor the hairpin packets in Adrian (2007) are single-scale objects, making the analysis of the logarithmic layer a challenging one.

1.4 Aims

The goal of the present thesis is to improve our insight into the multiscale dynamics of the logarithmic layer of wall-bounded turbulence.

In order to accomplish such a task, a novel approach is proposed based on the temporal tracking of three-dimensional coherent structures in a time-resolved direct numerical simulation of a turbulent channel flow at moderate/high Reynolds numbers. By making use of the time-resolved data, we aim to extend the structural time-dependent analysis to the logarithmic layer in terms of three-dimensional clusters of vortices, sweeps, ejections and streaks.

In particular, the objectives are to perform time-resolved DNSs of turbulent channels, to analyze the minimum domain to correctly capture the dynamics of the logarithmic layer and their interactions with other scales, to compute coherent structures associated with different flow quantities and study their features at instantaneous snapshots, and to track in time the previous structures and characterize their histories.

Finally, all the results are compiled to build a new structural model for the logarithmic layer.

1.5 Contents and organization of the thesis

Beyond this introduction, the present thesis is organized in five more chapters. In chapter 2, the direct numerical simulations used throughout the thesis are presented and the effect of the computational domain analyzed. In particular, three new time-resolved DNSs were computed with Reynolds numbers up to $Re_\tau = 4200$, and streamwise and spanwise dimensions of $2\pi h$ and πh, respectively. It is shown that this domain is large enough to accurately capture the dynamics of all the scales of the logarithmic layer. In addition, a very large computational box with streamwise and spanwise dimensions of $60\pi h$ and $6\pi h$, respectively, serves to determine the largest energetically active scales in turbulent channels. The contents of this chapter have been published in *Physics of Fluids* under the title '*Effect of the computational domain on direct simulations of turbulent channels up to* $Re_\tau = 4200$', volume 26, number 1, eid 011702, with Javier Jiménez as coauthor.

In chapter 3, the simulations above are used to compute and study the time-independent properties of several three-dimensional coherent structures, namely, vortex clusters, sweeps and ejections. It is shown that there is a family of geometrically self-similar coherent structures attached to the wall and responsible for most of the momentum transfer in turbulent channels. These structures are promising candidates to represent the wall-attached eddies described by Townsend (1976). The contents of the chapter have been published in the *Journal of Fluid Mechanics* under the title '*The three-dimensional structure of momentum transfer in turbulent channels*', volume 694, pages 100–130, with Oscar Flores and Javier Jiménez as coauthors, and in the *ACM Transactions on Mathematical Software* in a work entitled '*An efficient algorithm to compute the genus of discrete surfaces and applications to turbulent flows*', with Guillem Borrell as coauthor.

Chapter 4 contains the temporal extension of the previous one and, vortex clusters, sweeps and ejections are tracked in time for several eddy turnovers times in a time-resolved turbulent channel flow. The results provide unique and detailed information that allows to characterize the histories of the structures from birth to death. In particular, it is shown that the wall-attached eddies from the previous chapter are self-similar not only in space but also in time.

Chapter 5 is devoted to the turbulent cascade in terms of coherent structures and the processes of merging and splitting of coherent structures are associated with the direct and inverse cascades, respectively, as in the models proposed by Richardson (1920) and Obukhov (1941).

The contents of chapters 4 and 5 have been published in the *Journal of Fluid Mechanics* under the title '*Time-resolved evolution of coherent structures in turbulent channels: characterization of eddies and cascades*', volume 759, pages 432–471, with Javier Jiménez as coauthor.

Finally, the conclusions are offered in the last chapter, which summarizes the main results obtained in the present thesis, and describes a new multiscale structural model for the logarithmic layer of wall-bounded turbulence consistent with all the observations.

Chapter 2

Direct numerical simulations of turbulent channels up to $Re_\tau = 4200$[*]

2.1 Introduction

It is unclear how large the computational domain has to be in DNSs of plane turbulent channels to avoid unphysical constraints on the largest flow scales. Previous works have determined the minimal boxes for 'healthy' turbulence in the buffer region (Jiménez & Moin, 1991) and in the logarithmic layer (Flores & Jiménez, 2010*a*) in the sense of providing correct one-point statistics. Those results suggest that the whole flow would be healthy for boxes wider than about $3h$, where h is the channel half-height. However, even in the largest domains simulated until now, the premultiplied spectrum of the streamwise velocity remains unclosed for a contour of 20% of its maximum which only contains about 70% of the total streamwise energy as shown by Hoyas & Jiménez (2006). Moreover, some of the longest ejections in those boxes span the full length of the simulation domain even though they carry a substantial fraction of the total Reynolds stress (Guala *et al.*, 2006; Lozano-Durán *et al.*, 2012). In both cases, the longest structures are presumably misrepresented. Their maximum length remains unknown, and so are the consequences of constraining them.

Our goal is to examine the effect of the computational domain size on the large-scale structures of the flow, and on the velocity and pressure statistics. That information is used to determine the smallest box that reproduces identical one-point statistics to those in larger domains at all wall-normal distances. The results will be used to choose the

---

[*] Part of the contents of this chapter have been published in *Physics of Fluids*, volume 26, number 1, eid 011702, with Javier Jiménez as coauthor.

appropriate computational domain in the following chapters. Smaller-scale quantities such as the vorticities are not expected to be influenced by the box sizes used in the present chapter.

The chapter is organized as follows. Old and new DNSs are presented and described in the next section. The results are shown in section 2.3 and the conclusions offered in §2.4.

2.2 Numerical experiments

We have performed five new DNSs of plane turbulent channels. Their parameters are summarized in Table 2.1 together with the older simulations used for comparison. In all of them, the incompressible flow is integrated in the form of evolution equations for the wall-normal vorticity and for the Laplacian of the wall-normal velocity as in Kim *et al.* (1987), and the spatial discretization is dealiased Fourier in the two wall-parallel directions. Cases with $Re_\tau < 1000$ use Chebychev polynomials in y, while those with $Re_\tau \geq 2000$ use seven-point compact finite differences from Lele (1992). Time stepping is third-order semi-implicit Runge-Kutta by Spalart *et al.* (1991) with CFL $= 0.5$. The streamwise, wall-normal and spanwise coordinates are x, y and z respectively, and the mean streamwise velocity is $U(y)$. The corresponding components of the velocity fluctuations with respect to the mean are u, v and w. Primed quantities are root-mean-squared intensities, and the superscript $+$ denotes wall units based on the friction velocity u_τ and on the kinematic viscosity ν. The Kármán number is $Re_\tau = h^+$.

The very small case VS950 is a minimal box for the logarithmic layer from Jiménez (2013), and is known to have incorrect statistics above $y \approx L_z/3 \approx 0.25h$ (Flores & Jiménez, 2010*a*). The new small case S950 has a somewhat larger computational domain with streamwise and spanwise periodicities $L_x = \pi h$ and $L_z = \pi h/2$ at $Re_\tau = 939$, and Flores & Jiménez (2010*a*) suggests that its statistics should fail above $y \approx 0.5h$. The new medium cases M950, M2000 and M4200 have boxes with $L_x = 2\pi h$ and $L_z = \pi h$, with $Re_\tau = 932$, 2009 and 4179 respectively. The older large cases L550 from del Álamo & Jiménez (2003), L950 from del Álamo *et al.* (2004), and L2000 from del Álamo *et al.* (2004), have domains with $L_x = 8\pi h$ and $L_z \geq 3\pi h$, while the new very large case VL550 has a box size $L_x = 60\pi h$ and $L_z = 6\pi h$, and is intended to test whether there is a largest size for the structures that develop in the channel. The lines and symbols in table 2.1 are used consistently in later plots, and are chosen so that DNSs with the same Re_τ have similar symbols, unless otherwise stated. We also include results from the experimental

Case	Re_τ	L_x/h	L_z/h	Δx^+	Δz^+	Δy^+_{max}	N_y	$T_s u_\tau/h$	Symbols
VS950	948	$\pi/2$	$\pi/4$	11.6	5.8	7.8	769	77	– – –
S950 (present)	938	π	$\pi/2$	11.5	5.8	7.7	385	110	-·-·-
M950 (present)	932	2π	π	11.5	5.7	7.7	385	20	—●—
M2000 (present)	2009	2π	π	12.3	6.2	8.9	633	11	—■—
M4200 (present)	4179	2π	π	12.8	6.4	10.7	1081	15	——
L550	547	8π	4π	13.4	6.8	6.7	257	22	—▲—
L950	934	8π	3π	11.5	5.7	7.6	385	12	—○—
L2000	2003	8π	3π	12.3	6.1	8.9	633	11	—□—
VL550 (present)	547	60π	6π	12.6	5.0	6.7	257	5	—△—
E1000	1010	-	-	-	-	-	-	-	+
E2000	1960	-	-	-	-	-	-	-	*
E4000	4050	-	-	-	-	-	-	-	◇

Table 2.1: Parameters of the simulations. $Re_\tau = h^+$ is the Kármán number. L_x and L_z are the streamwise and spanwise dimensions of the numerical box and h is the channel half-height. Δx and Δz are the spatial resolutions in terms of Fourier modes before dealiasing. Δy_{max} is the coarser spatial resolution in the wall-normal direction. N_y is the number of wall-normal collocation points. $T_s u_\tau/h$ is the total time used for statistics after discarding transients, in eddy turnovers. The initial letter of each case is related with the size of the domain: very small (VS), small (S), medium (M), large (L) and very large (VL). The entries starting with (E) are experimental channels from Schultz & Flack (2013).

channels from Schultz & Flack (2013) at $Re_\tau = 1010 - 4050$, denoted by E1000 to E4000. They are plotted in the same color as the DNS with the closest Re_τ. The case with the highest Reynolds number is the new M4200, with $Re_\tau = 4179$. It reaches a maximum Taylor-microscale Reynolds number $Re_\lambda = q^2[5/(3\nu\varepsilon)]^{1/2} \approx 200$, at $y \approx 0.4h$, where $q^2 = u^2 + v^2 + w^2$ is the magnitude of the velocity fluctuations and ε is the kinetic-energy dissipation rate. Assuming that the smallest coherent structures are of order 10η (Jiménez *et al.*, 1993) where $\eta = (\nu^3/\varepsilon)^{1/4}$ is the Kolmogorov viscous length, the resulting scale separation is $h/10\eta \approx 100$.

To illustrate the relative dimensions of the computational boxes from table 2.1, figure 2.1 shows the instantaneous streamwise velocity at the centerline of the channel VL550, and compares the sizes for very large, large and medium domains.

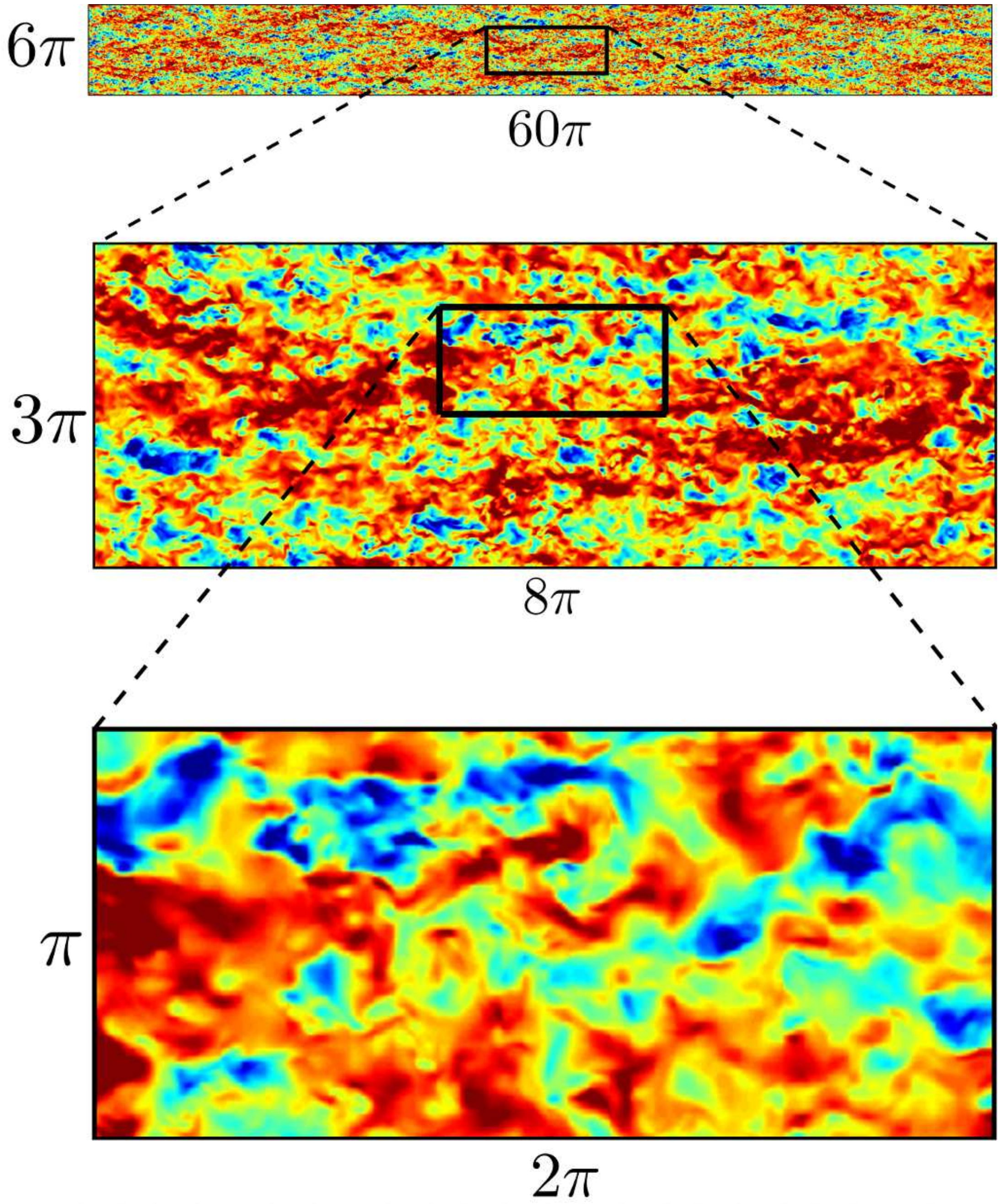

Figure 2.1: Instantaneous streamwise velocity at the centerline of the channel, $y = h$, for case VL550. The horizontal axis represents the streamwise direction and the vertical axis the spanwise one. The flow goes from left to right.

2.3 Results

The mean streamwise velocity profiles are shown in figure 2.2(*a*). They collapse reasonably well to a common logarithmic behavior for all the Reynolds numbers, experiments, simulations, and box sizes. The only anomalous behavior is the bump in the core of the smallest box (VS950), which is accelerated with respect to the other cases. To test the logarithmic behavior in more detail, figure 2.2(*b*) shows the diagnostic function

$$\Xi^+(y) = y^+ \partial U^+ / \partial y^+, \tag{2.1}$$

which is equal to the inverse of the Kármán constant κ wherever the mean profile is logarithmic. The only case with an incipient logarithmic layer is M4200, for which $\kappa \approx 0.38$ is within the scatter of the values obtained by other authors (Klewicki, 2010; Marusic *et al.*, 2010; Smits *et al.*, 2011) and Jiménez (2012). The agreement between the large (L950, L2000) and medium (M950, M2000) boxes is excellent across the whole channel, especially when compared with the differences with the smaller boxes, S950 and VS950. As expected, $U(y)$ and $\Xi(y)$ are identical for the large and very-large cases L550 and VL550. Experiments are not included in the diagnostic plot because of the relatively large scatter of the derivatives of their velocity profiles. Note that one-standard-deviation error bar has been added to figure 2.2(*b*) for case M4200 at $y^+ = 1000$, computed as in the appendix of Hoyas & Jiménez (2008). The error bars for other simulations are of the order of the thickness of the lines used to plot statistics, and are omitted. For cases L2000 and M2000 whose statistics have been accumulated for the same amount of eddy turnovers, the errors in u' at the center of the channel are roughly 3.4 times smaller in the large box. If we suppose that each snapshot from case L2000 is equivalent to $8\pi \times 3\pi/(2\pi \times \pi) = 12$ snapshots from case M4200, the result agrees well with the theoretical value $\sqrt{12} \approx 3.5$ and the statistical uncertainties decrease inversely proportional to the square-root area of the box simulated. See Hoyas & Jiménez (2008) for more details about the previous argument.

The mean-squared velocity and pressure fluctuations are presented in figures 2.3(a-d). We briefly highlight some aspects regarding the effect of the box size and of the Reynolds number, and the reader is referred to Townsend (1961, 1976); Metzger & Klewicki (2001); Hoyas & Jiménez (2006); Jiménez & Hoyas (2008); Hultmark *et al.* (2012) and Sillero *et al.* (2013) for a more detailed physical discussion. The profiles of the mean-squared spanwise velocity fluctuations w'^2 are logarithmic, as predicted in Townsend (1976), and as already reported in Jiménez & Hoyas (2008); Jiménez *et al.* (2010) and Sillero *et al.* (2013). This becomes more evident as the Reynolds number increases. The same is not

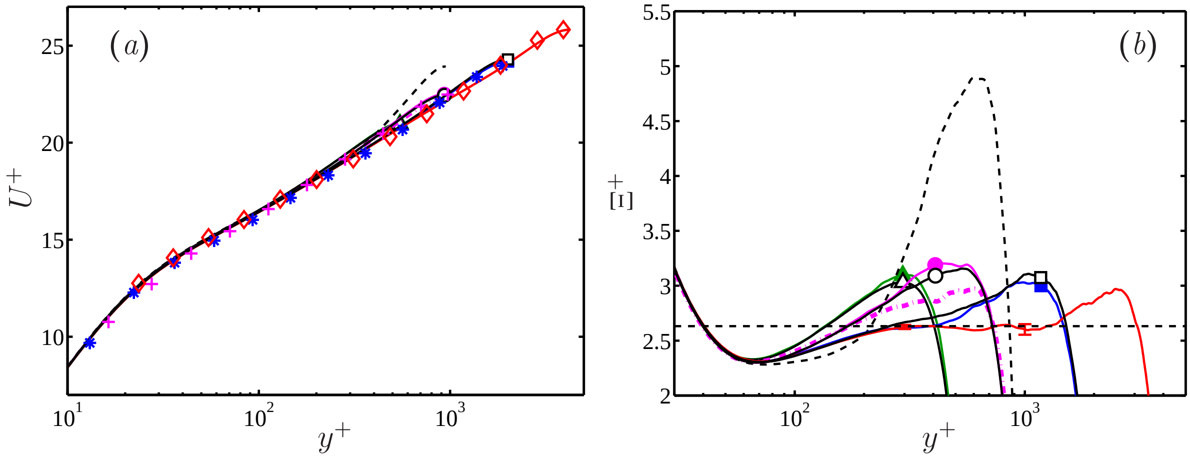

Figure 2.2: (*a*) Mean streamwise velocity profiles. (*b*) Logarithmic-law diagnostic functions. The dashed horizontal line correspond to a Kármán constant $\kappa = 0.38$. Lines and symbols are as in table 2.1.

true of the streamwise velocity fluctuations u'^2, for which a logarithmic region cannot be found even at the highest simulated Reynolds number. The profile of u'^2 gets flatter with Re_τ in the inner part of the region where the logarithmic behavior appears for the other variables as noted by Marusic *et al.* (2013) and Sillero *et al.* (2013), and it is unclear from the present data whether it will develop a local maximum, a plateau, or an actual logarithmic region for higher Reynolds numbers. Experiments in pipes from Marusic *et al.* (2013) suggest that u'^2 also develops a logarithmic range, although probably only in the outer part of the overlap layer. The asymptotic empirical law given in that paper has been added to figure 2.3(*a*), and is tangent to M4200 and to E4000. An experimental channel at $Re_\tau \approx 6000$ from Schultz & Flack (2013) not included in the figure, approximately follows that logarithmic behavior over a narrow range, suggesting that simulations at moderately higher Reynolds numbers than the present ones should begin to show it.

The mean-squared wall-normal velocity fluctuations v'^2 do not have a logarithmic range, as expected from the constraints imposed by impermeability (Townsend, 1976). Experimental and DNS data are in reasonable agreement, although v'^2 is slightly higher in E4000 than in the comparable simulation. Fluctuations for large (L950, L2000) and medium (M950, M2000) simulations agree very well at all heights, including the growth with Re_τ of u'^2 at its near-wall maximum (figure 2.4a), and at the center of the channel (figure 2.4b). Even the pressure fluctuations, which could be expected to be more sensitive than the velocities to the global effects of the box size, agree well between large and medium boxes. These results support the prediction by Flores & Jiménez (2010*a*) that

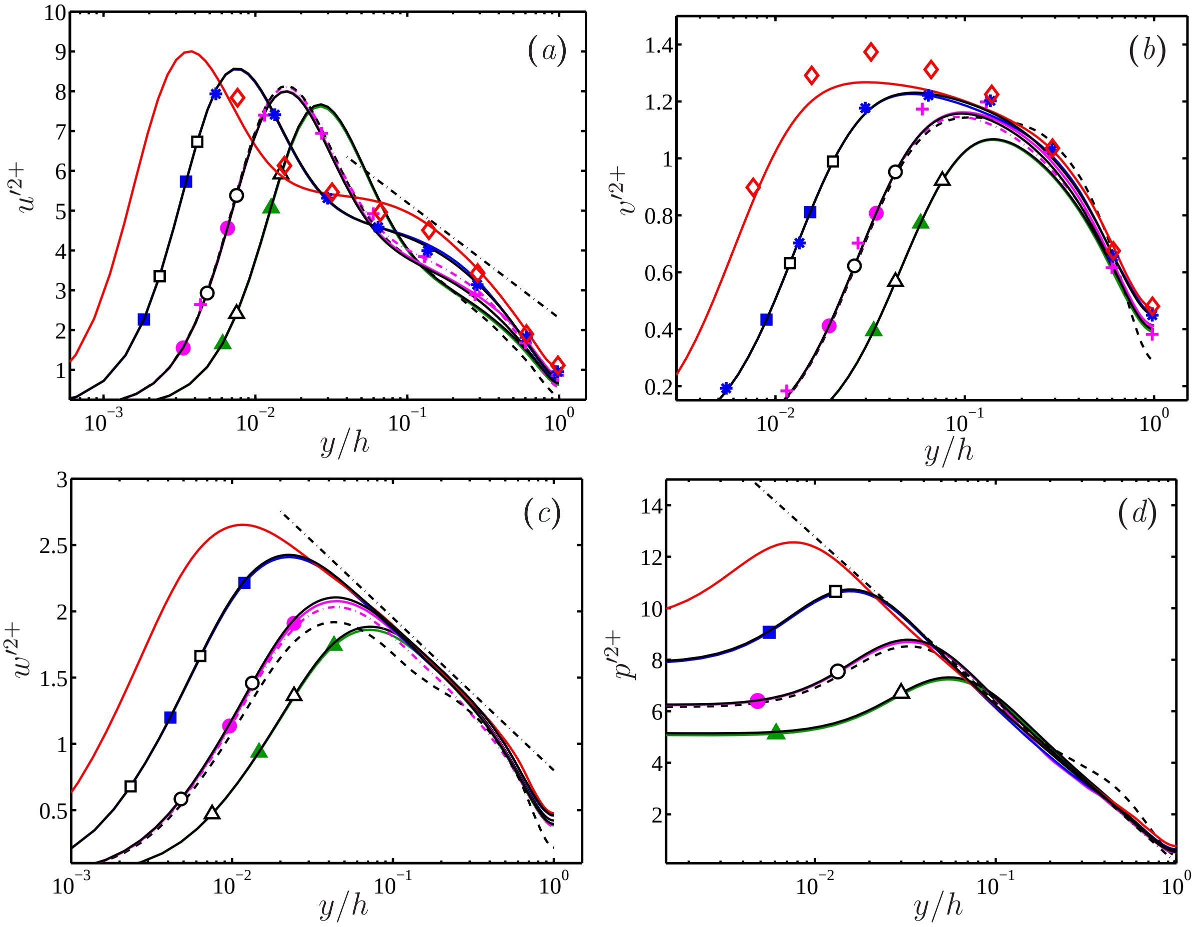

Figure 2.3: (a-c) Streamwise, wall-normal and spanwise mean-squared velocity fluctuations. (*d*) Mean-squared pressure fluctuations. The dashed-dotted line in (*a*) is $u'^2 = 2.25 - 1.26\log(y/h)$ from Marusic *et al.* (2013), the one in (*c*) $w'^2 = 0.80 - 0.50\log(y/h)$ from Jiménez & Hoyas (2008), and the one in (*d*) $p'^2 = 0.10 - 2.75\log(y/h)$ from Sillero *et al.* (2013). Other lines and symbols are as in table 2.1.

the $L_z \approx \pi$ is sufficient to obtain good statistics up to the center of the channel. It is also reassuring that there are no differences between the statistics of cases L550 and VL550, supporting the conclusion that the simulation boxes used at present are large enough to capture the one-point statistics of all the flow variables. The small box S950 has only minor differences in the mean-squared fluctuations with respect to the medium boxes, although we have seen that the logarithmic-law diagnostic function is more sensitive. On the other hand, the smaller box VS950 shows important deviations for the three velocity fluctuations above $y/h \approx 0.25$.

It was already noted by del Álamo *et al.* (2004) that the resolved part of the velocity

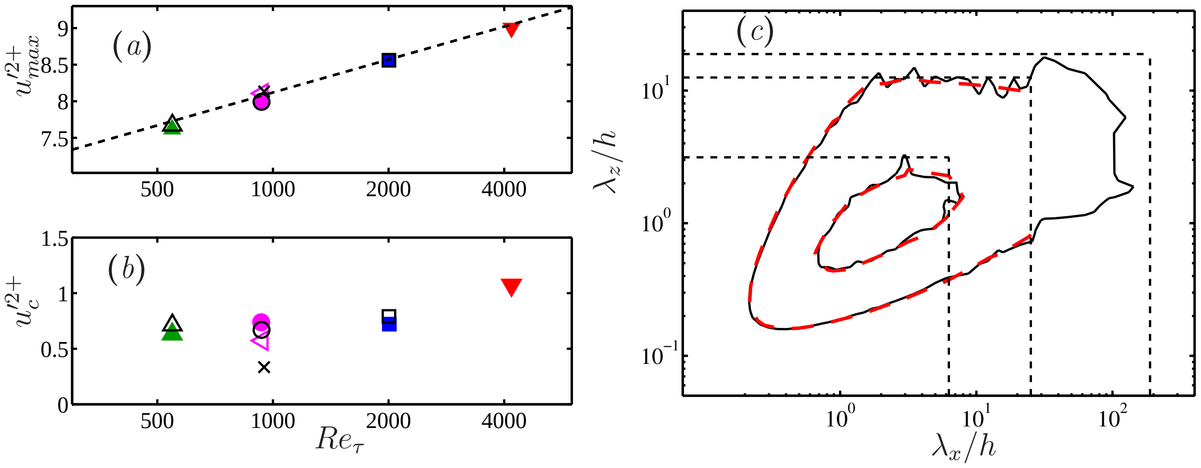

Figure 2.4: (*a*) Maximum of the mean-squared streamwise velocity fluctuations, u'^2_{max}. The dashed line is $u'^{2+}_{max} = 3.63{+}0.65\log(Re_\tau)$ from Sillero *et al.* (2013). (*b*) Mean-squared streamwise velocity fluctuations, u'^2_c, at the center of the channel ($y = h$). Symbols are as in table 2.1 except for: ▼, M4200; × VS950; ◁, S950. (*c*) Premultiplied two-dimensional spectra of the streamwise velocity, ϕ_{uu}, at $y = h$, as a function of the streamwise and spanwise wavelengths. The contours are 0.1 and 0.6 of the maximum value of ϕ_{uu}. (– – –), case L550; (——), case VL550. The dashed lines mark the box dimensions, L_x and L_z, for the medium, large and very large domains.

spectrum is not strongly affected by the size of the domain. The same is found to be true when comparing the spectral densities of the present medium and large boxes (not shown). Essentially, the spectra in the medium boxes follow those in the large ones until they are truncated at the maximum wavelengths fitting in the domain. A comparison between the premultiplied spectra, ϕ_{uu}, of the the large and very large boxes, L550 and VL550, is presented in figure 2.4(*c*). The lowest contour plotted is 10% of the maximum of ϕ_{uu} and contains roughly 80% of the streamwise kinetic energy. The spectrum of L550 is truncated by the box, but that of VL550 is not. Very large structures of length $O(25h)$ have been documented before in pipes and channels (Jiménez, 1998; Kim & Adrian, 1999; Marusic, 2001; del Álamo *et al.*, 2004; Jiménez *et al.*, 2004; Guala *et al.*, 2006; Monty *et al.*, 2007) but, to our knowledge, this is the first time that such a low energy contour has been shown to close within the computational box or within the spatial experimental domain. That result sets a new lower limit of $\lambda_x \approx 100h$ for the wavelengths at which some of the energy of the streamwise velocity fluctuations can be found.

The good agreement of the one-point statistics for large and medium boxes in figures 2.3(a-d) suggests that these infinitely long structures capture most of the dynamics of the actual ones, or at least of their interactions with the smaller scales of size $O(h)$. This is reasonable considering the disparity of lengths and times scales between them and the rest of the scales in the flow. A similar argument applies to the truncated spectral density of the streamwise velocity as pointed out by del Álamo *et al.* (2004).

2.4 Conclusions

Five new DNSs of plane turbulent channels have been presented. Three of them are computed in moderate domains with streamwise and spanwise sizes of $L_x = 2\pi h$ and $L_z = \pi h$ at $Re_\tau = 932$, 2009 and 4179. The two lowest Reynolds numbers, for which similar simulations exist in boxes with $L_x = 8\pi h$ and $L_z = 3\pi h$, have identical one-point statistics to the larger simulations, giving some confidence that the smaller boxes can be used for simulations with this particular purpose. This is true even if the largest structures are found not to fit within the smaller simulation box, as shown by the spectrum of the streamwise velocity. It is argued that, because of the periodic boundary condition, these very large structures are essentially infinitely long in the smaller boxes, but that their interaction with the well-resolved scales is correctly represented. Note that these medium-sized boxes are not necessarily cheaper to simulate than larger ones, because they have to run for longer times to accumulate comparable statistics, but they can typically be run in smaller computers. In contrast, the statistics of even smaller boxes, with $L_z \leq \pi/2$ differ significantly from the larger simulations, as predicted in Flores & Jiménez (2010*a*), with the largest discrepancies affecting the mean velocity profile.

The simulation with the highest Reynolds number, $Re_\tau = 4179$, continues the trends of the previously available simulations at lower Re_τ. For example, it confirms the growth with Re_τ of the near-wall peak of the mean-squared streamwise velocity fluctuations. It also shows an incipient logarithmic region in the diagnostic function of the mean velocity profile, with a Kármán constant $\kappa \approx 0.38$. No logarithmic range is found for u'^2, in contrast with clear ones for w'^2 and p'^2. Finally, in order to further test the effect of relaxing the constrains to the flow due to the limited numerical domain, a new simulation was performed in a very large box with $L_x = 60\pi h$ and $L_z = 6\pi h$ at $Re_\tau = 547$. No change was found in the one-point statistics, but the two-dimensional premultiplied spectrum of the streamwise velocity was shown to close for wavelengths of the order of $\lambda_x \approx 100h$ at the level of the contour containing 80% of the streamwise kinetic energy.

Chapter 3

The 3D structure of momentum transfer in turbulent channels [*]

3.1 Introduction

One of the most ubiquitous properties of turbulent flows is the enhancement of transport processes, such as mass, heat or momentum, and the success of many engineering devices depends of our ability to control and predict those processes. Of particular interest is the transport of momentum, which is responsible for the increased drag of wall-bounded turbulent flows, and for their characteristically flattened mean-velocity profiles. The object of the present chapter is to study the structure of the intense Reynolds stresses that carry most of the wall-normal flux of momentum, particularly in the logarithmic and outer layers.

The study of the statistical properties of the Reynolds stresses began in the late 1960's, with the observation by Kline *et al.* (1967) that the near-wall low-velocity streaks undergo a process of lift-up, oscillation, breakup and ejection, which they called bursting. Kim *et al.* (1971) showed that most of the turbulence production in the near-wall region occurs during those bursts, and several conditional-sampling techniques were developed to identify the structures involved in the process. Examples are the u-level detection of Lu & Willmarth (1973), the VITA (Variable-interval time-averaged) of Blackwelder & Kaplan (1976) and the VISA (Variable-interval space-averaged) of Kim (1985). Several of those techniques were surveyed by Bogard & Tiederman (1986), who concluded that the best

---

[*] Part of the contents of this chapter have been published in the *Journal of Fluid Mechanics*, volume 694, pages 100–130, with Oscar Flores and Javier Jiménez as coauthors, and in *ACM Transactions on Mathematical Software*, with Guillem Borrell as coauthor (submitted).

compromise between detection probability and false positives was provided by the quadrant analysis of Wallace *et al.* (1972), Willmarth & Lu (1972) and Lu & Willmarth (1973), in which points of the flow are classified in terms of the quadrant of the parameter plane of streamwise and wall-normal velocity fluctuations. Q1 events (outward interactions) have $u > 0$ and $v > 0$, Q2 events (ejections) have $u < 0$ and $v > 0$, Q3 events (inward interactions) have $u < 0$ and $v < 0$, and Q4 events (sweeps) have $u > 0$ and $v < 0$. Hereafter, Q events will be referred to simply as Qs, and we will occasionally group the 'gradient' Q2s and Q4s as Q^-, and the 'counter-gradient' Q1s and Q3s as Q^+.

As in previous chapters, u, v and w are streamwise, wall-normal and spanwise velocities, and are usually understood to refer to fluctuations with respect to the mean. The streamwise and spanwise coordinates are, respectively, x and z. The wall-normal coordinate, y, is zero at the wall. Overlined ($\overline{\varphi}$) and primed (φ') variables respectively denote average values and root-mean-squared (r.m.s.) intensities of the fluctuations, computed over the homogeneous directions and time. The channel half-height or boundary-layer thickness is h, and the '+' superindex denotes wall units defined in terms of the friction velocity u_τ and of the kinematic viscosity ν. We often classify results as relating to the buffer, logarithmic or outer regions, arbitrarily defined as $y^+ < 100$, $100\nu/u_\tau < y < 0.2h$, and $y > 0.2h$, respectively. Varying the limits of the logarithmic layer within the usual range did not significantly alter the results.

Although most of the early work focused on bursting in the buffer region, studies during the 1990's began to establish a relationship between near-wall bursting and outer structures. Antonia *et al.* (1990) applied a variant of the u-level method (WAG, window average gradient) to boundary layers with relatively high Reynolds numbers based on the momentum thickness, $Re_\theta = U_\infty \theta/\nu = 1360$–$9630$, corresponding to $h^+ = 530$–3100. They reported that outer-scale discontinuities in the streamwise velocity, extending across the whole thickness of the boundary layer, tend to be located near the upstream end of the near-wall bursts. Wark & Nagib (1991) applied quadrant analysis to a boundary layer at $Re_\theta = 4650\,(h^+ = 1500)$, and found large conditional events with sizes of the order of h. Using a related identification technique in the atmospheric boundary layer, Narasimha *et al.* (2007) described Reynolds-stress structures with lengths comparable to the distance to the wall that, because of the high Reynolds number involved, were both very long in wall units and very short compared with the boundary layer thickness. Hoyas & Jiménez (2006) showed that the spectral signatures of the very-large motions (Jiménez, 1998; Kim & Adrian, 1999), or global modes (del Álamo *et al.*, 2004), characteristic of the outer region are present at the wall, as well as those of similar smaller structures in the logarithmic layer, and Hutchins & Marusic (2007*b*) showed that part of that influence is a modulation of the intensity of the small-scale buffer-layer fluctuations.

More recently, Flores & Jiménez (2010*a*) showed that the hierarchy of structures of increasing sizes postulated by Townsend (1976) for the logarithmic layer can be represented numerically in computational boxes of widths proportional to the height to be studied. Each box contains a single complex structure, including a segment of a streamwise velocity streak and a cluster of vortices, that bursts quasi-periodically to fill the box with essentially normal turbulence, with a strong Q2 and Q4 occurring simultaneously. The existence of a hierarchy of Q2s and Q4s was also conjectured by Wark & Nagib (1991), and is consistent with the similarity observed by Kailas & Narasimha (1994) between the conditionally sampled structures extracted from the near-wall region of laboratory boundary layers, and those in the logarithmic region of the atmospheric boundary layer. It was also shown in chapter 2 that computational domains with streamwise and spanwise lengths equal to $2\pi h$ and πh respectively are large enough to accurately reproduce the one-point statistics of larger boxes.

Q2s and Q4s play important roles in most of the structural models proposed to explain how turbulent kinetic energy and momentum are redistributed in wall-bounded turbulence. The majority of these models (see review by Robinson, 1991) are loosely based on the attached-eddy hypothesis of Townsend (1976), and involve wall-attached vortical loops growing from the wall into the outer region (Perry *et al.*, 1986). More recently, in order to account for the very large scale motions mentioned above, as well as for earlier experimental evidence on the internal structure of the bursts (Bogard & Tiederman, 1986), a variant model has evolved to include vortex packets (Adrian *et al.*, 2000), in which trains of hairpin vortices grow from the wall by a process of merging (Tomkins & Adrian, 2003) and self-regeneration (Zhou *et al.*, 1999). The heads of the hairpins are arranged into inclined shear layers generated by the combined induction of the hairpins of the packet, with a Q4 upstream and above the packet, and a Q2 beneath it. Ganapathisubramani *et al.* (2003) used PIV data on wall-parallel planes in a boundary layer with $Re_\theta = 2500\,(h^+ = 1060)$ to quantify the contribution to the Reynolds stresses by packets of hairpins. They report that, at $y^+ = 100$, packets covering 4% of the area produce 28% of the total Reynolds stresses.

As discussed in §1.3, the hairpin-packet model is usually understood to involve relatively smooth vortex loops as the structures associated with Townsend's attached eddies, although recent discussions tend to include "canes, heads, legs and three-quarter hairpin shapes, generally asymmetric and distorted" into the class of 'hairpin-like' vortices

(Dennis & Nickels, 2011*a*), making them hard to distinguish from generic vortices. An alternative, less organized, structure was proposed by del Álamo *et al.* (2006), who analyzed the statistical properties of clusters of vortices (clusters hereafter) in DNSs of turbulent channels with $h^+ = 550 - 1880$. The clusters segregate into wall-attached and wall-detached families. The wall-detached clusters are dissipative objects, with sizes that scale with the local Kolmogorov scale. The attached ones form a self-similar family of objects that mark strong Q2s. The average flow conditioned to an attached cluster consist on an elongated low-velocity streak extending downstream of the cluster, flanked by a pair of shorter high-velocity streaks. While this average structure is consistent with the hairpin packet paradigm, del Álamo *et al.* (2006) pointed out that the instantaneous clusters are more complex, in agreement with earlier visualizations by Tanahashi *et al.* (2004).

In this chapter we study the statistical properties of the coherent structures responsible for the Reynolds stresses and the momentum transfer, and their possible relationship with vortex clusters. We generalize to three dimensions the quadrant analysis of Wallace *et al.* (1972) and Lu & Willmarth (1973), in a manner analogous to the method used by del Álamo *et al.* (2006) to study clusters. This is the first time that a full, three-dimensional, characterization of the Qs has been presented. These structures are candidates for the time-dependent analysis presented in the next chapter, including its relation with previously studied structures. As argued above, Qs are important for the transfer of momentum and for the generation of turbulent energy, and can be considered as lying at the top of the turbulent cascade. They have also been studied enough in the past, typically as one-dimensional sections, to provide some continuity of the present work with earlier ones. The further study of their temporal evolution, specially in relation to other flow structures, will be studied in the next chapter.

The chapter is organized as follows. Section 3.2 describes the numerical database and the method employed to identify Qs, which are classified in §3.3. The statistical properties of the attached Q2s and Q4s are presented in §3.4 and §3.5, and their relative positions and organization are described in §3.6. Finally, the results are discussed in §3.7, and conclusions are offered.

3.2 Numerical experiments and identification method

We use data from the DNSs of turbulent channels by del Álamo *et al.* (2004) at $h^+ = 934$ (case L950), and by Hoyas & Jiménez (2006) at $h^+ = 2003$ (case L2000). Their parameters are summarized in table 3.1. The details of both simulations were described

Case	h^+	L_x/h	L_z/h	Δx^+	Δz^+	N_y	N_F	N_Q	N_V
L950	934	8π	3π	11	5.7	385	21	4.6×10^5	9.6×10^5
L2000	2003	8π	3π	12	6.1	633	8	8.3×10^5	2.1×10^6

Table 3.1: Parameters of the simulations. L_x and L_z are the streamwise and spanwise dimensions of the numerical box and h is the channel half-width. Δx and Δz are the resolutions in terms of Fourier modes before dealiasing. N_y is the number of wall-normal collocation points. N_F is the number of fields used to accumulate statistics and N_Q and N_V are the numbers of Q^-s and of clusters extracted for the reference values of the identification thresholds.

in chapter 2. The two channels have large computational domains in the streamwise and spanwise directions, to ensure that the largest structures of the flow are reasonably well represented. Note that the Reynolds numbers of the simulations are comparable to those of most of the laboratory experiments mentioned in the introduction. Occasionally, we will use some of the cases with moderate and very large domains presented in chapter 2.

To investigate the statistical properties of the intense structures contributing most to the Reynolds stresses, we extend the one-dimensional quadrant analysis of Lu & Willmarth (1973) to three dimensions. We define the Qs as connected regions satisfying

$$|\tau(\boldsymbol{x})| > H u'(y) v'(y), \tag{3.1}$$

where $\tau(\boldsymbol{x}) = -u(\boldsymbol{x})v(\boldsymbol{x})$ is the instantaneous point-wise tangential Reynolds stress and the hyperbolic-hole size H is discussed below. Connectivity is defined in terms of the six orthogonal neighbors in the Cartesian mesh of the DNS, and an object is classified as belonging to the different quadrants according to the signs of the mean u_m and v_m, computed over the domain Ω of all its constituent points,

$$v_m = \frac{\int_\Omega v dV}{\int_\Omega dV}, \tag{3.2}$$

with a similar definition for u_m. It will be shown in figure 3.5(a) that this classification is essentially unambiguous. To identify correctly the Qs of the upper channel half, we change the sign of their v_m. That allows connected Q2s and Q4s to extend beyond the central plane, even if, otherwise, they would be classified as Q3s and Q1s over part of their volumes. On the other hand, it leads to distortions in the statistics of the quadrant contributions near the center of the channel ($y/h \gtrsim 0.7$), because some of the stresses are included with the wrong sign (see figure 3.3b, discussed in section 3.3).

Note that the threshold in (3.1) depends on the wall-distance. As noted by Nagasoa & Handler (2003), using an identification method with a constant threshold, such as $|\tau| > Hu'(y_0)v'(y_0)$, with some reference y_0, is problematic in inhomogeneous flows. In our case, fewer objects are recovered in the outer region if y_0 is chosen in the buffer layer, while choosing a high y_0 results in a cluttered buffer layer. This behavior agrees with the observations of Blackburn *et al.* (1996), and worsens as Reynolds number increases. Our choice of the local standard deviation in (3.1) results in a roughly constant contribution of the Qs to the Reynolds stress, and agrees with a similar choice in del Álamo *et al.* (2006) for the identification of vortex clusters. Nevertheless, the aforemention problem mainly affects structures based on small-scale quantities, such as vortex clusters, but it is less relevant for Qs. The results presented in this chapter were repeated for a constant threshold, $Hu'(y_0)v'(y_0)$, with $y_0 = 0.5h$ and qualitatively similar results were obtained.

As argued by Bogard & Tiederman (1986), quadrant analysis depends on the value of the hyperbolic-hole size H. They report that the optimum threshold for the buffer region is $H \approx 1$, based on direct comparisons between the detected events and instantaneous visualizations of the flow. We choose H based on the percolation behavior of equation (3.1). Percolation theory describes the statistics of the connected components of a random graph. Here, it is applied to the variation with H of the volume of the connected objects extracted by (3.1), as first used to identify vorticity and dissipation structures in isotropic turbulence by Moisy & Jiménez (2004), and in channels by del Álamo *et al.* (2006).

Figure 3.1(a) shows the percolation diagram of (3.1) in the two channels considered here. The solid lines are the ratio of the volume of the largest identified object, V_{lar}, to the total volume V_{tot} satisfying (3.1), and the dashed ones are the total number of identified objects, N/N_{max}, normalized with its maximum over H. When $H \gtrsim 3$, the identification only yields a few small objects that correspond to the strongest Qs. Decreasing H introduces new Qs, while previously identified ones grow in size. At first, the size of the largest Q changes little, and V_{lar}/V_{tot} stays roughly constant, but eventually the objects start to merge, resulting in a rapid increase of V_{lar}/V_{tot} and in a decrease of the number of objects. Figure 3.1(a) shows that this percolation crisis takes place in the range $0.5 \lesssim H \lesssim 3$, independently of the Reynolds number. For lower thresholds, $V_{lar}/V_{tot} \approx 1$, and most of the volume satisfying equation (3.1) belongs to a single object.

The vertical dashed line in figure 3.1(a) shows the threshold used in the present work, $H = 1.75$, chosen to maximize the number of objects. Some of the effects of changing H are discussed in later sections to illustrate specific points, but, in general, the results are qualitatively similar within the range $1 \lesssim H \lesssim 3$.

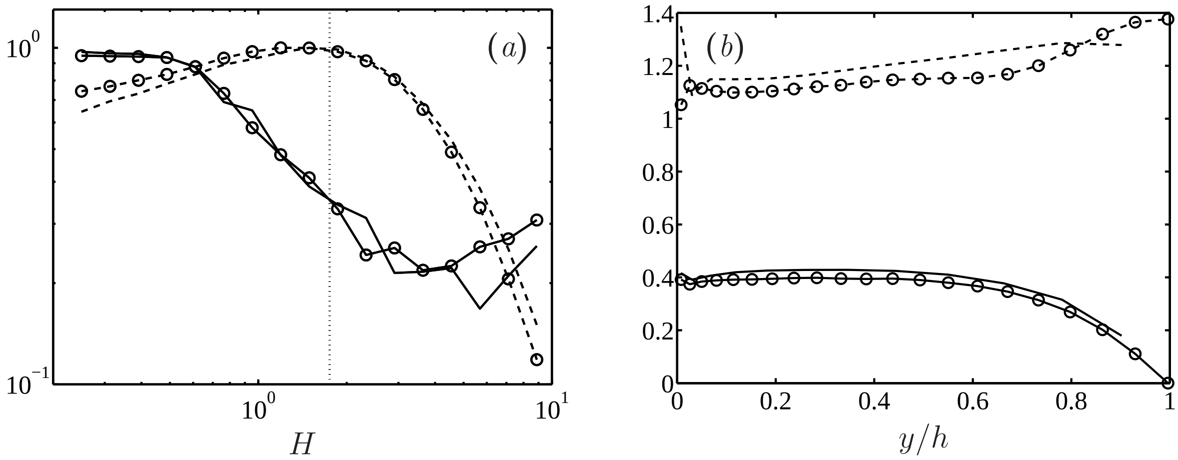

Figure 3.1: (a) Percolation diagram for the identification of Qs. ——, Ratio of the volume of the largest object to the volume of all identified objects, V_{lar}/V_{tot}; – – –, ratio of the number of identified objects to the maximum number of objects, N/N_{max}. The vertical dotted line indicates the chosen threshold, $H = 1.75$. (b) Profiles of the ratios $\overline{\tau}/(u'v')$ (——) and $\tau'/(u'v')$ (– – –). In both panels, lines without symbols correspond to L950, and those with symbols correspond to L2000.

To avoid the high cost of evaluating (3.1) in the full domain for $H \lesssim 0.5$, we followed del Álamo *et al.* (2006) and all data points in figure 3.1 were generated by applying (3.1) to sub-boxes of size $6h \times h \times 3h$ in the three Cartesian directions, rather than to the full computational domain ($25h \times 2h \times 12h$). The low values of V_{lar}/V_{tot} at the chosen threshold (figure 3.1a), and the agreement between both Reynolds numbers, give some confidence that the percolation diagram is not strongly influenced by that simplification. The rest of the data in the chapter are obtained applying (3.1) to full flow fields.

The threshold selected, $H = 1.75$, compares well with the one recommended by Bogard & Tiederman (1986) for bursts in the buffer region, but some care is needed when comparing it with other published values. The Reynolds stresses in (3.1) are normalized with the r.m.s. of the velocity fluctuations u' and v', as in Lu & Willmarth (1973) and Bogard & Tiederman (1986), but other normalizations are also found in the literature. The original analysis in Willmarth & Lu (1972) used multiples of the local mean Reynolds stress,

$$|\tau(\boldsymbol{x})| > \widetilde{H}|\overline{\tau}|(y), \tag{3.3}$$

while the more recent paper by Narasimha *et al.* (2007) proposes the r.m.s. of the stress fluctuations,

$$|\tau(\boldsymbol{x})| > \widehat{H}\tau'(y), \tag{3.4}$$

together with a more complicated identification algorithm involving the zero crossings of the instantaneous τ.

Figure 3.1(*b*) shows that H, $\widetilde{H}$ and $\widehat{H}$ satisfy approximately $\overline{\tau}/(u'v') \approx 0.4$ and $\tau'/(u'v') \approx 1.1$, at least in $y \lesssim 0.7h$, yielding

$$H \approx 0.4\widetilde{H} \approx 1.1\widehat{H}. \tag{3.5}$$

We will use those approximations in §3.3 to compare our results with others in the literature.

As mentioned in the introduction, del Álamo *et al.* (2006) found that wall-attached clusters of vortices are markers for strong Q2s. Hence, we also apply their methodology to extract clusters from the same fields used to extract the Qs. Briefly, a cluster of vortices is a connected region satisfying

$$D(\boldsymbol{x}) > \alpha_t D'(y), \tag{3.6}$$

where D is the discriminant of the velocity gradient tensor, $D'(y)$ is its standard deviation, and $\alpha_t = 0.02$ is a thresholding parameter. Connectivity is defined as for the Qs, and α_t is obtained from a similar percolation analysis. Full details can be found in del Álamo *et al.* (2006). Figure 3.2 shows several examples of actual objects extracted from the flow and demonstrates the complex geometries that may appear.

Finally, even if the flow is not isotropic, it will be useful in section 3.3 to define isotropic Reynolds numbers and scales to compare the largest with the smallest Qs. We define the Taylor microscale from $\lambda^2 = 10\nu K/\varepsilon$, and the microscale Reynolds number as,

$$Re_\lambda = q\lambda/\nu = K(20/3\nu\varepsilon)^{1/2}, \tag{3.7}$$

where ε is the kinetic-energy dissipation rate and K is the turbulent kinetic energy. The large scale velocity q is defined from $K = 3q^2/2$ as an 'isotropic' fluctuation intensity (Batchelor, 1953). The three velocity components are available for the two simulations, and K and ε can be computed directly, but we will use in the next section experimental data for which only u and v are known. In those cases, ε is computed from the temporal gradients of u, assuming isotropy of the small scales, and converting times to lengths using Taylor's frozen-turbulence hypothesis with the local mean velocity, and the kinetic energy is defined as $K = (u'^2 + 2v'^2)/2$. The error of the latter approximation can be estimated from the simulation data to be about 5% in the logarithmic layer. The Kolmogorov length is $\eta = (\nu^3/\varepsilon)^{1/4}$, and the integral scale is defined as $L_\varepsilon = q^3/\varepsilon$.

In the logarithmic layer of channels, ε can be approximated by the local turbulent energy production, $\varepsilon \approx u_\tau^2 \partial_y U \approx u_\tau^3/\kappa y$, where $\kappa \approx 0.4$ is the Kármán constant, from

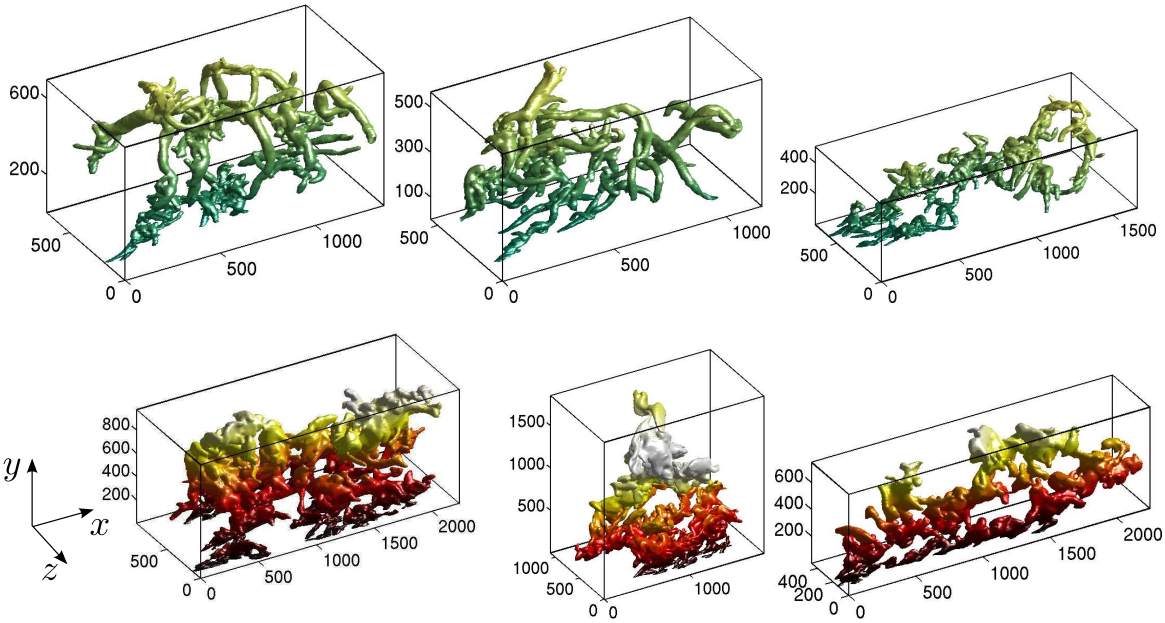

Figure 3.2: Examples of three vortex cluster (top row) and Qs (bottom row). The flow goes from bottom-left to top-right. The axis are scaled in wall-units. The colors change gradually with the distance to the wall, which is located at $y = 0$. Note that the objects are not to scale.

where it follows that $\eta^+ \approx (\kappa y^+)^{1/4}$, and that $Re_\lambda \propto \lambda^+ \propto y^{+1/2}$. In practice, the maximum Re_λ of channels is attained at $y \approx 0.4h$, above where it decreases slightly. Table 3.3 includes typical values for the two simulations and for some experiments at higher Reynolds numbers.

3.3 Wall-attached and detached objects

The above procedure yields about 10^6 Q^-s and clusters for each of the two Reynolds numbers under study (see table 3.1). Objects with volumes smaller than 30^3 wall units are discarded to avoid grid resolution issues, and are not included in the table. Although they account for about 70% of the number of originally identified Qs, they contain less than 1% of their volume. For clusters, the small discarded objects are almost 90% of the total number, and contain 1.5% of the volume. Each object is circumscribed within a box aligned to the Cartesian axes, whose streamwise and spanwise sizes are denoted by Δ_x and Δ_z. The minimum and maximum distances of each object to the closest wall are y_{min} and y_{max}, and $\Delta_y = y_{max} - y_{min}$.

Figure 3.3(a) shows the probability density function (p.d.f.) of the minimum and maximum wall distances for the Q^-s, and shows that they separate into two families.

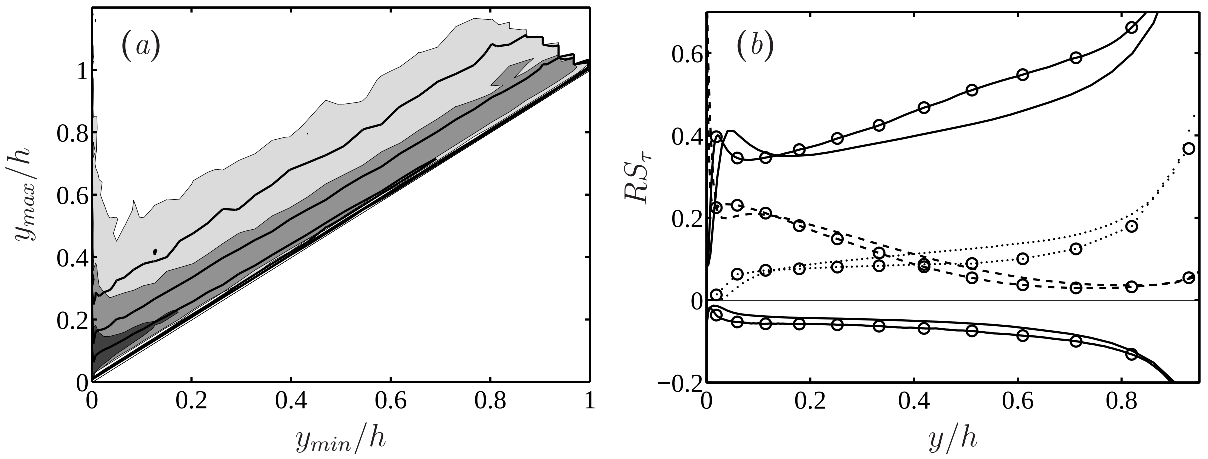

Figure 3.3: (*a*) Probability density function of the maximum and minimum wall distances of the identified Q$^-$s, $J(y_{min}, y_{max})$. The contours are 0.1, 1 and 10, from lighter to darker. Shaded contours are L950, and lines are L2000. (*b*) RS_τ, fraction of the total Reynolds stresses from: ——(positive), attached Q2; – – –, attached Q4; ········, detached Q$^-$; ——(negative), all Q$^+$. Lines without symbols for L950, lines with symbols for L2000.

Case	N_{f1}	N_{f2}	N_{f3}	N_{f4}	V_{f1}	V_{f2}	V_{f3}	V_{f4}
L950 (all)	0.18	0.33	0.19	0.31	0.004	0.056	0.006	0.025
L950 (attached)	0.02	0.15	0.006	0.13	0.000	0.047	0.000	0.015
L2000 (all)	0.19	0.33	0.21	0.28	0.004	0.059	0.008	0.022
L2000 (attached)	0.02	0.14	0.007	0.11	0.000	0.053	0.000	0.014

Table 3.2: N_{fk} is the numerical fraction with respect of the total number of objects, and V_{fk} is the volume fraction with respect to the total channel volume, for the four different types of Qs.

The first one is formed by the narrow vertical band with $y^+_{min} < 20$, and corresponds to wall-attached objects. The second family is formed by wall-detached objects with $y^+_{min} > 20$, contained in the wider parallel band above the diagonal in figure 3.3(a). The p.d.f. of the objects in that family depends only on their vertical size, not on their distance from the wall, so that $J(y_{min}, y_{max}) \approx J(\Delta_y)$. By definition, $y_{min} \leq h$, and the detached Q^-s only rise modestly above the channel center. The attached family, on the other hand, contains very large Q^-s that cross deeply into the opposite half of the channel. They are not easy to see in figure 3.3(a) because they are contained in the narrow band of very small y_{min}, but some of them reach almost to the opposite wall, $y_{max} \approx 2h$. For both Reynolds numbers, the number of attached Q2s and Q4s is about 40% of the total number of Q^-s, but they are large enough to account for about 80% of their volume. There are very few attached Q1s and Q3s. They only account for about 7% of the total number of Q^+s, and for 2% of their volume. The numerical and volume fractions for the different kinds of Qs are summarized in table 3.2.

3.3.1 Detached structures.

A similar separation was reported for clusters by del Álamo *et al.* (2006). In that case, the attached clusters are energy-containing eddies, while the detached ones are dissipative objects with sizes of the order of a few local Kolmogorov scales. Figure 3.3(a) suggests that the same is true for the detached Q^-s, because the width of their p.d.f.s appears to scale in wall units. In fact, the circumscribed boxes of the detached Qs are roughly cubical, with sides of the order of 30η at our Reynolds numbers. That does not necessarily mean that the Qs are isotropic. A characterization of the shape of the objects in terms of their smallest, intermediate and largest dimensions will be introduced in §3.5. For the detached Qs, they are of the order of $7 \times 14 \times 45$ Kolmogorov units, suggesting that they are isotropically oriented, rather than isotropically shaped. Those sizes change relatively little from $H = 1$ to $H = 1.75$, and make the detached Qs comparable to fragments of the compact 'worms' in the dissipative ranges of isotropic turbulence (Jiménez *et al.*, 1993) and channels (Tanahashi *et al.*, 2004). It is clear, for example, that isotropic turbulence must have Reynolds-stress fluctuations, even if they cancel in the mean, and figure 3.1(b) shows that, even in channels, the standard deviation of τ is 2.5 times larger than its average. The figures just discussed suggest that the detached Qs are examples of those fluctuations. For example, figure 3.3(b) includes the fraction of the total Reynolds stress carried by the detached Qs. It is never large, and the contribution of the Q^+s essentially cancels that of the Q^-s.

Case	y^+	Re_λ	$\overline{\tau}/u'v'$	$\tau'/u'v'$	L_ε/η	λ/η	ℓ/η	L_Q/L_{tot}
L950 (detached)	370	80	0.42	1.15	93	16	20	0.02
L2000 (detached)	800	127	0.39	1.11	187	22	21	0.01
L2000 (all)	800	127	0.39	1.11	187	22	31	0.10
Round jet		415	0.09	0.965	1.1×10^3	40	50	0.05
Plane jet (PJ1)		632	-0.12	0.963	2.1×10^3	49	50	0.03
Plane jet (PJ2)		1090	-0.04	0.962	4.7×10^3	65	76	0.04
ASL	4×10^4	1910	0.34	1.02	1.1×10^4	85	188	0.08

Table 3.3: Characteristic of the Reynolds-stress fluctuations in the channels, and in several high-Reynolds number flows from Antonia & Pearson (1999). The mean length, ℓ, of the Q$^-$s is defined for $H = 1.75$, estimated using Taylor's advection hypothesis with the local mean velocity. L_Q/L_{tot} is the time (or length) fraction satisfying the Q$^-$ criterion. The velocities are reduced to zero mean before processing.

The isotropic orientation of the detached Qs is consistent with the classical Corrsin (1958) criterion that eddies are isotropically oriented when their internal gradients are larger than the mean shear, $\ell^{-1}(\varepsilon\ell)^{1/3} \gtrsim \partial_y U$, with $U = U(y)$ the mean streamwise velocity profile. If we estimate ε in terms of the production, eddies smaller than about $\ell_C = u_\tau/\partial_y U$ should be isotropic. In the logarithmic layer, that implies $\ell_C \approx \kappa y$. The question was studied experimentally by Saddoughi & Veeravalli (1994), who concluded that the actual threshold for the Reynolds stress tensor to be approximately isotropic is $\ell_C \approx 0.25y$, implying that only attached structures of size $O(y)$ need to be examined to understand momentum transfer. We will indeed see in the next section that attached objects are responsible for most of the mean Reynolds stress.

Table 3.3 compares the characteristics of the Reynolds-stress fluctuations in several flows, most at considerably higher Reynolds numbers than ours. It turns out that the rough equality $\tau' \approx u'v'$ holds in all cases, including the plane jets for which the mean Reynolds stress is very small and countergradient. The correlation between u and v is responsible for the non-zero mean stress in the wall-bounded cases, but it is low enough to act as a second-order effect from the point of view of the intensity of the fluctuations of τ. Antonia & Atkinson (1973) and Lu & Willmarth (1973) showed that the p.d.f. of τ can be modeled as a joint Gaussian distribution of u and v, with the correct correlation coefficient. The resulting distribution is very intermittent, but its standard deviation differs little from $u'v'$ if $|\overline{\tau}|/u'v' \lesssim 0.5$.

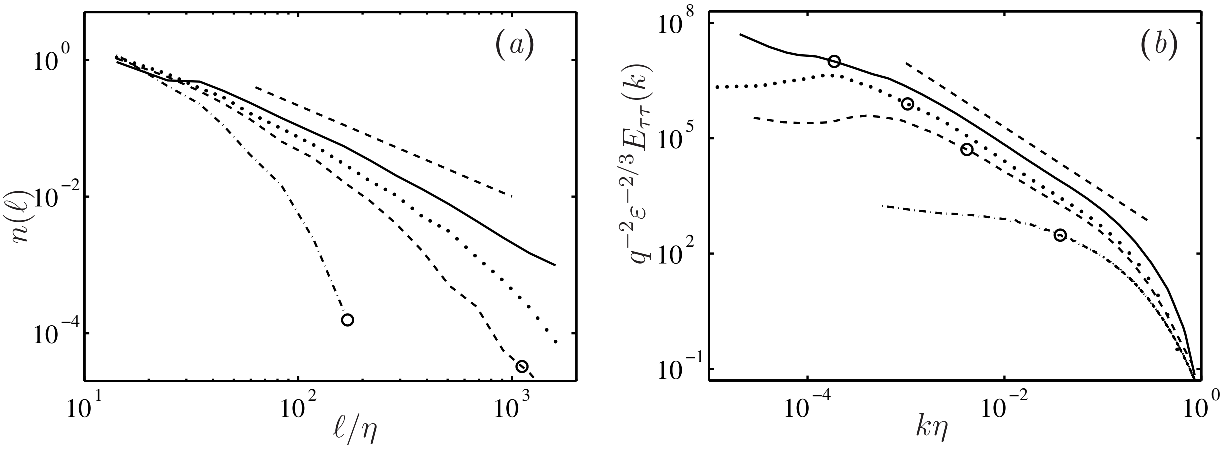

Figure 3.4: (*a*) Histograms of the lengths of the Q^-s, measured along streamwise lines. −·−·−, L2000; −−−, round jet; ········, PJ2; ——, ASL. The slope of the dashed diagonal is $-4/3$. All the histogram are normalised with their value at $\ell = 15\eta$ to compensate for the truncation of the smaller objects. (*b*) Spectra of the $\tau = -uv$ product. Lines as in (*a*). The slope of the dashed diagonal is $-5/3$. The open circles in both figures mark the integral scale, L_ε/η.

The experiments in the table are one-dimensional hot-wire traces, and the dimensions of their Q^-s are estimated from the lengths of the segments in which $\tau > Hu'v'$, discarding segments shorter than 8η to make them comparable with the threshold for small objects used in the numerical channels. The results given in the table for the channels were obtained by mimicking the experimental procedure, intersecting the Qs detected in the previous section with random streamwise lines. The average dimensions of the structures in the atmospheric surface layer (ASL) are longer than in the jets, probably because they include attached objects that cannot be distinguished in the experimental traces. To clarify that effect, the experiments in the L2000 channel were repeated taking into account either all the Q^-s, or only the detached ones, which are probably more representative of the case of the jets. The average lengths of the detached Q^-s are shorter when all the Q^-s are taken into account, but the effect is weaker than the difference between the ASL and the jets.

Even with those uncertainties, it is clear that the lengths of the Q^-s do not scale in Kolmogorov units. The closest match is the Taylor microscale λ, specially for the lower Reynolds numbers. That would be difficult to interpret, because the dynamical meaning of λ is unclear, but we will see below that it is the result of trying to define a single length scale for a turbulent phenomenon. Figure 3.4(*a*) displays histograms for the lengths of the one-dimensional Q-intersections for the experimental and numerical cases. They are very wide, with maxima near $\ell \approx 10\eta$ in the two cases in which the resolution is enough to capture that range of scales (L2000 and ASL). To facilitate comparisons, all the histogram have been redrawn on identical logarithmic bins, starting from $\ell = 10\eta$, and normalised to unity in the first bin. They have tails reaching into the integral length scales, which are marked in both panels of figure 3.4, even if the spectra in figure 3.4(*b*) suggest that the sample length of the ASL is not enough to capture the longest structures. The best approximation to the histograms is a power law $n_{ob}(\ell) \propto \ell^{-\alpha}$, with α between 4/3 and 5/3, approaching the former for high Reynolds numbers. The resulting average length is then

$$\overline{\ell} = \frac{\int n(\ell)\ell \,\mathrm{d}\ell}{\int n(\ell)\,\mathrm{d}\ell}, \tag{3.8}$$

where the two integrals extend over an inertial range of the order of $\eta < \ell < L_\varepsilon$. The integral in the numerator is dominated by its upper limit, and is proportional to $L_\varepsilon^{2-\alpha}$. The one in the denominator is dominated by its lower limit, and is proportional to $\eta^{1-\alpha}$. The mean length is $\overline{\ell} \propto L_\varepsilon^{2-\alpha}\eta^{\alpha-1}$. For $\alpha = 5/3$, that average is proportional to $\lambda \propto (L_\varepsilon \eta^2)^{1/3}$, which is the best fit for the lower-Reynolds number data in table 3.3, while for $\alpha = 4/3$ it is proportional to $(L_\varepsilon \lambda)^{1/2}$, which grows somewhat faster, and may be a better fit for the higher Reynolds numbers. From their derivations, it is clear that neither average should be considered the length of a ‘typical’ object.

The form of the ℓ histograms can be related to the spectrum of τ, reinforcing the argument that the objects that we are discussing are the carriers of the Reynolds-stress fluctuations. If we assume, from the previous discussion, that those fluctuations are objects with intensities of the order of the large-scale velocity q, and simplify them to a distribution of segments in which either $\tau = \pm q^2$ or $\tau = 0$, the correlation function $R_{\tau\tau}(r)$ is proportional to the probability that a point falls within an active segment with $\ell > r$. For $\alpha = 4/3$, it can be estimated as

$$R_{\tau\tau}(0) - R_{\tau\tau}(r) \propto \int_0^r n(\ell)\ell \,\mathrm{d}\ell \propto r^{2/3}, \tag{3.9}$$

corresponding to a spectrum $E_{\tau\tau}(k) \propto k^{-5/3}$. From purely dimensional arguments, the spectrum of τ would be expected to behave as $\varepsilon^{4/3}k^{-7/3}$, but figure 3.4(*b*) shows that that is not the case. The higher-order spectra of u^n were documented, among others, by Van Atta & Wyngaard (1975), who found them to behave as $k^{-5/3}$ for all orders. They gave theoretical arguments for the failure of the naive dimensional scaling, which are essentially that large- and small-scale quantities are statistically independent, and that the second-order structure function of the increments $\overline{\delta(u^n)^2}$ is dominated by terms of the form $u^{2n-2}\overline{\delta(u)^2}$. For example, the spectrum of quadratic quantities such as u^2 has the form $q^2\varepsilon^{2/3}k^{-5/3}$. Y. Kaneda (private communication) noted that the same argument should hold for the second-order quantity τ, and we have used that normalization in figure 3.4(b).

3.3.2 Attached structures.

Attached Q^{-}s are responsible for around 60% of the total Reynolds stresses in both channels, even if they cover less than 8% of the total area at all heights. As expected, their contribution in terms of volume and tangential Reynolds stresses increases as H is lowered. At the same time, there is a transfer from detached to attached objects, reflecting the percolation process by which small detached units collect into larger attached ones. For example, the percentage of detached volume with respect to the total Q^{-}s changes from 60% at $H = 3$, to 14% at $H = 1$. Interestingly, the percolation does not proceed at the same pace for the different kinds of structures. While the detached volume fraction of Q4s changes little from $H = 1.75$ to $H = 1$, suggesting that their percolation is essentially complete, that of the Q2s decreases by 30% in the same range.

The contributions to the mean stress mentioned above are in good agreement with those reported in the literature. Figure 16 in Willmarth & Lu (1972) shows that the contribution from Q2s and Q4s to the total Reynolds stresses in the buffer region is about 60% when $\widetilde{H} \approx 4.5$ ($H \approx 1.75$), and that those Qs cover roughly 10% of the measurements. At the lower end of the logarithmic region, Ganapathisubramani *et al.* (2003) report that hairpin packet signatures covering 4% of the total area contribute about 28% of the Reynolds stresses, which also agrees with our data for $H = 3$ (not shown). Narasimha *et al.* (2007) report that $\widehat{H} = 1$ yields structures that contains 100% of the total Reynolds stresses, while covering roughly 50% of the measurement time in the neutral atmospheric boundary layer at $h^{+} \sim 10^{7}$ ($y^{+} \sim 10^{5}$). When we use $H = 1$ ($\widehat{H} \approx 0.9$), the contribution to the total Reynolds stresses from attached Qs is also about 90%, but they only fill 20% of the area. The difference in covered area is most likely due to the eduction scheme used by Narasimha *et al.* (2007), who identify the structures by means of $\widehat{H}$, but subsequently extend them to the nearest zero crossing of the Reynolds stress. Note that the covering fractions given in table 3.3 for our channels are in reasonable agreement with those for the other high-Reynolds number flows, suggesting that Reynolds number effects can not explain the aforementioned difference between our results and Narasimha *et al.* (2007).

The contribution from the different quadrants, at $H = 0$, has been treated extensively in the literature, and was discussed in some detail by Jiménez *et al.* (2010) in the context of the similarities and differences between internal and external shear flows. The reader is referred to that discussion for further details and references, but the behavior is roughly

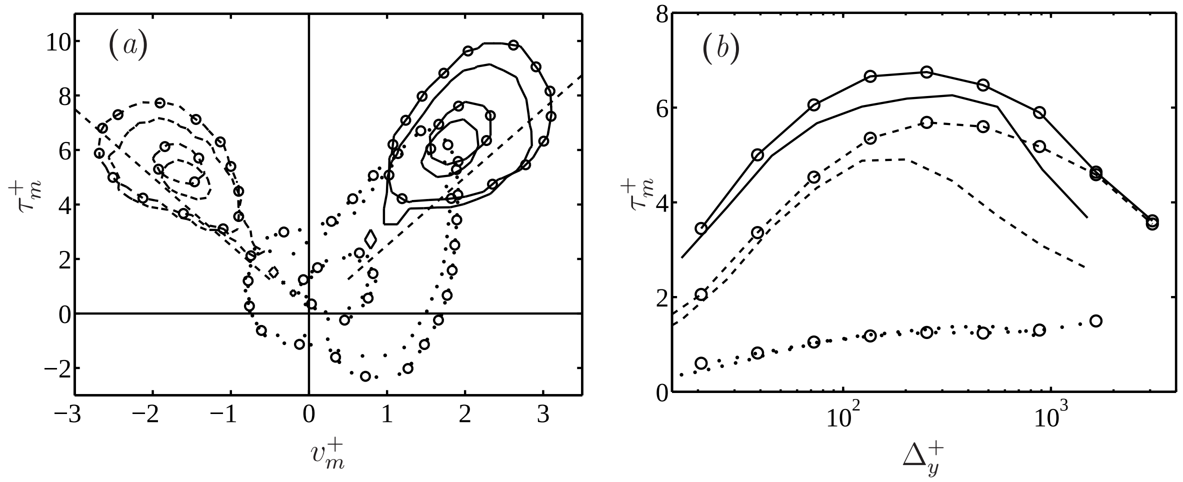

Figure 3.5: (*a*) Joint probability density function of the wall-normal velocities and the tangential Reynolds stresses averaged over individual attached objects with Δ_y in the logarithmic layer. For each case, the plotted contours contain 50% and 98% of the data. The straight dashed lines are $\tau_m^+ = \pm 2.5 v_m^+$. (*b*) Mean τ_m^+ for the different objects, as functions of their heights. In both panels, ——, Q2; – – –, Q4; ········, clusters. Lines without symbols are L950; those with symbols are L2000.

as in figure 3.3(*b*), including the reversal of the roles of Q2s and Q4s in the buffer layer, and the decay of the contribution of the Q4s far from the wall.

The picture that emerges from the previous discussion is that relatively few (25-30% by number), large and intense wall-attached Q$^-$s are responsible for most of the momentum transfer, while detached Qs play a secondary role. From now on, we will focus on the geometry and structure of the attached Q$^-$s, including, their geometry, spatial distribution, associated velocity fields, and relationship with vortex clusters.

3.4 Size and intensity of the attached Q$^-$s

The average Reynolds stress of an object, τ_m, is defined in the same way as the average velocities in (3.2), and is a measure of its intensity. Figure 3.5(*a*) shows the joint p.d.f. of v_m and τ_m for the attached Q$^-$s of the logarithmic layer. It clearly separates into Q2s, with $v_m > 0$, and Q4s with $v_m < 0$, confirming that the classification of the Qs in terms of their average velocities is meaningful. Similar plots are obtained in the buffer and outer regions, or using u_m instead of v_m.

The p.d.f.s of both kinds of Q$^-$s are roughly aligned along $\tau_m^+ = 2.5|v_m^+|$, which is consistent with a simple mixing-length argument in which the Reynolds stress is generated by displacing the mean velocity profile by an amount proportional to the eddy size, $l \propto y$. In the logarithmic region, $\partial_y U \approx u_\tau/\kappa y$, and

$$\tau^+ \propto v^+(l\partial_y U)^+ \propto v^+. \tag{3.10}$$

This is a very rough estimate, but it provides a simple explanation for the other interesting feature of figure 3.5(*a*), which is that the Reynolds stresses of the Q4s are weaker than those of the Q2s with the same $|v_m|$, probably because they can only draw momentum from the flatter shear in the central part of the channel (see figures 3.3*b* and 3.5*b*). The asymmetry between sweeps and ejections has been known for a long time (Nakagawa & Nezu, 1977), and its modeling has been discussed often. The best-known argument is based on the skewness of the velocity fluctuations (Raupach., 1981; Katul *et al.*, 2006), but it was shown by Jiménez & Hoyas (2008) that the velocity skewness can itself be traced to the inhomogeneity of the mean velocity profile.

Figure 3.5(*a*) includes the p.d.f. of the vortex clusters, and shows that most of them are Q2s, in agreement with the conditional velocity fields of del Álamo *et al.* (2006). On the other hand, a non-negligible fraction of clusters lie in other quadrants: 14% are Q4s, 5% are Q1s and 1% are Q3s, showing that their association with the Q2s is not exclusive. Accordingly, the average stress integrated over the attached clusters in figure 3.5(*b*) is weaker than for the Qs.

Figure 3.6 shows the p.d.f.s of the logarithms of the sizes of the circumscribing boxes for the Q⁻s, $J(\Delta_x, \Delta_y)$ and $J(\Delta_z, \Delta_y)$. They follow fairly well-defined linear laws,

$$\Delta_x \approx 3\Delta_y \quad \text{and} \quad \Delta_z \approx \Delta_y, \tag{3.11}$$

except for objects with $\Delta_y \gtrsim 1$, crossing the central plane. Del Álamo *et al.* (2006) reported similar, although slightly wider, laws for the attached clusters, $\Delta_z \approx 1.5\Delta_y$.

Figure 3.6 shows that the sizes of the boxes of the Q2s and Q4s are similar, but that the latter are more common below $\Delta_y^+ = 20$, which is to be expected because their negative v_m tends to flatten them against the wall. Those flattened Q4s have widths comparable to the high-speed streaks reported by Jiménez *et al.* (2004) in the buffer region, but they are shorter, in agreement with the conclusion in that paper that both the high- and the low-velocity streaks of the buffer layer are composite objects.

There are other, smaller, differences between the size distributions of Q2s and Q4s. Figure 3.6(*c*) shows that the Q2s are longer and narrower than the Q4s in the logarithmic region, and the same is true in figure 3.6(*d*) for the outer layer, although to a lesser degree. It is interesting that, although the modes of the size distributions grow linearly with y, as

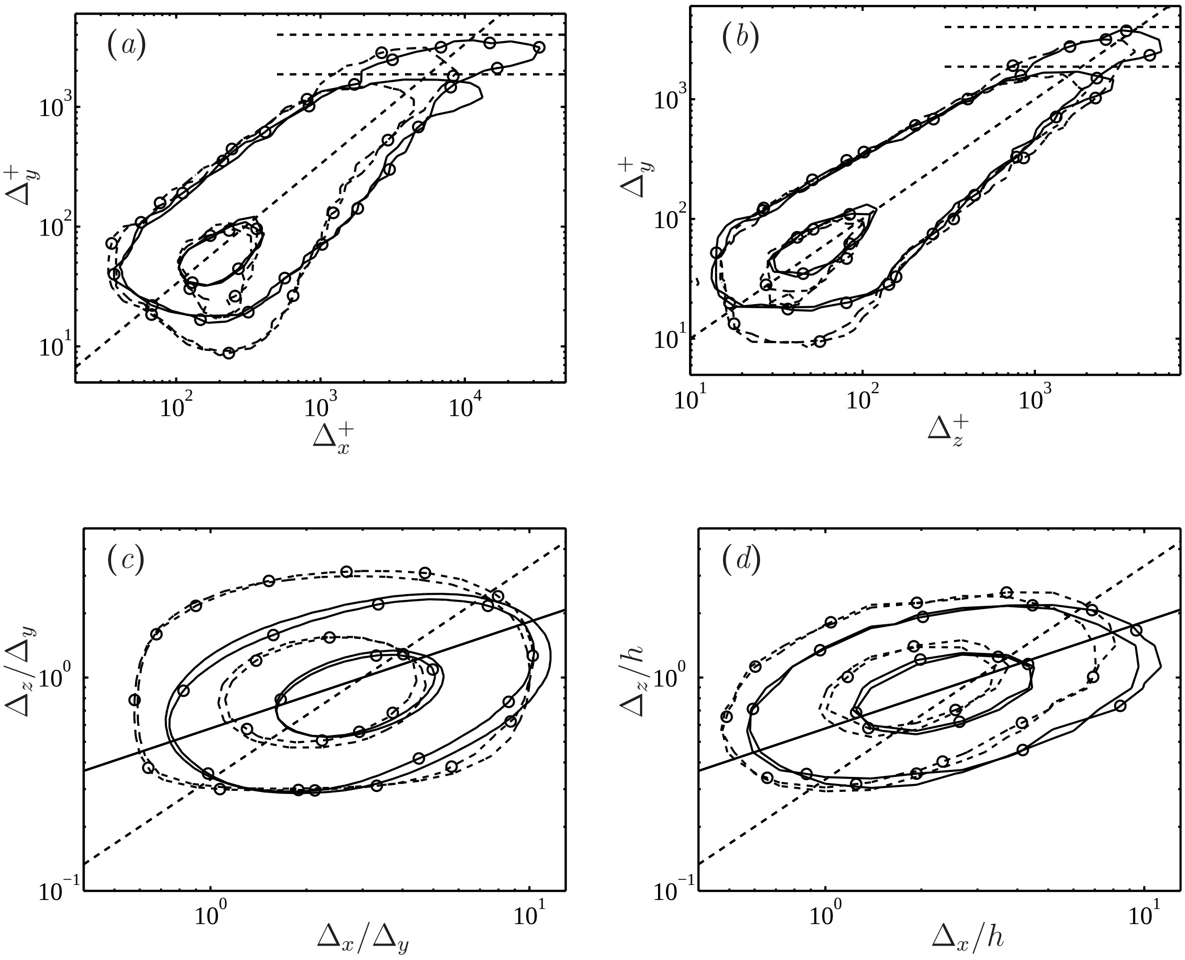

Figure 3.6: Joint probability density functions of the logarithms of the sizes of the boxes circumscribing attached Q$^-$s. (*a*) $J(\Delta_x^+, \Delta_y^+)$. (*b*) $J(\Delta_z^+, \Delta_y^+)$. (*c*) $J(\Delta_x/\Delta_y, \Delta_z/\Delta_y)$ for objects in the logarithmic layer. (*d*) $J(\Delta_x/h, \Delta_z/h)$ for objects with $0.5h < \Delta_y < 0.95h$. In all figures, the contours plotted contain 50% and 98% of the p.d.f. ——, Q2s; – – –, Q4s. Lines without symbols are L950, and those with circles are L2000. In all the panels, the solid and dashed straight lines are $\Delta_x\Delta_y = 3\Delta_z^2$ and $\Delta_x = 3\Delta_z = 3\Delta_y$, respectively, and the horizontal dashed ones are $2h$.

shown in figures 3.6(*a*) and 3.6(*b*), the relationship between Δ_x and Δ_z in the distributions at a fixed Δ_y is not linear. Both p.d.f.s are roughly aligned along $\Delta_x\Delta_y \propto \Delta_z^2$, which recalls the shape of the streamwise energy spectra in del Álamo *et al.* (2004). However, the two behaviors are probably unrelated, and it is even unclear whether the alignments in figures 3.6(*c*) and 3.6(*d*) are quadratic or some similar power. What those p.d.f.s measure is the dispersion among the sizes of structures with similar Δ_y, and the nonlinear alignment implies that there is more variation in Δ_x than in Δ_z. However, the dispersion is not large, and its amplitude does not appear to vary with the Reynolds number, making the definition, and relevance, of a power law uncertain. Most probably, the message of figures 3.6(*c*) and 3.6(*d*) is just that the mechanisms that deform the structures along the two coordinates are different. A possible model is that the deformation along x is due to the shear, while the weaker dispersion by the background turbulence is responsible for the spanwise growth (Flores & Jiménez, 2010*b*). On the other hand, an explanation in terms of longitudinally growing vortex packets may be equally valid (Tomkins & Adrian, 2003) and it will be analyzed in the next chapter by the temporal tracking of the objects.

The 'overhangs' of the p.d.f.s in figures 3.6(*a*) and 3.6(*b*) contain the largest structures, which are mostly Q2s extending beyond the centerline. Their sizes, $\Delta_x \approx 20h$ and $\Delta_z \approx 2h$, are comparable to the very-large-scale motions of Jiménez (1998) and Kim & Adrian (1999), or to the global modes of del Álamo *et al.* (2004). They are the only parts of the p.d.f.s that change appreciably with the detection threshold H, and also the only ones that do not satisfy the scaling self-similarity of the smaller objects, suggesting that the global modes are different from the Qs of the logarithmic and buffer layer, and are probably formed by percolated juxtapositions of smaller subunits. Figure 3.10 includes examples of a cluster and a Q2 from the logarithmic layer, and of a global Q2, and highlights the differences among them. The appearance of the latter clearly suggests a composite character, and it is difficult not to remark its similarity with the large-scale low-velocity streaky structures discussed, for example, by Hutchins & Marusic (2007*a*), or in figure 4 of Flores *et al.* (2007).

The very-large outer objects extending to the center of the channel carry a substantial fraction of the Reynolds stresses (Jiménez *et al.*, 2004; Guala *et al.*, 2006; Balakumar & Adrian, 2007). Figure 3.7 shows how the total stress carried by the Q^-s is distributed among objects of different heights. In general, the stress carried by objects of height y_{max} is maximum near $y = y_{max}/3$, although the distributions are not strictly self-similar, and tend to peak closer to the wall for the Q4s than for the Q2s. It is striking that about one third of the stress carried by the attached Q^-s is due to objects crossing the

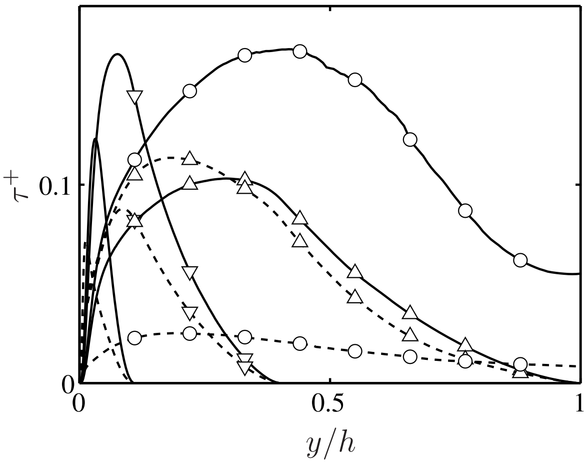

Figure 3.7: Reynolds stress carried by attached Q2s and Q4s with heights in different bands. Case L950. Lines without symbols, $y^+_{max} < 100$; ▽, $100\nu/u_\tau < y_{max} < 0.4h$; △, $0.4h < y_{max} < h$; ○, $y_{max} > h$. Solid lines are Q2s, dashed ones are Q4s.

centerline. About 70% of those objects are Q2s, and the rest are Q4s. The former are larger, accounting for 90% of the volume. There are only about 50 very large objects per field (< 1%), but they account for about 60% of the volume of the attached Qs, or 4% of the volume of the channel.

To check which fraction of the smaller attached structures are also aggregates of even smaller ones, we analyze the fragmentation of the Q^- as the threshold varies from $H = 1.75$ to $H = 3.0$ by tracking the Cartesian boxes circumscribing them. Intersections of actual objects are forbidden by the clustering procedure, which collects intersecting objects into single ones, but the boxes may intersect each other, usually because a large attached Q overlies smaller ones near its base. Those intersections are not very relevant, and usually involve objects of very different heights. To avoid them, only boxes whose heights differ by less than a factor of two,

$$1/2 \leq \Delta_y^{(i)}/\Delta_y^{(j)} \leq 2, \tag{3.12}$$

are considered as interacting in the rest of this chapter. Boxes with no interactions when $H = 1.75$, and therefore presumably 'isolated' (ranging from 90% by number in the buffer layer to 50% above $0.2h$), were tracked when the threshold was increased to $H = 3$. Of those that survived (about 35%), most were still isolated at the higher threshold, but the rest broke into sub-boxes, and were considered to have been originally composite. The number of composite Q^-s, and the number of pieces, increases with the distance to the wall; from 10%, and an average of 2.2 fragments for boxes originally below $y^+_{max} = 100$, to 20% and an average of 2.5 fragments when $y^+_{max} > 0.2h$.

Those percentages depend little on the Reynolds number, but change when the limit in (3.12) is relaxed from 2 to 4, allowing a wider range of scales between an object and its fragments. In that case, the percentage of initially isolated objects ranges from 90% below $y^+_{max} = 100$ to only 15% above $y^+_{max} = 0.2h$, and the fraction of surviving Q$^-$s increases to almost 60% away from the wall. Not surprisingly, more of those surviving objects turn out to be composite, ranging from 10% near the wall to 40% above $0.2h$.

We can now compare the size distributions of the Q$^-$s with other scaling information about wall-bounded flows. The proportionality $\Delta_z \approx \Delta_y$ in (3.11) agrees approximately with the results of Tomkins & Adrian (2003) and Ganapathisubramani *et al.* (2003) for hairpin packets in the near-wall region. It should be stressed that the Qs studied here cover the entire height of the flow, from $\Delta^+_y \approx 10$ to $\Delta_y = 2h$, while ordered hairpin packets have only been observed directly in the buffer and lower logarithmic layers ($y^+ \lesssim 200$), and become disorganized further from the wall (Lee & Sung, 2011; Jiménez, 2012).

Del Álamo *et al.* (2004) and Hoyas & Jiménez (2006) found that the peaks of the uv-cospectrum of L950 and L2000 align along $\lambda_z \approx 3y$, which agrees with (3.11) if we accept, from figure 3.7, that the maximum stress of the Q$^-$s is at $y \approx \Delta_y/3$. It also agrees with the relation between the width of the minimal logarithmic boxes in Flores & Jiménez (2010*a*) and the height to which they maintain turbulence. Moreover, the proportionality $\Delta_x \approx 3\Delta_z$ in (3.11) implies that the peak of the uv-cospectrum should be around $\lambda_x \approx 9y$, which is not too far from the ratio, $\lambda_x/y \approx 10 - 15$, found by Jiménez & Hoyas (2008) in boundary layers and channels. In all, those figures reinforce the conclusion that the structures described here are those responsible for most of the Reynolds stresses in wall-bounded turbulent flows.

The y dependence of the number of attached Q$^-$s per unit height and wall area is given in figure 3.8(*a*). As we have already seen, Q4s reach closer to the wall than Q2s, but otherwise their densities are similar and decay with size as $n^+_{ob} \propto (\Delta^+_y)^{-2}$. Because the cross-sections of individual Q$^-$s are proportional to $\Delta_x\Delta_z \propto \Delta^2_y$, the fraction of the area covered by Q$^-$s at a given y within the logarithmic layer is equally distributed among the Δ_y of the Q$^-$s crossing that level, which are those with $\Delta_y > y$. Moreover, since the Reynolds stress averaged over the section of individual Q$^-$s is also remarkably uniform within each structure, as shown in figure 3.8(*b*), the uniform distribution of areas implies a uniform contribution to the overall Reynolds stress by each Δ_y. Integrating over $y < \Delta_y < h$, the total stress is proportional to $h - y$, in agreement with the constant fraction of the total stress carried by the Q$^-$s in figure 3.3(*b*). Note that some such constraint has to be satisfied by any set of structures carrying the bulk of the Reynolds stress across

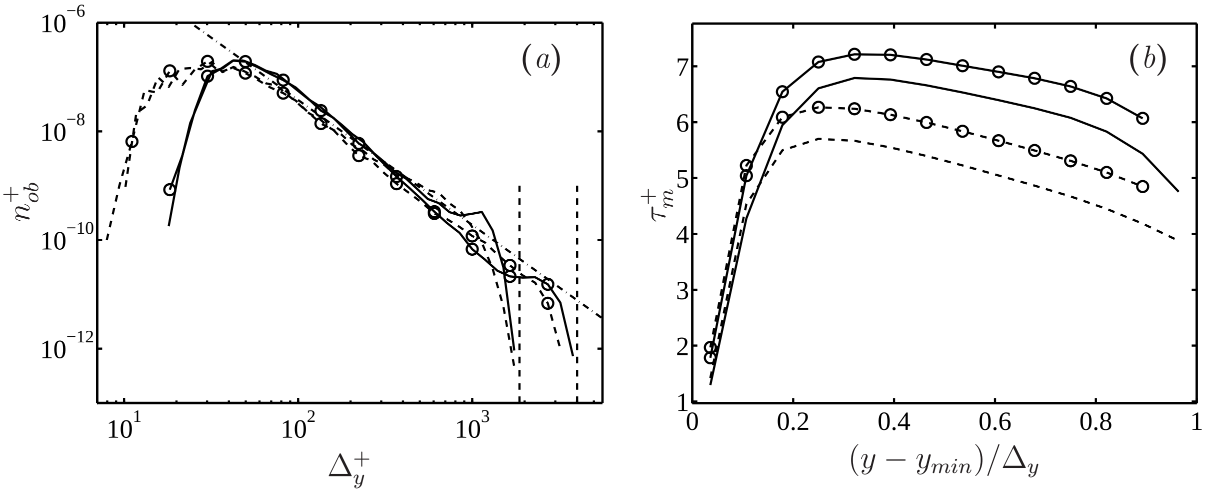

Figure 3.8: (a) Number n_{ob}^+ of attached events per unit height and wall area, and time, in wall units. ——, Q2s; – – –, Q4s. Lines without symbols are L950, those with circles are L2000. The chain-dotted line is $n_{ob} \propto {\Delta_y}^{-2}$, and the two vertical dashed lines are $\Delta_y = 2h$. (b) Mean $\tau_m(y)$ of attached Q$^-$s in the logarithmic layer, as a function of y within the object. ——, Q2; – – –, Q4. Lines without symbols are L950, those with circles are L2000.

the channel, because the total stress is fixed by the mean momentum equation, and it implicitly determines the decay law for n_{ob}.

On the other hand, the clusters, which are not constrained by the dynamics to carry a constant property flux, decay faster with Δ_y than the Q$^-$s. Del Álamo *et al.* (2006) showed that their density behaves like $n_{ob}^+ \propto (\Delta_y^+)^{-3}$. As a consequence, attached clusters are essentially near-wall objects, which can only associate with the smaller Q$^-$s. We will see in §3.6 that the larger Q$^-$s are mostly independent of small-scale vorticity.

3.4.1 Effect of the computational domain

The sizes shown in figure 3.6 are computed in large domains ($L_x = 8\pi$, $L_z = 3\pi$). To assess the effect of the computational box, some results for 'medium' ($L_x = 2\pi$, $L_z = \pi$) and 'very large' ($L_x = 60\pi$, $L_z = 6\pi$) domains are discussed next. The DNSs considered are the cases M2000, L550, L2000 and VL550 presented in the previous chapter in table 2.1.

The results are shown in figure 3.9. The distribution of spanwise sizes is barely affected by the size of the domain. On the contrary, the largest structures in x are found for case VL550, with streamwise lengths of the order of $40h$, and probably correspond to the very large-scale motions reported in previous works (Jiménez, 1998; Kim & Adrian, 1999;

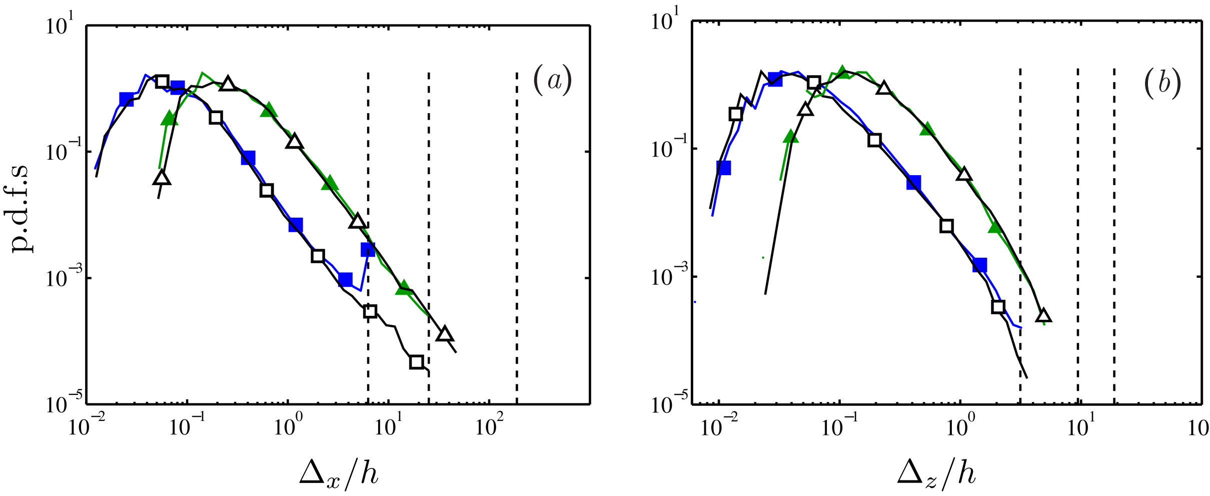

Figure 3.9: Probability density functions of the logarithm of the size of Qs. (*a*) Streamwise size, Δ_x. (*b*) Spanwise size, Δ_z. The vertical dashed lines are the edges of the domain for medium, large and very large boxes. –■–, M2000; –□–, L2000; –▲–, L550; –△–, VL550. Cases from table 2.1 .

Marusic, 2001; del Álamo *et al.*, 2004; Jiménez *et al.*, 2004; Guala *et al.*, 2006). They are somewhat shorter than the u-structures implied by the spectra shown in figure 2.4(c), in agreement with previous observations that the Reynolds-stress cospectrum is shorter than ϕ_{uu} (del Álamo *et al.*, 2004; Jiménez & Hoyas, 2008). The distribution of streamwise sizes in the medium box only differs from that in the larger domain at the limit $\Delta_x \approx L_x$, where it develops a peak caused by the accumulation of structures that would otherwise be longer than L_x, but do not fit in the domain. In agreement with that interpretation, the total probability contained in that peak is roughly the same as the one in the tail of the longer p.d.f. The number of structures per unit area with $\Delta_x \geq 2\pi h$ is $(0.041h^{-2})$ for M2000 and $(0.039h^{-2})$ for L2000, which are very close. It is important to realize that, because of the periodic boundary condition, these structures are seen by the flow in the shorter box as being infinitely long, but it was shown in chapter 2 that their interactions with the smaller scales are correctly represented.

3.5 Shape of individual objects

We showed in the previous section that, at least in the logarithmic layer, the circumscribing boxes of the attached Q^{-}s form a self-similar family with sizes proportional to y. The same was shown for the vortex clusters by del Álamo *et al.* (2006). In this section

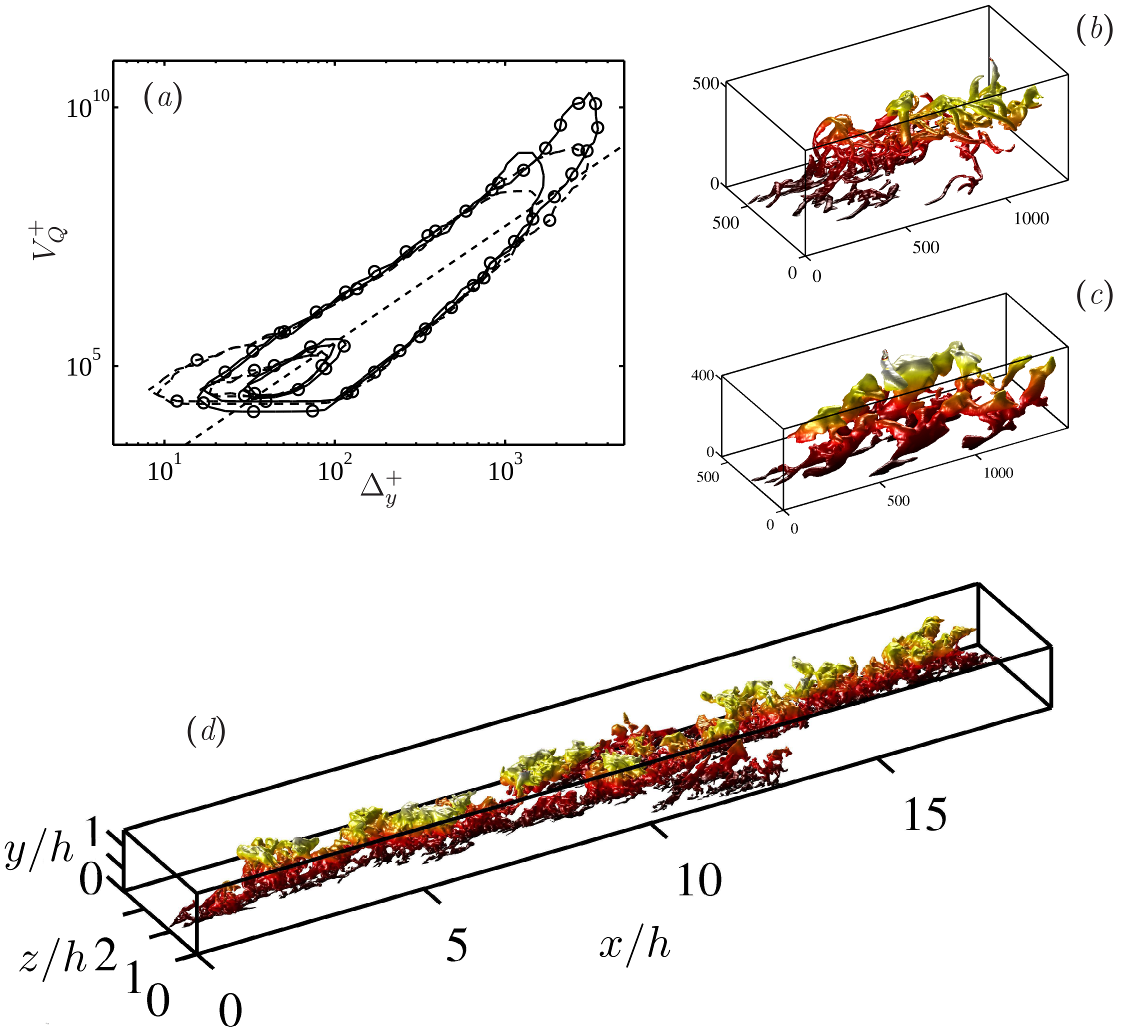

Figure 3.10: (*a*) Joint probability density function of the logarithms of the volume V_Q and the height Δ_y of attached Q$^-$s. The contours contain 50% and 98% of the data. The dashed straight line is $V_Q \propto \Delta_y^{2.25}$. (*b*) Instantaneous visualization of an attached cluster. (*c*) Instantaneous visualization of an attached Q2. The axes of (*b*) and (*c*) are in wall units. (*d*) Very-large-scale attached Q2, with the axes scaled with h. Note that the object crosses the center of the channel. The visualizations are colored with the distance to the wall; red (dark) near the wall, and white near the top. Flow is from bottom-left to top-right.

we study the shape of the objects themselves.

Figure 3.10(*a*) is the joint p.d.f. of the volumes and heights of the attached Q$^-$s, and follows quite well $V_Q^+ \propto (\Delta_y^+)^\alpha$, with $\alpha \approx 2.25$. A similar law, with $\alpha \approx 2$ was found for the clusters by del Álamo *et al.* (2006), who interpreted it as an estimate of their fractal dimension, and as an indication that they were shell-like. Figure 3.10(*a*) implies that the

Qs have slightly fuller shapes, which is confirmed by inspection of the individual cluster and Q2s in figures 3.10(*b*) to 3.10(*d*).

Although the power law in 3.10(*a*) seems persuasive, it can only be related to a fractal dimension by assuming that the objects themselves are self-similar. A more direct characterization requires estimating the shapes of the individual structures, to which end we define three 'intrinsic' lengths for each object, following the methodology of Moisy & Jiménez (2004). The outer scale, r_3, is the size of the smallest circumscribing cube, which typically coincides with Δ_x. The inner scale, r_1, is the side of the largest inscribed cube, and is computed from the inner coverage fraction, as in the appendix in Moisy & Jiménez (2004). The third scale, r_2, is related to the volume by $V_Q = r_1 r_2 r_3$.

The inner length, r_1, estimates the 'thickness' of the object, and is always the smallest of the three. For smooth objects, one also expects that $r_1 \leq r_2 \leq r_3$, and the two aspect ratios (r_1/r_2, r_2/r_3) give an idea of the shape of the object. Ideal spheres, tubes, sheets and ribbons have aspect ratios of the order of $(1, 1), (1, 0), (0, 1)$ and $(0, 0)$, respectively (Moisy & Jiménez, 2004), but the shapes of non-smooth objects can be very different from those ideal ones. For example, it is not always true that $r_2 < r_3$, even approximately, as can be seen by considering a large piece of cloth packed into a small box. The ratio r_2/r_3 characterizes the amount of 'wrinkling' of the object, but there are relatively few cases among our Q^-s and clusters in which the smooth ordering is not satisfied. The p.d.f.s of the aspect ratios for the attached Q^-s and clusters are shown in figures 3.11(*a*) and 3.11(*b*), respectively. Both types of objects change from being tubes or ribbons in the buffer and lower logarithmic layers, to fuller sheets in the center of the channel, although the somewhat larger values of r_1/r_2 of the Qs confirm their slightly fuller shapes.

We gave in §3.3 typical intrinsic lengths for the detached Qs, which were of the order of the Kolmogorov scale, presumably making them smooth objects. Their aspect ratios, $(r_1/r_2,\, r_2/r_3) \approx (0.5,\, 0.3)$, put them in the class of elongated ellipsoids, or 'flakes', fuller than the attached Q^-s or clusters (figure 3.11a).

Figure 3.11(*c*) shows the evolution with height of the average lengths of the attached Q^-s. Somewhat surprisingly, the inner length, $r_1/\eta \approx 5 - 15$, is of the order of the local Kolmogorov scale, suggesting that even these larger structures of a large-scale quantity, such as the Reynolds stress, are shells formed from viscous-scale subunits. The ratio r_1/η increases slowly with the distance from the wall, and it can be shown that its probability distribution is fairly narrow at each wall distance, as opposed to the wide tails of figure 3.4(*a*). The other two lengths grow approximately linearly with y, except in the buffer layer. The largest one, $r_3 \approx 2.5\Delta_y$, agrees roughly with Δ_x in the logarithmic layer,

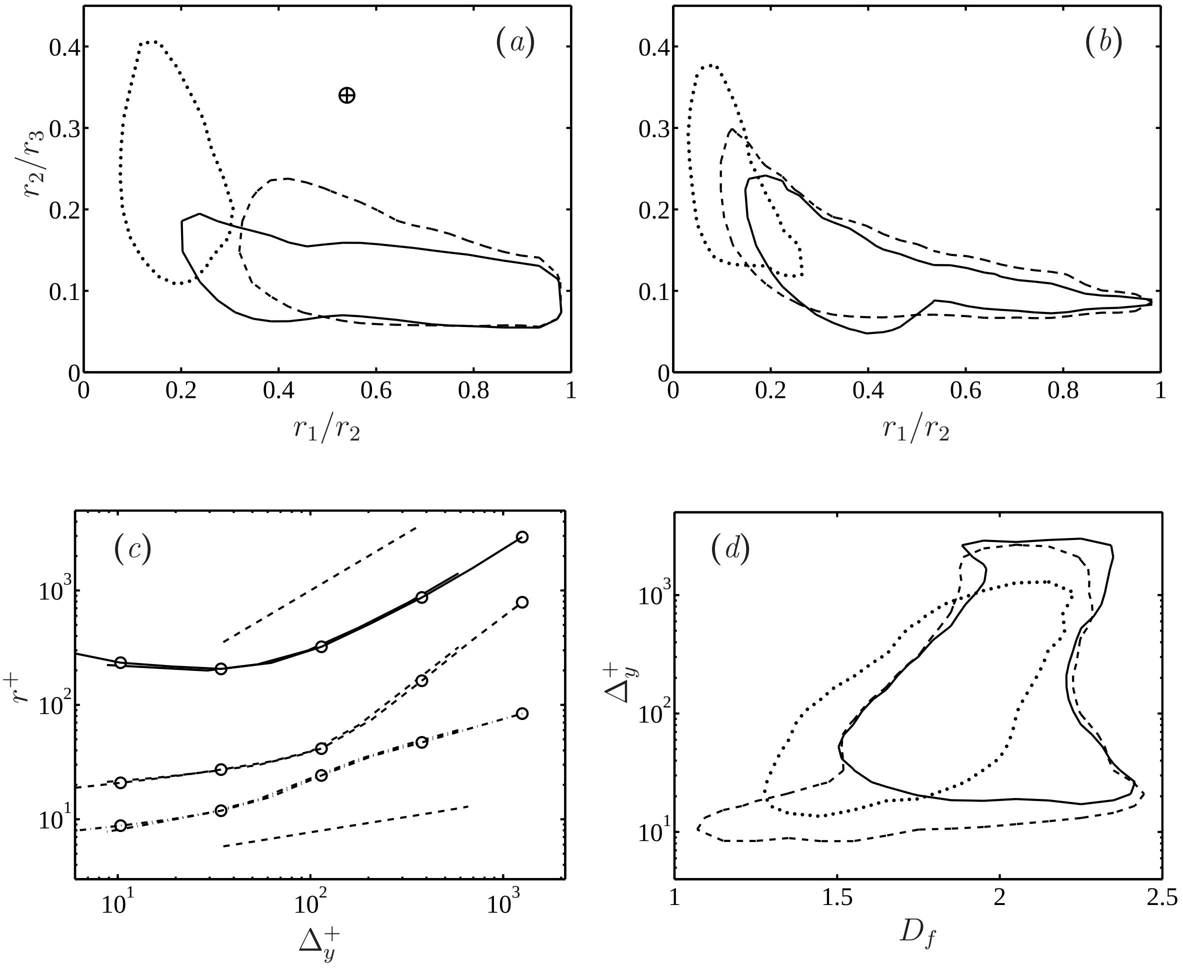

Figure 3.11: (a) Probability density functions of the aspect ratios r_1/r_2 and r_2/r_3 for attached Q$^-$s. ——, Buffer layer; – – –, logarithmic; ········, outer. Probability contours include 50% of the data. $\oplus$, average aspect ratios of the detached Qs. (b) As in (a), for attached clusters. (c) Intrinsic lengths of the attached Qs. –·–·–, r_1; – – –, r_2; ——, r_3. Lines with symbols are L2000; those without symbols are L950. The lower dashed straight line is 3η, and the upper one $10\Delta_y$. (d) Joint histogram of the fractal dimension and Δ_y^+, normalized with the maximum at each Δ_y. ——, Q2; – – –, Q4, ········; clusters. Probability contours include 90% of the data. Figures (a), (b) and (d) are L2000.

but the intermediate one, $r_2 \approx 0.5\Delta_y$, is smaller than Δ_z. The implied shapes change from tubes, or narrow ribbons, in the buffer layer, to increasingly wrinkled sheets away from the wall. They are moderately elongated streamwise, of sizes of the order of the integral scale, but their small, perhaps viscous, thickness suggests that they are formed by connecting subunits similar to the detached Qs.

The ratio r_2/r_3 increases with increasing y, suggesting that the wrinkling increases with increasing size, as expected. That was confirmed by counting the number of discrete intersections (n_I) of random lines aligned with each coordinate axis within the circumscribing boxes of individual objects. It turns out to be proportional to $\Delta_y^{+1/2}$ along the three coordinate axes, implying mean distances between intersections of the order of $\Delta_y^{+1/2} \propto \lambda^+$. That recalls the scaling of the detached Qs discussed in §3.3.1, and probably has a similar origin. In fact, if the volume of each subunit is estimated by dividing the total volume of the Qs, which is proportional to $\Delta_y^{+2.25}$, by n_I^3, the result is $\Delta_y^{+0.75} \propto \eta^{+3}$, which is consistent with the dimensions given above for the detached objects. The resulting model for the attached Qs is a sponge-like object formed by the agglutination of ellipsoidal flakes similar to the detached Qs, most of which are of the order of the Kolmogorov scale, but which span a wide range of sizes. The examples shown in figures 3.10(*c*)-(*d*) support this model of a 'sponge of flakes', in the same way that figure 3.10(*b*) suggests that vortex clusters are 'sponges of strings'.

Following Moisy & Jiménez (2004), the fractal dimension of individual objects can be statistically estimated by box counting within their bounding boxes. Each object is circumscribed within a cube of side r_3, which is then divided into smaller cubes of size r. The number $N_c(r)$ of cubes containing at least one point of the object is then counted. If we can approximate $N_c(r) \propto r^{-D_f}$ for $r_1 < r < r_3$, the exponent D_f can be considered as the fractal dimension of the individual object.

Figure 3.11(*d*) shows the joint histogram of D_f and Δ_y, and is roughly consistent with the discussion above. The dimension increases slightly with the height of the Qs and clusters, with a wide distribution between $D_f = 1$ and $D_f = 2$ in the buffer layer, increasing towards $D_f \approx 2$ away from the wall. As above, the dimension of the clusters is slightly lower than for the Qs. The fractal dimension of the Qs suggests a shell, but we have just seen that it has to be a very corrugated one. Note that the dimensions in figure 3.11(*d*) are lower than those obtained above from the evolution of the volume with height. The reason is that the objects become thicker as they become taller. We showed in §3.2 that the Kolmogorov scale increases in the logarithmic layer as $y^{1/4}$. The volume of a 'sheet' of dimension D_f, with outer scale Δ_y and thickness η, is proportional to $\Delta_y^{D_f}\eta^{3-D_f}$. Substituting $\eta \propto \Delta_y^{1/4}$, we obtain $V_Q \propto \Delta_y^{\alpha}$, and

$$\alpha = \frac{3}{4}(D_f + 1). \tag{3.13}$$

Taking, from figure 3.11(*d*), $D_f = 1.7$ for clusters, and $D_f = 2$ for Qs, we obtain $\alpha = 2$ and $\alpha = 2.25$, respectively, in reasonable agreement with the results of figure 3.10(*a*) for the Q$^-$s, and of del Álamo *et al.* (2006) for the clusters.

Using a DNS of isotropic turbulence, Bermejo-Moreno & Pullin (2008) characterized the geometry of eddies of a passive scalar as blobs or tubes for the larger scales, and as sheets for the smaller ones, which could be construed as being related to the present results. However, beside referring to a different flow and variable, the Qs described here are conceptually different from the objects discussed by those authors. Our Qs coexist in physical space without intersecting each other, while they filter their fields before analyzing them, with the result that their small-scale objects are engulfed within their large-scale ones. One of the conclusions of the discussion above should be that different small-scale quantities have different geometries (see also Moisy & Jiménez, 2004), and our results and those of Bermejo-Moreno & Pullin (2008) are probably unrelated.

3.5.1 Topology of the coherent structures

In this section, we use the genus to characterize the topology of the coherent structures. The genus is a topologically invariant property of a surface defined as the largest number of non-intersecting simple closed curves that can be drawn on the surface without separating it. The genus is negative when applied to a group of several isolated surfaces, since it is considered that no closed curves are required to separate them. Both spheres and discs have genus zero, while a torus has genus one. On the other hand, two separated spheres or the surfaces defined by a sphere shell (or sphere with a cavity) has genus minus one. For a set of objects in a given region, the genus is equal to the *number of holes - number of objects - number of internal cavities*+1. The concept is also defined for higher dimensions but the present section is restricted to two-dimensional surfaces embedded in a three-dimensional space. In integral geometry, the genus is part of a larger set of Galilean invariants called the Minkowski functionals, which characterize the global aspects of a structure in a *n*-dimensional space. The genus is also closely related with the Betti numbers, and more details can be found in Thompson (1996).

The method used to numerically compute the genus of the structures is the fast and memory-efficient algorithm presented by Lozano-Durán & Borrell (2015), which makes

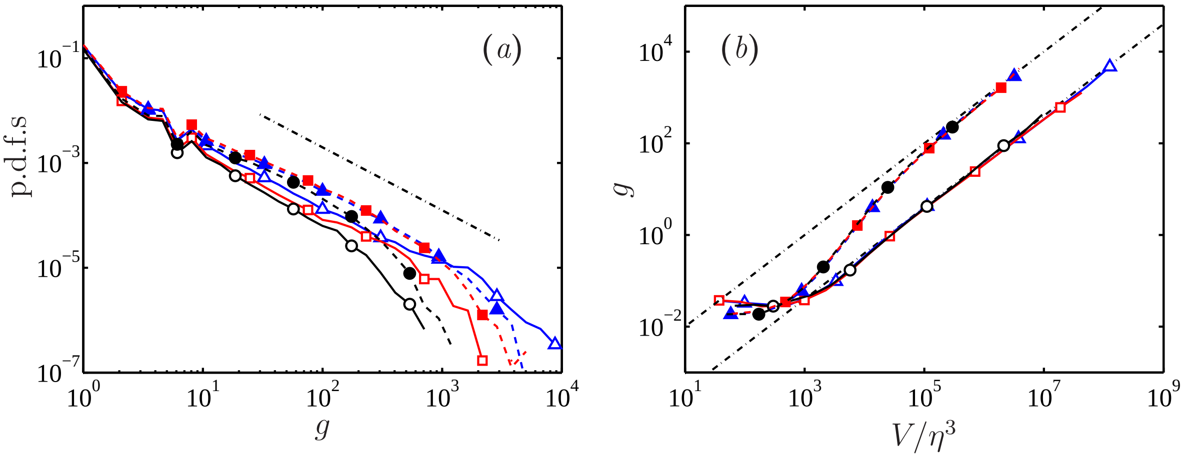

Figure 3.12: (*a*) Probability density functions of the genus g. The dashed-dotted line is proportional to $g^{-1.2}$. (*b*) Average number of holes (genus) of individual coherent structures as a function of their volume, V, in Kolmogorov units. The dashed-dotted lines are $g = 10^{-3}\eta^{-3}(V/\eta^3)$ and $g = 4 \times 10^{-5}\eta^{-3}(V/\eta^3)$. For (*a*) and (*b*), the solid lines with open symbols correspond to Qs and the dashed lines with closed symbols to vortex clusters. Different symbols stand for different Reynolds numbers; ○, $Re_\tau = 934$; □, $Re_\tau = 2004$; △, $Re_\tau = 4180$, which correspond to cases M950, M2000 and M4200 from table 2.1.

the present analysis feasible from a computational point of view. Figure 3.2 shows several examples of actual objects extracted from the flow and demonstrates the complex geometries that may appear. The data reveals that only 0.05% of objects have negative genus, suggesting that most of structures are solid objects with few or no internal cavities. This was reassured by counting the number of internal cavities of the structures. In this scenario, genus and number of holes can be used interchangeably.

The probability density functions of the genus, g, are presented in figure 3.12(*a*) and most of the values concentrate around zero or a few holes, although the long potential tails reach values up to 10^4 holes. Figure 3.12(*b*) shows the average number of holes in the objects as a function of their volume, V, normalized in Kolmogorov units. It becomes clear that as the volume of the structures increases, so does the genus, which is reasonable if we consider that the volume of the object is related to its internal Reynolds number (or complexity), and increasing its volume results in more complicated topologies. The curves for both vortex clusters and Qs show good collapse for the three Reynolds numbers and follow the trend $g = \rho_h V$, with ρ_h a constant equal to $10^{-3}\eta^{-3}$ and $4 \times 10^{-5}\eta^{-3}$ for vortex clusters and Qs respectively.

From relation $g = \rho_h V$, the genus may be understood as an alternative method to characterize the level of complexity of the structures, with ρ_h a density equal to the number of holes per unit volume. If we define l as the average distance between holes within the structures, its value may be approximated by $l \approx (10^{-3})^{-1/\alpha_c}\eta \approx 30\eta$ for vortex clusters and $l \approx (4 \times 10^{-5})^{-1/\alpha_Q}\eta \approx 90\eta$ for Qs, with $\alpha_c = 2$ and $\alpha_Q = 2.25$ the fractal dimensions for vortex clusters and Qs, respectively, computed in the previous section. These lengths are consistent with the model of coherent structures built mostly by small blocks of length $30 - 90\eta$ stacked together to create larger objects but not perfectly compacted which results in holes between the blocks. For a given volume, V, vortex clusters have on average 25 times more holes than Qs, suggesting that their blocks and connections are fundamentally different. This is consistent with the results above where the Qs are flake-shaped while vortex clusters are worm-shaped, also visible in figure 3.2.

3.6 Spatial organization

We discuss now the relative positions of the objects characterized in the previous sections. Consider first the relation between clusters and Q2s, which were shown by del Álamo *et al.* (2006) to be statistical markers for each other. As in §3.4, we only consider that two objects are related if their heights differ by less than a factor of two.

Figure 3.13(a) shows that more than 80% of the clusters intersect with at least one Q^-, at all heights. The converse is not true, and the probability that a Q^- intersects a cluster is only high near the wall. It decays further up, together with the density of clusters, essentially because there are not enough tall clusters to cover all the tall Q^-s.

Figure 3.13(b) contains the p.d.f.s of the fraction of the volume of the box of each attached cluster that is covered by boxes containing Q2s or Q4s, and addresses the question of how relevant are the intersections between Q^-s and clusters. The figure is drawn for the logarithmic region of L2000, but similar results hold for L950 and for other heights. In theory, the intersected fraction f_A can be greater than one, because the boxes of the Qs may overlap, and some parts of the cluster can be covered by more than one Q. Figure 3.13(b) shows that the p.d.f.s drop sharply beyond $f_A = 1$, indicating that those cases are rare. Note that the discreet peak at $f_A = 1$ is an artifact of considering covering fractions.[*] It is clear from the figure that the intersections of clusters with Q2s are more probable than with Q4s, in agreement with figure 3.5(b). Moreover, to test whether those

---

[*] Lets consider a system with two boxes A and B, where the relative positions of the boxes are random and where the box B is larger than box A. The probability of the box A being completely covered by box B ($f_A = 1$) is proportional to a triple-infinitude of relative positions. But the probability of any other covering fraction is proportional to a double-infinitude, the positions resulting of moving box B over the surface of box A.

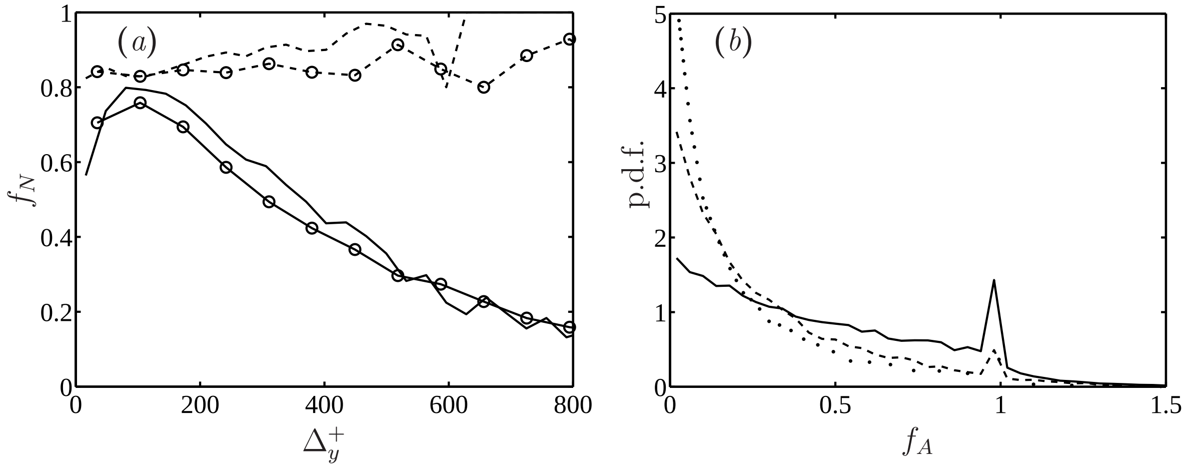

Figure 3.13: (*a*) Fraction of clusters (Q$^-$s) whose boxes are intersected by one or more boxes of a Q$^-$ (cluster), as function of their Δ_y. ——, Qs; – – –, clusters. Lines without symbols are L950, those with symbols are L2000. (*b*) Probability density function of the fraction of the volume of cluster boxes that is filled by intersecting boxes of Q$^-$s. Case L2000, for clusters in the logarithmic layer. ——, Q2s; – – –, Q4s; ········, randomized Q$^-$s.

intersections are just a statistical consequence of the areas covered by the different objects, we recomputed their statistics after randomizing the $x - z$ positions of the centers of the boxes of the Q$^-$s. The resulting p.d.f. is very close to that of the Q4s, supporting the idea that their intersections with the clusters are mostly a matter of chance, while those of the Q2s are not.

We analyze next the relative positions of different objects, defining joint p.d.f.s, $J^{(ij)}(\delta_x, \delta_z)$, for the position of events of type j with respect to those of type i, where i and j are 2 for Q2s, 4 for Q4s and C for clusters. The relative distances

$$\delta_x = 2\frac{x^{(j)} - x^{(i)}}{d^{(j)} + d^{(i)}} \qquad \text{and} \qquad \delta_z = 2\frac{z^{(j)} - z^{(i)}}{d^{(j)} + d^{(i)}}, \tag{3.14}$$

are referenced to the position of i-objects, $(x^{(i)}, z^{(i)})$, and are normalized with the semisum of the wall-parallel diagonals of each pair of events,

$$d^{(i)} = \sqrt{\Delta_x^{(i)2} + \Delta_z^{(i)2}}. \tag{3.15}$$

The spanwise statistical symmetry of the flow allows us to choose the direction of the δ_z axis for each individual reference event. In p.d.f.s involving only Qs, such as figures 3.14(*a*), 3.14(*b*) and 3.14(*d*), $\delta_z > 0$ is chosen pointing to the nearest Q of different kind than the reference. For the p.d.f.s of the positions of clusters with respect to Qs, such as figures 3.14(*e*) and 3.14(*f*), $\delta_z > 0$ points towards the closest cluster. That choice weights the p.d.f.s towards the positive δ_z, but allows us to test the symmetry of individual groups of events. For example, if Q2s were typically surrounded by two roughly equivalent Q4s, as in a symmetric trio, the p.d.f. of the positions of Q4s with respect to Q2s would have a secondary peak with negative δ_z, in addition to the primary one with $\delta_z > 0$. Weaker secondary peaks correspond to statistically more one-sided associations.

Figure 3.14 shows the p.d.f.s for reference objects within the logarithmic region, with probability isolines normalized with $J_\infty^{(ij)}$, which is the average value of the p.d.f. for $\delta_x^2 + \delta_z^2 > 9$. The three distributions for pairs of objects of the same type, figures 3.14(a) to 3.14(c), show that they tend to be aligned in the streamwise direction, and that the objects do not overlap, as shown by the low probabilities at $\delta_x = 0$. The Q$^-$s tend to be spaced longitudinally by $|\delta_x| \approx 1$, with the probability of finding another Q of the same kind in that position being more than twice the probability of finding it anywhere else. The clusters also align longitudinally, but tend to be a little closer than the Qs, $|\delta_x| \approx 0.75$. That means that they almost overlap each other, and is consistent with the discussion in the previous sections that the Qs are slightly fuller objects than the clusters.

Objects of different kinds tend to align spanwise, rather than streamwise. Figure 3.14(d) shows that the most probable position of the Q4s with respect to the Q2s is to one side of the Q2, and very close to it, suggesting that both events tend to form parallel pairs. Our choice of the sign of δ_z requires the closest Q4 to be at $\delta_z > 0$, but the lack of any peak at $\delta_z < 0$ (where the probability of finding a Q4 is actually lower than the average) strongly implies one-sided pairs, rather than symmetric hairpins. Although not shown, $J^{(42)}$ is similar to $J^{(24)}$, because the Q2s and Q4s have roughly the same density and size distribution throughout the logarithmic layer.

The p.d.f. of the relative position of the clusters with respect to the Q2s is presented in figure 3.14(e), and shows that they tend to be embedded within Q2s of similar sizes, in agreement with figure 3.5(a), and with the conditional velocity fields in del Álamo *et al.* (2006). Figure 3.14(f) reinforces that conclusion, because the clusters are in $\delta_z > 0$ with respect to the Q4s, which is also the preferred location of the Q2s.

The picture that emerges is one of spanwise pairs of Q2s and Q4s, with a cluster associated with the Q2, and with the groups aligned streamwise. The p.d.f.s in figure 3.14, including the existence of pairs and the streamwise distance between neighboring Q$^-$s, are robust with respect to the eduction threshold. They change little in $1 < H < 3$, implying that the pairs are distinct units rather than random pieces of longer objects. The statistical evidence for pairs of Q2s and Q4s is also strong. Roughly 50% of the Q$^-$s in the logarithmic region are involved in simple pairs, and 30% are involved in more

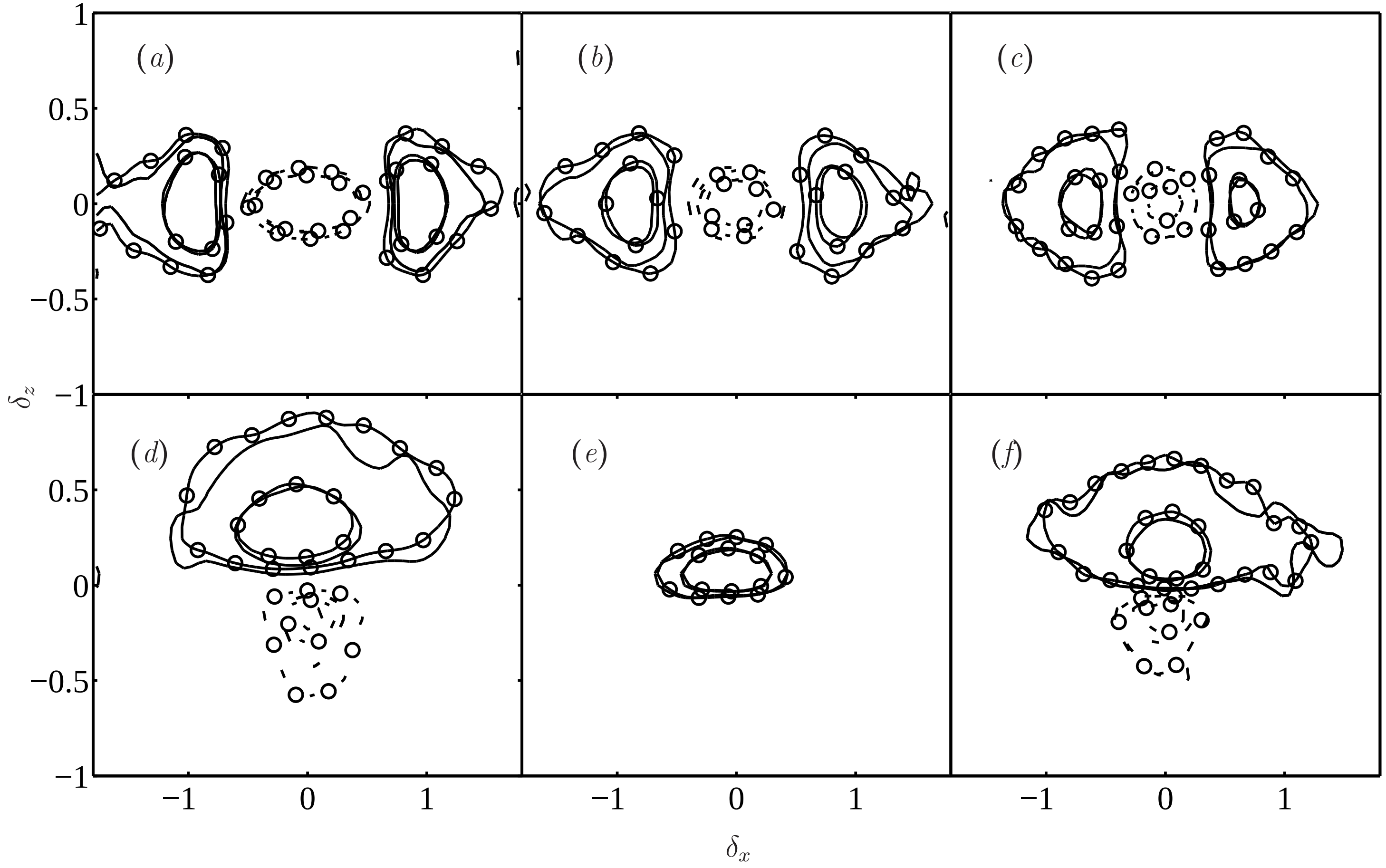

Figure 3.14: Probability density functions of the relative positions of clusters, Q2s and Q4s, using as reference events in the logarithmic layer. (*a*) J^{22}. (*b*) J^{44}. (*c*) J^{CC}. (*d*) J^{24}. (*e*) J^{2C}. (*f*) J^{4C}. Solid contours are $J^{(ij)}/J^{(ij)}_{\delta,\infty} = 1.5$ and 2. Dashed contours are $J^{(ij)}/J^{(ij)}_{\delta,\infty} = 0.66$ and 0.5. Lines without symbols are L950, and those with symbols L2000.

complicated trios or groupings. The rest are isolated.

3.6.1 Sweep-ejection pairs

Figure 3.15 shows the average flow field conditioned to the presence of a Q2–Q4 pair, which is defined whenever a Q2 has a neighboring Q4 that satisfies the relative-height condition (3.12), and is within

$$|\delta_x| < 1.25 \qquad \text{and} \qquad |\delta_z| < 0.75. \tag{3.16}$$

Very similar results are obtained when the pair is defined as a Q4 with a neighboring Q2. The conditional averages are then computed in the reference frame

$$\boldsymbol{r} = 2\,(\boldsymbol{x} - \boldsymbol{x}^{(24)})/\Delta_y^{(24)}, \tag{3.17}$$

where $\boldsymbol{x}^{(24)}$ is the midpoint of the line connecting the centers of the circumscribing boxes of the two Qs, and $\Delta_y^{(24)} = (\Delta_y^{(2)} + \Delta_y^{(4)})/2$ is the semi-sum of their vertical sizes. The axes are chosen so that $r_z > 0$ for the Q4.

Figure 3.15(*a*) shows the average shape of the pair and its associated cluster. As expected, the aspect ratios of this conditional object, approximately $4 \times 1 \times 1.5$ in the coordinate directions, are consistent with the p.d.f.s shown in figure 3.6, with two parallel Q^-s. The cluster is mostly lodged within the Q2, but it extends into the shear layer underneath the Q4. Note that the Q-pair is one-sided. No effort was made to prevent the formation of a conditional trio involving a second Q4 or Q2, but they did not appear in the statistics. Even so, and as we have already mentioned, the smooth conditional shape in this figure is not representative of the individual pairs of the flow, which are more complex. An example is given in figure 3.15(*b*). It should be stressed again that while the average flow field in figure 3.15(*a*) is consistent with an asymetric hairpin, the instantaneous pair is not.

Figure 3.15(*c*) shows the conditional streamwise velocity perturbation associated to the Q2–Q4 pairs. It has two streaks, elongated in the x direction, in qualitative agreement with the conical wakes reported by del Álamo *et al.* (2006) in the velocity fields conditioned to attached clusters. However, the figure shows that the two streaks are very different. For the isosurfaces used in the figure, the low-velocity object is only about as tall as the Q2, but the high-velocity perturbation is much larger, longer and taller than its associated Q4. The Q2 and its low-velocity streak seem to be engulfed within the larger high-velocity region. That is seen even more clearly in the cross-section in figure 3.15(*d*). As mentioned above, the velocity field obtained when the pair is defined with respect to the Q4, instead

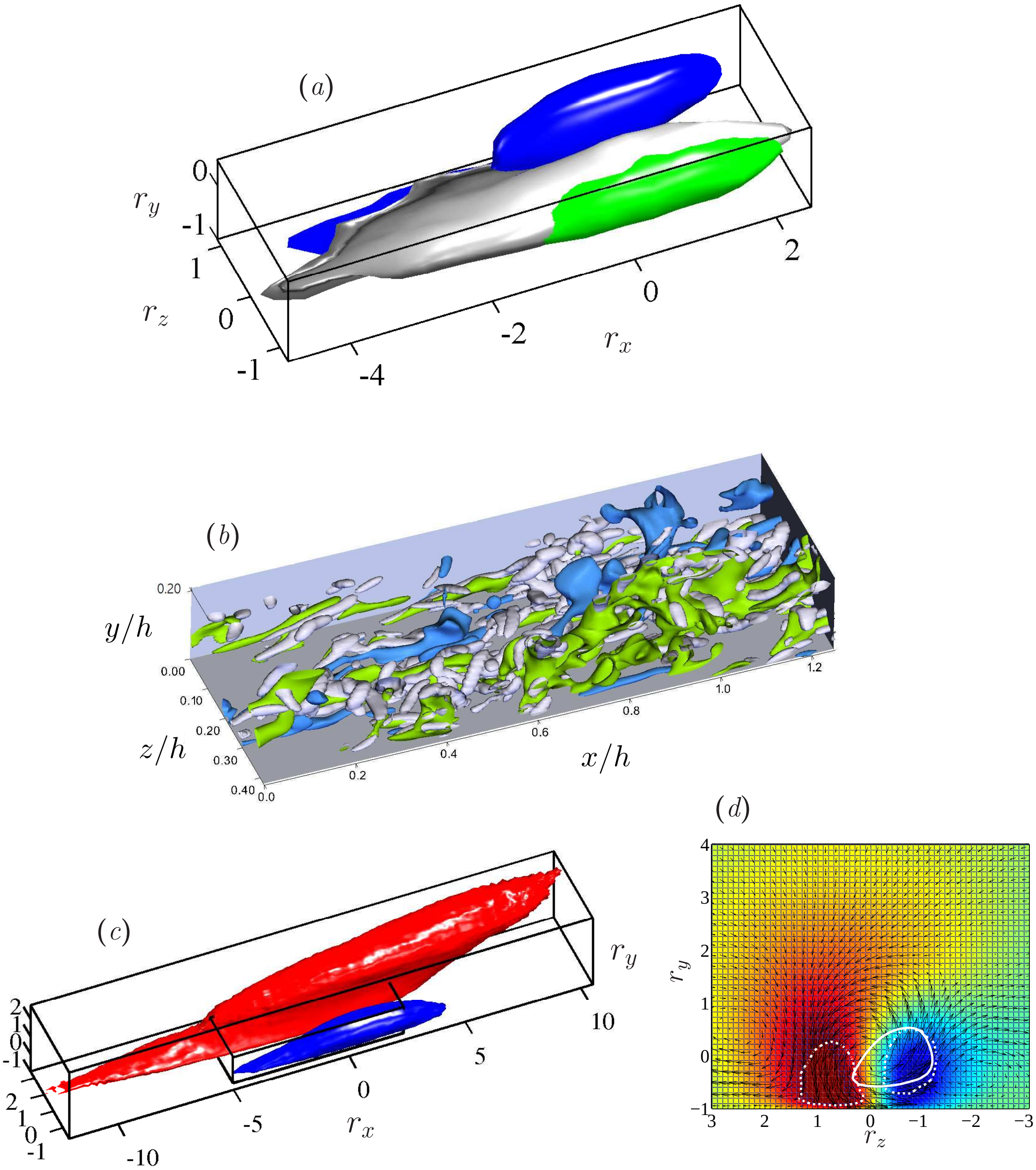

Figure 3.15: Flow fields conditioned to attached Q2–Q4 pairs in the logarithmic layer. Data for L2000. (*a*) P.d.f.s of the points belonging to the Q2 (green), Q4 (blue) and clusters (grey). The isosurfaces plotted are 0.75 times the maximum value of the p.d.f.s for the Qs, and 0.85 for the cluster. (*b*) Example of an instantaneous Q2–Q4 pair. Color code as in (*a*). (*c*) Conditional streamwise perturbation velocity. The blue object is the low-speed isosurface, $u = -0.5u_\tau$. The red one is $+0.5u_\tau$. The heavy parallelepiped is a tight box around the conditional object in (*a*). The flow in (*a*) to (*c*) is from bottom-left to top-right. (*d*) Cross section of the conditional field in (*c*) at $r_x = 0$. The arrows are the cross flow (v, w), and the shaded map is the streamwise velocity ($u < 0$ in blue, $u > 0$ in red). The white dotted lines are 0.75 times the maximum value of the p.d.f. of the points belonging to the reference Q pair. The white solid line is 0.85 times the maximum value of the p.d.f. of the points belonging to the cluster.

of the Q2, is very similar to the one in figures 3.15(*c*) and 3.15(*d*), and does not differ too much from those obtained when conditioning on all Q2s or Q4s, confirming that most Q^-s are parts of pairs.

Similar findings were reported by Kim (1985) using the VITA technique in the buffer region, and by Ganapathisubramani (2008) for sinks of momentum, both at $y^+ \approx 100$ and at $y \approx 0.5h$. The low-velocity object lodged underneath the high-velocity overhang in figures 3.15(*c*) and 3.15(*d*) is clearly the same phenomenon as the low-velocity 'ramps' seen by many investigators in streamwise sections of the velocity field (e.g., Meinhart & Adrian, 1995). Flores *et al.* (2007) noted that those ramps are actually long cylindrical tubes or cones, and figure 3.15(*c*) is most probably a conditional picture of a side-wall of such a tube.

It was argued in del Álamo *et al.* (2006) that the clusters are too small to have created the low-velocity streak associated with them, and that they are probably a consequence of the streak, rather than a cause. That should probably now be rephrased as that they are a consequence of the Q2. Figures 3.15(*c*) and 3.15(*d*) suggest that even the low-speed streak is conditioned by the presence of a pre-existing larger sweep, which either creates it, or, more probably, preferentially influences the location of the Q-pairs and clusters that serve to condition the figures.

3.6.2 Large-scale organization

The results presented up to now suggest that the building block of the Reynolds stresses is a pair of attached Q2s and Q4s, with a vortex cluster embedded within the Q2. The aspect ratios of those units are of the right order of magnitude for them to become comparable, when $\Delta_y \approx h$, to the large-scale-motions defined by Adrian (2007). They are the best candidates that we have for the attached eddy hierarchy postulated by Townsend (1976).

On the other hand, they do not hint at a mechanism by which such structures, of size $O(h)$, can give rise to the very-long coherent structures ($\Delta_x \approx 20h$) in the central part of the channel, such as the one in figure 3.10(*d*). Moreover, the procedure that we have used to identify them does not make use of the streamwise alignment detected in figure 3.14, suggesting that some undetected organization could exist at even larger scales. The only conditional structure detected up to now longer than a single Q is the high-velocity streak in figure 3.15(*c*).

It is tempting to explore the existence of 'supergroups' formed by Qs and clusters under somewhat laxer relational rules, but our attempts to extract physical meaning from such groups were not successful. It is very easy to form them by defining two objects as connected when they satisfy (3.16). Moreover, even if we enforce our usual rule that two objects can only be related if their heights differ by less than a factor of two, a supergroup can be formed with objects of many sizes, connected by intermediate chains of structures that differ little from their neighbors.

Such supergroups are longer and taller than individual Q^-s or clusters, and have statistical properties that can be interpreted as self-similar, although their aspect ratios, $8 \times 1 \times 2$ are only marginally more elongated than the single Q-pairs, and do not explain the longer global modes. In fact, although figure 3.14 proves the streamwise alignment of the pairs, the range of that ordering is not very long. Of the Q^-s in the logarithmic layer, roughly 55% have another Q in front or behind, but only 13% have both.

Moreover, most of the definite properties of the supergroups are retained when the positions of the Qs and clusters are randomized before they are allowed to connect, suggesting that the supergroups are little more than random juxtapositions of unrelated units, whose properties are determined by the volume fractions occupied by the different objects. They will not be discussed further.

It is interesting to mention at this point that recent visualization work suggests that the very-long structures mentioned above may be an exclusive feature of internal flows, and are not present in turbulent boundary layers (Hutchins *et al.*, 2011; Dennis & Nickels, 2011*a*,*b*; Lee & Sung, 2011). Although generally using more limited statistics than those in the present work, the three groups find that the longest structures in boundary layers have $\Delta_x \approx 6h$, and do not reach above $\Delta_y \approx 0.5h$. We have seen that the largest structures in channels extend well across the mid-plane, but Jiménez *et al.* (2010) already noted that boundary layers are shorter than channels, and showed that many of the differences between the two flows are due to the effect of turbulent/irrotational intermittency in the corrugated edge of the boundary layer. That the wall-normal extent found in the papers just mentioned roughly coincides with the lower edge of the intermittent layer suggests that it may also be the interaction with irrotational fluid that limits the growth of the structures. The largest structures in boundary layers would not then be much longer than the self-similar attached eddies discussed in the previous sections, and the problem with very-large-scale alignment would be exclusive to pipes and channels.

3.7 Conclusions

We have generalized to three dimensions the quadrant analysis of the intense Q events that contribute most to the tangential Reynolds stress in plane turbulent channels, with special emphasis on the logarithmic and outer layers. We have shown that they separate into wall-attached and wall-detached families.

The detached objects represent background fluctuations of the tangential Reynolds stress. They are isotropically oriented, and their contributions to the mean Reynolds stress cancel. Their dimensions and intensities are very similar to the strong fluctuations of the Reynolds stress in experimental flows with little mean momentum transport. Even in our turbulent channels, or in the atmospheric surface layer, the r.m.s. amplitude of the τ fluctuations is 2.5–3 times larger than their mean. Those detached Qs are small, with sizes that, at least at our Reynolds numbers, are of the order of a few Kolmogorov lengths.

The wall-attached Q^-s are larger, and carry most of the mean tangential Reynolds stress. At the identification threshold, $H = 1.75$, they only fill 8% of the volume of our channels, but they are responsible for roughly 60% of the total Reynolds stresses at all wall-distances. Most of the wall-attached events are sweeps or ejections, and form a self-similar family with aspect ratios $\Delta_x \approx 3\Delta_y$ and $\Delta_z \approx \Delta_y$, which agree well with the known dimensions of the uv cospectrum. There are very few attached 'countergradient' Q1s or Q3s.

When the Qs are extracted from one-dimensional sections of either our channels or experimental shear flows, their lengths appear to scale with the local Taylor microscale, but closer inspection reveals that they really span a wide range of scales, from the Kolmogorov to the integral length, and that the average length is not a representative quantity. In the channels, where objects can be classified in terms of their overall connected sizes, the thickness of objects in a given size class is more narrowly defined, suggesting that longer one-dimensional Qs also correspond statistically to larger three-dimensional objects in the experimental flows.

In fact, the similarities among the distributions of the one-dimensional Q surrogates in the very different shear flows in table 3.3 suggest that the fluctuations of the Reynolds stress are similar for all such flows at sufficiently high Reynolds numbers. In wall-bounded turbulence, the attached structures would simply be large fluctuations that reach the wall, because of their size, where they are modified by the inhomogeneity of the mean velocity profile.

The number of attached Q^-s decays away from the wall as Δ_y^{-2}. Since their wall-parallel area increases as Δ_y^2, the area covered by Q^-s of a given size is independent of Δ_y, and so is the fraction of the Reynolds stress carried by them. On the other hand, the volume fraction filled by the Q^-s increases with their size. Roughly 60% of the total volume of the attached Q^-s is concentrated in a few very large Q2s that extend into the opposite half of the channel across the central plane. Those objects, with lengths of the order of $20h$ in our simulations, are probably the same as the very-large-scale structures discussed by several authors. They are visually composite objects, formed by the concatenation of smaller subunits, and do not form part of the self-similar family mentioned above.

The dimensions of the self-similar attached Q^-s are similar to those of the attached vortex clusters discussed by del Álamo *et al.* (2006). Most clusters are associated with at least one Q2, although the converse is not true. The number of attached clusters decays faster than the Qs, as Δ_y^{-3}, and the taller Qs do not have associated clusters.

The individual Q^-s have fractal dimensions of the order of $D_f = 2$, slightly fuller than the clusters, whose dimension is $D_f \approx 1.7$. The thickness of their shells is 10–15 times the Kolmogorov length, at our Reynolds numbers, and they become more complicated as their sizes increase, suggesting that they might be described as 'sponges of flakes', in the same way that the vortex clusters might be described as 'sponges of strings'. Examples of both are given in figures 3.10 and 3.15.

Most of the Q2s and Q4s are grouped into side-by-side parallel pairs, mostly one-sided rather than symmetric trios. The predominant structure is formed by one such pair with a vortex cluster embedded within the base of the Q2 and underneath the Q4. As with the individual objects, the groups are self-similar, with aspect ratios $\Delta_x \approx 4\Delta_y$ and $\Delta_z \approx 1.5\Delta_y$. It is conjectured that those objects are the attached eddies of Townsend (1976), with which they share the dimensions and the stresses. The conditional velocity field around them shows that they are preferentially located in the side-walls separating a low-velocity streak lodged underneath a larger high-velocity structure, which most probably coincides with the low-momentum ramps discussed by various authors.

The attached eddies tend to be aligned longitudinally with each other, but that organization does not extend far enough to explain the very long structures in the center of the channel. Although roughly 55% of the Q^-s have another Q in front or behind, only 13% have both. Attempts to identify larger super-groups that could explain the formation of the very-large-scale structures failed beyond what could be expected from purely random associations, and did not reach the required aspect ratios, although some evidence is cited that this might only be a problem in internal turbulent flows.

Our simulations cover a factor of two (or four in some cases) in friction Reynolds numbers, in the range of many of the available experiments. The scalings that we have used in the figures are those that result in the best collapse of our simulations, and they are usually not ambiguous. Although it is dangerous to extrapolate beyond the range of the available data, that collapse suggests that our conclusions may apply to a wider range of Re_τ.

Chapter 4

Time-resolved evolution of coherent structures [*]

4.1 Introduction

The research on coherent structures in turbulence relies on the notion that there is a set of eddies that are representative enough of the dynamics of the flow that their understanding would result in important insights into the mechanics of turbulence. In recent years, the steady increase in computer power has allowed the study of instantaneous three-dimensional coherent structures extracted from DNSs. However, their dynamics can only be fully understood by tracking them in time. Although the temporal evolution of structures in wall-bounded flow has already been studied for small eddies at moderate Reynolds numbers (e.g., Robinson, 1991; Johansson *et al.*, 1991), a temporal analysis of the three-dimensional structures spanning from the smallest to the largest scales across the logarithmic layer, using non-marginal Reynolds numbers is still missing. Our goal in the present chapter is to perform such analysis and study the dynamics of turbulent channel flows in terms of the time-resolved evolution of coherent structures, with particular emphasis on the logarithmic layer. We describe the tracking method, summarize the properties of the three-dimensional eddies described in the previous chapter, and characterize their temporal evolution and interactions.

The efforts to describe wall-bounded turbulence in terms of coherent motions date at least to the work of Theodorsen (1952), but it was not until the experimental visualization of sublayer streaks in boundary layers by Kline *et al.* (1967), of fluid ejections by Corino

---

[*] Part of the contents of this chapter have been published in the *Journal of Fluid Mechanics*, volume 759, pages 432–471, with Javier Jiménez as coauthor.

& Brodkey (1969), and of large coherent structures in free-shear layers by Brown & Roshko (1974), that the structural view of turbulence gained wider acceptance. Quadrant analysis was proposed to study regions of intense tangential Reynolds stress in wall-bounded turbulent flows by Wallace *et al.* (1972) and by Willmarth & Lu (1972), and the related VITA (variable interval time average) technique of Blackwelder & Kaplan (1976) was used to identify one-dimensional sections of individual structures from single-point temporal signals, and to define and characterize ejections (Bogard & Tiederman, 1986). The pioneer numerical work by Chong *et al.* (1998) used a thresholding method to visualize coherent structures in wall-bounded flows. Particle-image velocimetry (PIV) experiments in the 90's provided two-dimensional flow sections, and linked the groups of ejections to ramp-like low-momentum regions (Adrian, 1991, 2005). Simultaneously, the increase in computational power and the development of new experimental techniques led to the study of full three-dimensional coherent structures (Robinson, 1991). Some recent works of this type are the characterization of clusters of vortices in simulations by Moisy & Jiménez (2004); Tanahashi *et al.* (2004) and del Álamo *et al.* (2006), the experiments in Dennis & Nickels (2011*a*,*b*), and the generalized three-dimensional quadrant analysis in the previous chapter among others. However, most of these studies are restricted to instantaneous snapshots from which it is difficult to extract dynamical information.

The study of convection velocities is closely linked to that of coherent structures. Kim & Hussain (1993) extracted the streamwise propagation speed of the fluctuations of pressure and velocity in a numerical channel, and concluded that it is approximately equal to the local mean velocity, except in the near-wall region, while Krogstad *et al.* (1998) computed convection velocities in an experimental turbulent boundary layer, and found that coherent motions of the order of the boundary layer thickness convect with the local mean velocity, but that the velocity drops significantly for the smaller scales. Interestingly, del Álamo & Jiménez (2009) found that the small scales in channels travel at approximately the local average velocity, whereas larger ones travel at a more uniform speed roughly equal to the bulk velocity. Since the bulk velocity may be larger or smaller than the local average depending on the distance to the wall, these three results are not necessarily incompatible. The average convection velocity has also been found to depend on the flow variable or structure under consideration. For instance, ejections travel at distinctly lower speeds than sweeps (Guezennec *et al.*, 1989; Krogstad *et al.*, 1998).

The first attempts to measure the lifetimes of vortices date from the experiments in grid turbulence by Cadot *et al.* (1995) and Villermaux *et al.* (1995), although with limited results. The temporal evolution of the velocity fluctuations in the logarithmic layer of turbulent channels was studied by Flores & Jiménez (2010*a*) using minimal boxes, resulting in a scenario that is a more disorganized version of the one in the minimal simulations of the buffer-layer described in Jiménez & Moin (1991). Some preliminary work about the time-resolved evolution of individual structures in a full-sized logarithmic layer may be found in Lozano-Durán & Jiménez (2010) and Lozano-Durán & Jiménez (2011). Those works share some features with previous studies of the dynamics of hairpin vortices, both numerical (Singer & Joslin, 1994; Zhou *et al.*, 1999; Suponitsky *et al.*, 2005) and experimental (Acarlar & Smith, 1987*a*,*b*; Haidari & Smith, 1994). However, while the older works describe the evolution of individual hairpin-like vortices in a laminar flow, although in some cases with a turbulent-like profile, Lozano-Durán & Jiménez (2010); Lozano-Durán & Jiménez (2011) and the present chapter deals with the evolution of actual eddies in fully developed turbulence.

Exploiting a different technique, Elsinga & Marusic (2010) studied the evolution of the invariants of the velocity gradient tensor (Chong *et al.*, 1990; Perry & Chong, 1994; Martín *et al.*, 1998) in the outer part of a turbulent boundary layer, using a dataset of time-resolved three-dimensional velocity fields obtained by tomographic PIV. They found a nearly constant orbital period of the order of tens of eddy turnovers for the conditionally averaged spiral trajectories in the invariant-parameter plane, and interpreted it as a characteristic lifetime of the energy-containing eddies. The same dataset was later used by Elsinga *et al.* (2012) to track vortices in a turbulent boundary layer, and to compute average trajectories and convection velocities. They observed non-negligible wall-normal displacements of the structures during a typical trajectory, and showed that the vortical structures and bulges are transported passively by the external velocity field without significant changes in their topology. The recent work of LeHew *et al.* (2013) also uses time-resolved PIV to examine the structure and evolution of two-dimensional swirling motions in wall-parallel planes of a turbulent boundary layer, which they take to be markers for three-dimensional vortex structures. They measured their convection velocity and lifetime, and found that the latter increases with the wall-normal distance, and that a small percentage of the vortices survive for more than five eddy-turnover times.

These observations have been used to build models for the dynamics of wall-bounded turbulence based on coherent structures. Some of these models were presented in §1.3 and we revisit below some of their main properties. The best developed models refer to the flow near the wall, where the local Reynolds numbers are low, and the flow is smooth enough to speak of simple objects. Examples include the papers by Jiménez & Moin (1991), Jiménez & Pinelli (1999), Schoppa & Hussain (2002) and Kawahara *et al.* (2012), and the reviews by Panton (2001) and McKeon & Sreenivasan (2007). Above the buffer layer, the internal Reynolds number of the eddies is higher, the eddies are themselves turbulent objects, and their characterization is more challenging. A seminal contribution was the attached-eddy model proposed by Townsend (1976) for the logarithmic layer. Generally speaking, there are at present two different models for the dynamical implementation of the Townsend (1976) conceptual framework, both of them hitherto incomplete. The first one is the hairpin-packet paradigm, originally proposed by Adrian *et al.* (2000), based on the horseshoe vortex initially described by Theodorsen (1952) and further developed by Head & Bandyopadhyay (1981), Perry & Chong (1982) and others. According to that model, several hairpin vortices are organized in coherent packets that grow from the wall into the outer region, with lifetimes much longer than their characteristic turnover times (Zhou *et al.*, 1999). The growth of the packets involves several mechanisms, including self-induction, autogeneration, and mergers with other packets, as discussed in Tomkins & Adrian (2003) and reviewed in Adrian (2007). The observed low-momentum regions and ejections are contained within the hairpin packet, and are reflections of the cooperative effect of the hairpins. However, the evidence for hairpin vortices far from the wall is limited, and their origin and evolution remain unclear, specially with regard to how they move away from the wall.

Other models have been proposed in which the importance of the hairpins is questioned. Pirozzoli (2011) studied the organization of vortex tubes around shear layers and concluded that the former are a by-product of the latter, most likely through a Kelvin-Helmholtz instability. In the same line, Bernard (2013) found vortex furrows to be the dominant structural entity in a transitional boundary layer and the hairpins the rotational motion created as a consequence of the furrows. Schlatter *et al.* (2014) showed that transitional hairpin vortices in fully developed turbulent boundary layers do not persist and their dominant appearance in the outer region at high Reynolds numbers is very unlikely. However, the three aforementioned works focus on the buffer layer or their vicinity and do not provide any information about the logarithmic layer and above. A more complete model has been proposed in the previous chapter extending the works by del Álamo *et al.* (2006) and Flores *et al.* (2007), in which the flow in the logarithmic layer is explained in terms of ejections, sweeps and clusters of vortices. Reviews are found in Jiménez (2012, 2013). These structures are intrinsically turbulent and complex objects, in contrast to the simpler hairpins. Ejections and sweeps are grouped into side-by-side parallel pairs, mostly one-sided rather than symmetric trios (see also chapter 3 and Guezennec *et al.*, 1989), and the predominant structure is formed by one such pair, with a vortex cluster embedded within the base of the ejection, and extending underneath the sweep. They are preferentially located in the side-walls of, rather than surrounding, a low-velocity streak lodged besides a taller high-velocity structure, in a configuration that most probably corresponds to the low-momentum ramps discussed by various authors (e.g., Adrian, 1991, 2005). The presence of structures with almost identical features over rough walls (Flores *et al.*, 2007) and in channels without a buffer layer (Mizuno & Jiménez, 2013) suggests that they are generated at all heights, or that, if they are formed at the wall, they quickly forget their origin and reach local equilibrium with the outer layers. Either way, the importance of the wall as the source of eddies is diminished, and is mostly relegated to the role of creating and maintaining the mean shear.

From the kinematic point of view (ignoring the asymmetry reported above for the ejection-sweep pairs), the hairpin packet model by Adrian *et al.* (2000) and the scenario proposed in chapter 3 together with del Álamo *et al.* (2006) and Flores *et al.* (2007), are statistically compatible at the level of one-point velocity statistics and spectra, as shown by Perry & Chong (1982), Perry *et al.* (1986) and Nickels & Marusic (2001) for hairpin packets, and by del Álamo *et al.* (2006) for vortex clusters. Beyond that, the two models are not dynamically equivalent and, while the hairpins are seen as the cause of the low-momentum regions and of the ejections, the clusters of vortices in del Álamo *et al.* (2006) are rather considered consequences of the streaks. This chapter is devoted to clarify this issue by the direct observation of the temporal evolution of the different structures.

The chapter is organized as follows. Section 4.2 describes the numerical experiments and the method employed to identify coherent structures. The tracking method is explained in §4.3. The temporal evolutions of eddies are classified according to different criteria in §4.4, and their geometry analyzed. Their temporal behavior is described in §4.5, their lifetimes in §4.5.1, their birth, death and vertical evolution in §4.5.2 and §4.5.3, and the advection velocities in §4.5.4. Finally, a discussion and conclusions are offered in section 4.6. Two sections at the end of the chapter contain additional information concerning the validation of the tracking procedure and the effect of the parameters chosen.

Case	Re_τ	Re_λ	L_x/h	L_z/h	Δx^+	Δz^+	Δy^+_{max}	Δt^+_s	$T_s u_\tau/h$	Symbol
M950	932	89	2π	π	11	5.7	7.6	0.8	20	○
M2000	2009	126	2π	π	12	6.1	8.9	2.1	11	△
M4200	4164	202	2π	π	12	6.1	10.6	3.5	10	none

Table 4.1: Parameters of the simulations. Re_τ is the Kármán number. The microscale Reynolds number Re_λ is the maximum in each channel, attained in all cases near the upper edge of the logarithmic layer, $y/h \approx 0.4$. L_x and L_z are the streamwise and spanwise dimensions of the numerical box, and h is the channel half-height. Δx and Δz are the streamwise and spanwise resolutions in terms of Fourier modes before de-aliasing and Δy_{max} is the coarsest wall-normal resolution. N_x, N_y, N_z are the number of collocation points in the three coordinate directions. Δt_s is the average time separation between the consecutive fields to compute coherent structures, and $T_s u_\tau/h$ is the number of global eddy-turnovers times used in the analysis, after transients are discarded. The symbols are used consistently in the figures, unless noted otherwise.

4.2 Numerical experiments and identification of coherent structures

4.2.1 Numerical experiments

The parameters of the direct numerical channel simulations used for our analysis are summarized in table 4.1, and were described in more detail in chapter 2. We define the global eddy-turnover time as h/u_τ, and occasionally use a local turnover time y/u_τ. The Kolmogorov length and time scales are $\eta = (\nu^3/\varepsilon)^{1/4}$ and $t_\eta = (\nu/\varepsilon)^{1/2}$, respectively, where $\varepsilon(y)$ is the mean dissipation rate of the kinetic energy. We often classify results in terms of buffer, logarithmic and outer regions, arbitrarily defined as $y^+ < 100$, $100\nu/u_\tau < y < 0.2h$, and $y > 0.2h$, respectively. It was checked that varying those limits within the usual range did not significantly alter the results presented below.

The Reynolds numbers chosen, $Re_\tau = 932, 2009$ and 4164, yield scale separations of $h/10\eta \simeq 30, 60$ and 100, respectively, if we assume that the largest structures are $O(h)$, and that the smallest ones are vortices with diameters of order 10η (Jiménez *et al.*, 1993; Jiménez & Wray, 1998). The microscale Reynolds numbers in table 4.1 are computed, assuming isotropy, as $Re_\lambda = q^2\sqrt{5/(3\nu\varepsilon)}$, where $q^2 = u^2 + v^2 + w^2$, and the maximum is achieved in all cases near $y/h = 0.4$. All the statistics are compiled over at least 10 global eddy-turnovers, which will be seen in §4.5.1 to be long enough with respect to the lifetimes of most coherent structures in order not to interference with their description.

The analysis of the temporal evolution of the flow requires storing approximately 10^4 snapshots for each simulation, implying several hundred Tbytes for each channel in table 4.1. To keep the storage requirements under some control, the channel dimensions are kept $L_x = 2\pi h$ and $L_z = \pi h$. It was shown by Flores & Jiménez (2010*a*) that this box size is the minimum needed to accommodate the widest flow structures, and it was shown in chapter 2 that it results in correct one-point statistics. Structures longer than $2\pi h$ exist in larger channels (Jiménez, 1998; Kim & Adrian, 1999; Marusic, 2001; del Álamo *et al.*, 2004; Jiménez *et al.*, 2004; Guala *et al.*, 2006), and are represented in the numerics as infinitely long, but it was argued by del Álamo *et al.* (2004) and in chapter 2 that their evolution times are slow enough for their interactions with the smaller scales to be represented correctly even in that case. The result is essentially healthy turbulence across the whole channel, although the behavior of the largest structures is probably unreliable. However, spectral analysis shows that structures longer than $2\pi h$ are at least as tall as h (Hoyas & Jiménez, 2006; Jiménez, 2012), so that the results of our analysis should be correct for eddies approximately restricted to the logarithmic and buffer layers. In fact, no structure has been discarded from our analysis for being too large. The number of eddies constricted by the box size is too small to influence the statistics, and the only obvious difference between our results and those in larger boxes is the 'cap' of very tall and long structures found in the size distributions in figure 3.6 in chapter 3, which is much weaker in the equivalent distributions in figures 4.8(*c*,*d*) of the present chapter.

4.2.2 Identification of coherent structures

We understand by coherent structures those motions that are organized in space and persistent in time and, although some distinctions are made in the literature, we will use as synonymous coherent structures, objects and eddies.

We define structures as simply connected sets of points in which some property exceeds a given threshold, with connectivity defined in terms of the six orthogonal neighbors in the Cartesian mesh of the DNS. We study two types of structures: the vortex clusters discussed by del Álamo *et al.* (2006) as surrogates for strong dissipation, and the 'quadrant' structures described in chapter 3 and responsible for the momentum transfer. Both have been shown to form well-defined hierarchies in the logarithmic layer of channels, and it will be shown in §4.5.1 that they retain their individuality long enough to be considered coherent.

Summarizing the identification method and results from chapter 3, vortex clusters are defined in terms of the discriminant of the velocity gradient tensor, satisfying

$$D(\boldsymbol{x}) > \alpha_t D'(y), \tag{4.1}$$

where D is the discriminant, $D'(y)$ is its standard deviation, and $\alpha_t = 0.02$ is a threshold obtained from a percolation analysis (Moisy & Jiménez, 2004; del Álamo *et al.*, 2006).

Quadrant events (Qs) are structures of particularly strong tangential Reynolds stress that generalize to three dimensions the one-dimensional quadrant analysis of Lu & Willmarth (1973). They satisfy

$$|u(\boldsymbol{x})v(\boldsymbol{x})| > H u'(y)v'(y), \tag{4.2}$$

where $-u(\boldsymbol{x})v(\boldsymbol{x})$ is the instantaneous point-wise tangential Reynolds stress, and the hyperbolic-hole size, $H = 1.75$, is also obtained from a percolation analysis (see chapter 3 or Lozano-Durán *et al.*, 2012).

Each object is circumscribed within a box aligned to the Cartesian axes, whose streamwise and spanwise sizes are denoted by Δ_x and Δ_z. The minimum and maximum distances of each object to the closest wall are y_{min} and y_{max}, and its wall-normal size is $\Delta_y = y_{max} - y_{min}$. Both types of structures are classified as being detached from the wall if $y^+_{min} > 20$, or attached to it if $y^+_{min} < 20$ (del Álamo *et al.*, 2006; Lozano-Durán *et al.*, 2012). Attached objects with $y^+_{max} > 100$ extend into the logarithmic layer and are denoted as tall attached. They form self-similar families with approximately constant geometric aspect ratios across the logarithmic layer, although without a clearly defined shape (Jiménez, 2012). Detached objects have sizes that range from a few Kolmogorov lengths up to the integral scale. The largest ones differ little from the tall attached objects (Jiménez, 2013), and we will see later that they often become temporarily attached to the wall during their lives. However, most of them are small and roughly isotropically oriented, with typical sizes of the order of 15–20η in the three directions (del Álamo *et al.*, 2006; Lozano-Durán *et al.*, 2012), and correspond to individual Kolmogorov-scale vortices.

The fraction of volume contained within vortex clusters depends strongly on the threshold chosen, but is about 1% of the total channel for the one used here, decreasing slowly with increasing Re_τ. Within this volume, clusters account for about 10–15% of the total enstrophy, which is similar to the values found by Moisy & Jiménez (2004) in isotropic turbulence. Tall attached clusters are especially relevant because, even if we will see in §4.4 that they are a relatively small fraction of the total, both by number and by volume, their bounding boxes fill a substantial part of the channel ($\approx 20\%$ by volume), and intercept a corresponding large part of the Reynolds stresses (del Álamo *et al.*, 2006).

Structure	Sizes	Shape	Fractal dimension	Volume of the channel occupied	f_c
Vortex cluster	$\Delta_x \approx 3\Delta_y$ $\Delta_z \approx 1.5\Delta_y$	sponges of worms	1.7	1%	10-15%
Attached Q$^-$s	$\Delta_x \approx 3\Delta_y$ $\Delta_z \approx \Delta_y$	sponges of flakes	2.0	6%	60%

Table 4.2: Summary of the main features of tall attached vortex clusters and Q$^-$s. f_c is the fractional contribution to the enstrophy for vortex clusters or to the Reynolds stress for Q$^-$s. The fractal dimension is defined as in chapter 3. See text for details.

They have $\Delta_x \approx 3\Delta_y$ and $\Delta_z \approx 1.5\Delta_y$, and are 'sponges of worms' whose elementary vortices have diameters of the order of 7η. Figure 4.1(a) shows all the vortex clusters in a snapshot from case M4200, and figure 4.2(a) is a particular tall attached cluster extracted from it.

Individual Qs are classified as belonging to different quadrants according to the signs of their mean streamwise and wall-normal velocity fluctuations, computed as

$$u_m = \frac{\int_\Omega u(\boldsymbol{x})\,\mathrm{d}^3\boldsymbol{x}}{\int_\Omega \mathrm{d}^3\boldsymbol{x}}, \tag{4.3}$$

over the domain Ω of all their constituent points, where $u(\boldsymbol{x})$ is the instantaneous streamwise fluctuation velocity. A similar definition is used for v_m, $\tau_m = (uv)_m$, etc. As in vortex clusters, Qs of each kind separate into wall-detached and wall-attached families. The wall-attached Q$^-$s (those with $(uv)_m < 0$) are larger and carry most of the mean tangential Reynolds stress. They only fill 6% of the volume of the channel, but are responsible for roughly 60% of the total Reynolds stresses at all wall distances. Most wall-attached events are sweeps (Q4s, with $u_m > 0$ and $v_m < 0$) or ejections (Q2s, with $u_m < 0$ and $v_m > 0$), and form self-similar families with aspect ratios $\Delta_x \approx 3\Delta_y$ and $\Delta_z \approx \Delta_y$. They agree well with the dimensions of the uv cospectrum (Jiménez & Hoyas, 2008; Lozano-Durán *et al.*, 2012). Geometrically, they are 'sponges of flakes' whose individual thickness are of the order of 12η. There are very few tall attached 'countergradient' Q$^+$s, with $(uv)_m > 0$, and we will pay little attention to them. Basically, the Reynolds stress carried by the detached Q$^+$s is compensated by the detached Q$^-$s. Figure 4.1(b) shows all the sweeps and ejections in a snapshot from case M4200, and figure 4.2(b) shows a structure extracted from it.

Table 4.2 summarizes some of the results described above for tall attached structures.

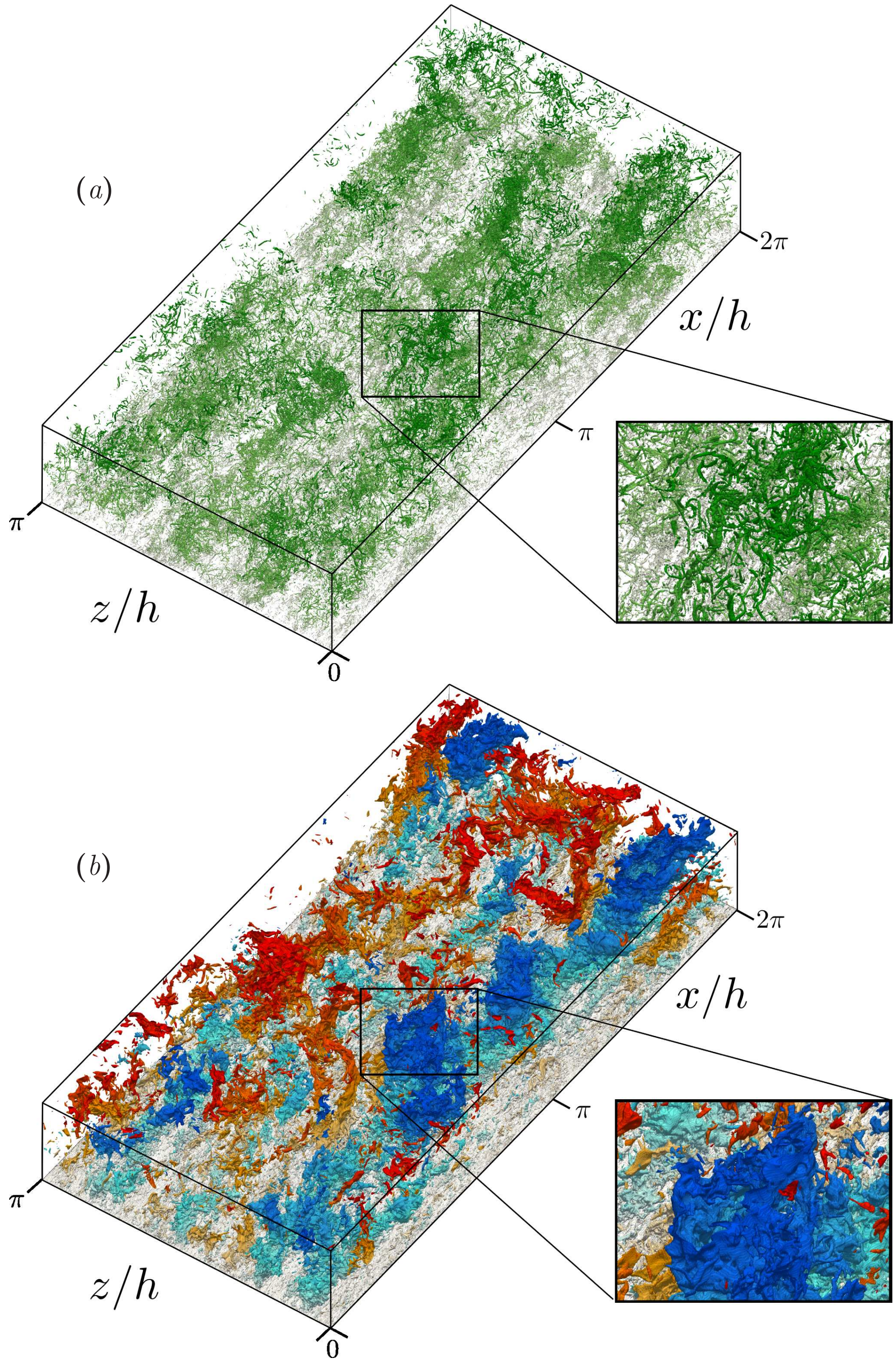

Figure 4.1: Coherent structures identified in a snapshot from case M4200. The structures are colored with their distance from the wall, and only the bottom half of the channel is shown. Points close to the wall are lighter. (*a*) Vortex clusters. (*b*) Sweeps (hot colors) and ejections (cold).

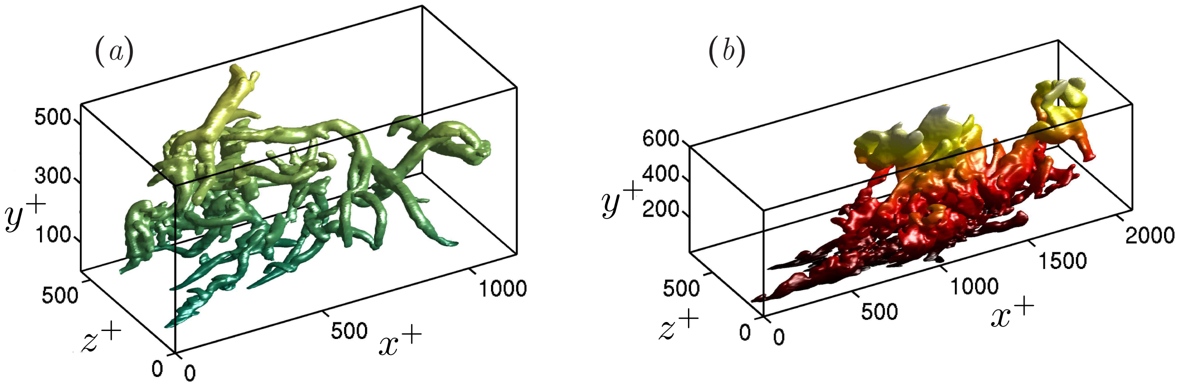

Figure 4.2: Instantaneous structures identified from case M4200. Both of them are attached to the wall and colored with their distance to it. (*a*) Vortex cluster. (*b*) Sweep.

Sweeps, ejections and vortex clusters are complex objects that are generally difficult to appreciate from a single two-dimensional view. An interactive three-dimensional view of a composite object incorporating the three kinds of structures can be downloaded from the supplementary material of Lozano-Durán *et al.* (2012), and a few more examples of individual structures can be found in our web page `http://torroja.dmt.upm.es/3Deddies`.

4.3 Tracking method

4.3.1 Temporal sampling

Since the purpose of this chapter is to analyze the time evolution of individual structures, snapshots of each simulation are periodically stored every Δt_s. The sampling intervals for the different cases are given in table 4.1, and were chosen to be sufficiently short to be able to track structures between consecutive snapshots. The sampling intervals in table 4.1 increase with Re_τ, but are always shorter than the Kolmogorov time scale, which ranges from $t_\eta^+ \approx 4$ at $y^+ = 50$ to approximately $Re_\tau^{1/2}$ in the center of the channels. The effect of coarsening the sampling times is analyzed in section 4.B, but it will be shown below that the values in table 4.1 are short enough that only the smallest structures fail to be correctly tracked. To keep the storage requirements reasonable, only M950 was stored in full for all the snapshots, so that the structure identification could be repeated if needed. This dataset was used to tune the identification and tracking methods, and the snapshots for the other two cases only contain lists of points belonging to identified structures, although including several thresholds to study the effect of the

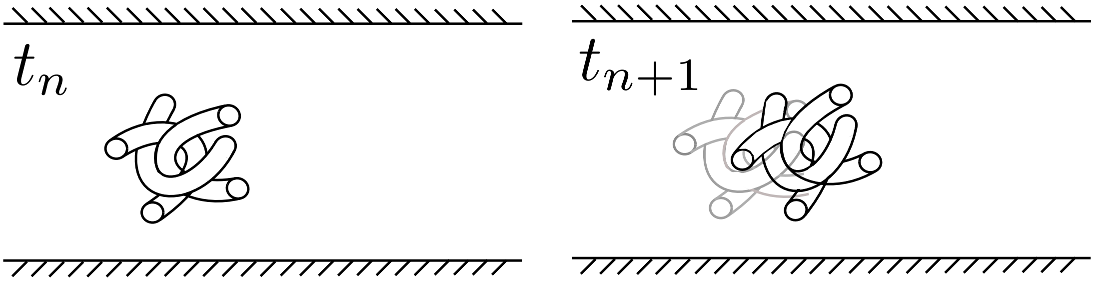

Figure 4.3: Sketch of the same coherent structure at two consecutive times. The picture corresponds to x–y views of the channel and the flow goes from left to right. The Sketch on the left shows one structure at time t_n, and the picture on the right the same structure in dark gray at time t_{n+1}, and in light gray at time t_n. The two structures overlap when copied onto a common grid and, thereby, a connection is created between them.

structure intensity. In addition, about 150 complete flow fields are stored for the two higher-Reynolds-number cases, and are used to compute averages conditioned to the different structures. This procedure decreases the storage requirement by about 95%, and makes the analysis in this chapter possible.

Note that what is being studied here are naturally occurring structures in a fully turbulent flow, rather than tripped structures in transitional or otherwise simplified flow fields (Zhou *et al.*, 1999; Wu & Moin, 2010). In that sense, our results avoid some of the artifacts of simpler situations and, for example, include all the interactions between different structures in their natural turbulent setting.

4.3.2 Steps of the tracking method

The tracking involves three stages:

(A) *Connections between structures.* All the structures of a given type (i.e., either Qs or clusters) from two consecutive snapshots are copied onto a common grid, and the spatial overlaps between them are computed using the actual points of the structures. All the structures with some overlap are considered connected (figure 4.3), and the operation is repeated for all the consecutive time pairs.

(B) *Organization in graphs.* The result of the previous analysis is a set of backwards and forward connections between structures in consecutive frames, and needs to be processed further if the evolution of individual structures is to be studied for longer times. An object in a given frame is considered to have evolved without merging or splitting if it has exactly one backward and one forward connection.

As long as that remains true, such an object can be unambiguously identified as an individual eddy. Structures with more that one backward connection are interpreted as having merged from several pre-existing ones, and those with several forward connections are said to split (see figure 4.4*a*). A first analysis of the data shows that mergers and splits happen often enough that they cannot be ignored, and suggests the organization of the objects in a temporal graph containing all the structures in the dataset and their connections. Hence, all the connected structures are organized into a very large graph or super-graph in which the nodes are the instantaneous structures and the edges are their temporal connections (figure 4.4*b*). This super-graph is then partitioned into singly connected components, each of which contains the evolution of all the structures that interact with each other at some point in their lives. For simplicity, each of those individual connected sub-graphs will be simply referred to as a 'graph'. Note that the organization of the structures into connected temporal graphs can be seen as a single clustering process in space-time, in which two points are assigned to the same four-dimensional cluster if they are contiguous in any of the three orthogonal spatial directions or in the forward or backwards temporal ones.

(C) *Organization in branches.* Graphs are organized into 'branches', each of which represents an individual structure. For that, each temporal connection is given a weight $\Delta V/V_i$, where ΔV is the volume difference between the structures in its two end nodes, and V_i is the volume of their overlap. Special action is only required for mergers and splits, which are defined as nodes with more than two edges. In those with more that one incoming edge, the edge with the lowest weight is defined as the primary incoming branch, while all the others are considered parts of branches that end (merge) at that moment. Similarly, in nodes with more than one outgoing edge, the edge with the lowest weight is defined as the primary outgoing branch, and all the others give rise to newly created branches that split at that moment. Roughly speaking, this algorithm continues as a primary branch the objects whose volume changes less across the split or merger.

A simple graph with three branches is sketched in figure 4.4(*b*), while figure 4.5(*a*) is an actual example of the temporal evolution of several vortex clusters belonging to the same graph. Figure 4.5(*b*) is the graph associated with that evolution, chosen as an example of the complex interactions that may arise. Figure 4.5(*c*) shows an actual branch classified as primary, tall attached and Q2 (see below and §4.4). Table 4.3 shows the

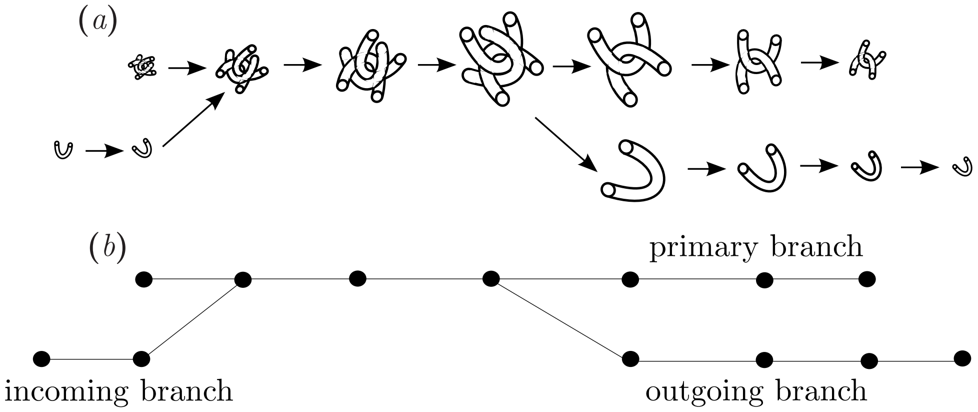

Figure 4.4: (*a*) Sketch of two structures created from the turbulent background that merge into a single one and eventually split into two fragments. (*b*) Graph associated with the evolution shown in (*a*) and its organization in branches. The graph is formed by three branches. The primary branch is continued throughout the largest object and new secondary branches are created for the fragments split and merged.

	Clusters				Qs			
Case	Objs.	Branches	Primaries	Graphs	Objs.	Branches	Primaries	Graphs
M950	185.7	6.6	2.8	1.9	107.8	3.2	1.3	1.8
M2000	397.8	19.4	8.8	6.2	294.7	18.6	11.0	9.4
M4200	799.2	45.8	19.7	36.9	889.5	64.1	35.3	32.6

Table 4.3: Number of identified objects (Objs.), branches, primary branches, and graphs. All numbers are in millions.

number of identified structures, branches and graphs for Qs and vortex clusters. Note that the numbers are in millions.

The tracking procedure in step (A) does not always succeed, especially for very small structures. The main reason is that a structure may be advected between snapshots by a distance larger than its length. To partly compensate for advection, which is mostly due to the mean flow (Taylor, 1938; Kim & Hussain, 1993; Krogstad *et al.*, 1998; Jiménez, 2013), the structures at time t_{n+1} are shifted (and hence deformed) by $-U(y)\Delta t_s$ in the streamwise direction before their connections are computed during the tracking. Even if this procedure allows us to track smaller structures than would be possible otherwise, only those with lifetimes longer than Δt_s can be captured, and structures much smaller than $U(y)\Delta t_s$ may be occasionally lost. For that reason, objects with sizes of the order of a few wall units may look artificially isolated in time from the point of view of our method.

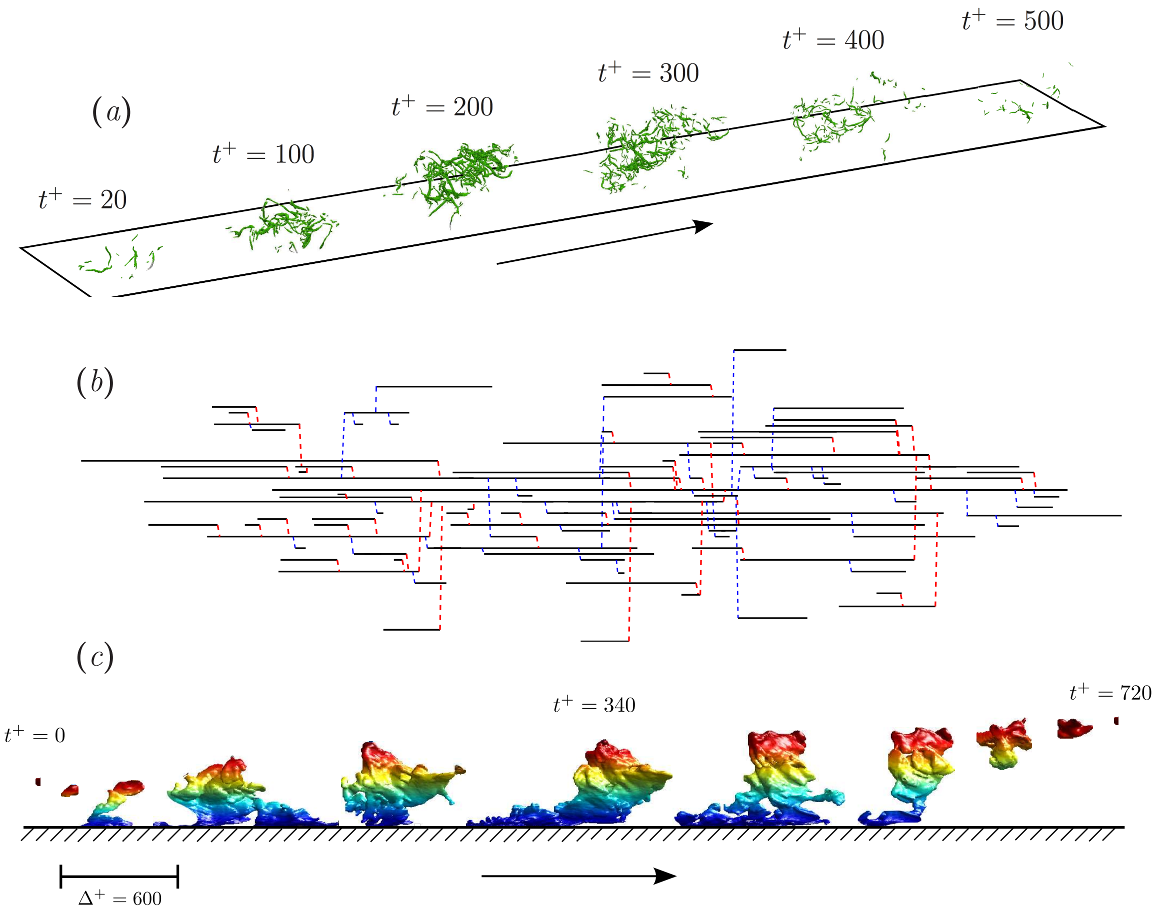

Figure 4.5: (*a*) Example of the temporal evolution of several vortex clusters belonging to the same graph for case M4200. The time goes from left to right. (*b*) The associated graph. The horizontal solid lines are branches, and the vertical dashed ones, mergers (red) or splits (blue). (*c*) Example of a primary branch extracted from case M4200 and classified as a tall attached ejection. The flow (and time) goes from left to right and the streamwise displacement of the structure has been shortened in order to fit several stages of its lifetime in less space. The structure is colored with the distance from the wall. Note the different behaviors of its upper and near-wall components.

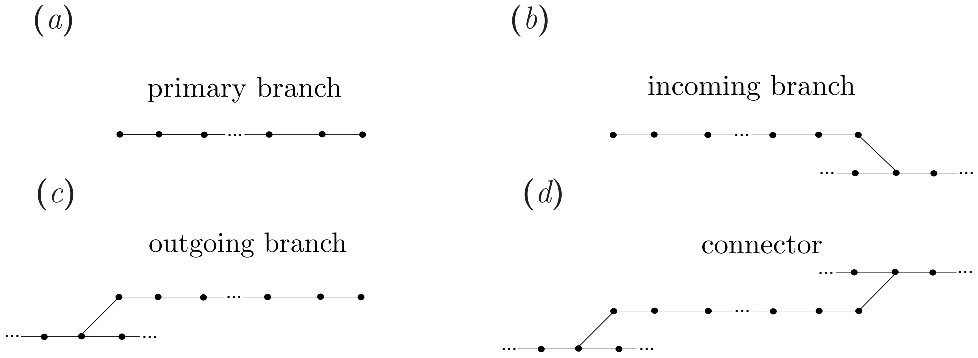

Figure 4.6: Classification of the branches attending to their beginning and end. (*a*) Primary. (*b*) Incoming. (*c*) Outgoing. (*d*) Connectors.

Section 4.A presents more details and several validation tests for the tracking procedure, including for the shifting step just described, but some idea of how many connections are being missed can be gained from the number of structures that remain isolated after the tracking step, without any temporal connection. They typically represent less than 1% of the total number of structures, and are small objects. In the case of clusters, where we have seen that the statistics are dominated by the small-scale end of the size distribution, the average volume of the isolated structures is 10–20% of the average volume computed for all the clusters. In the case of the Qs, the volume of the isolated objects is even smaller, about 1% of the average.

4.3.3 Classification of branches according to their endpoints

Branches can be further classified according to how they are created and destroyed. Sketches for the different cases are depicted in figures 4.6(*a*–*d*). When a branch is born from the turbulent background (i.e., its first node has no backwards connections) and ends in the same way (its last node has no forward connections), it is classified as 'primary' (figure 4.6*a*). Secondary branches may be 'incoming', if they are born from scratch and end in a merger (figure 4.6*b*), 'outgoing' if they are born from a split and end into the background (figure 4.6*c*), and 'connectors' if they go from a split to a merger (figure 4.6*d*). Primary branches can be considered to represent the full lives of individual structures, and will be our main interest in the following analysis. Their number for the different cases have been incorporated into table 4.3. For Qs in M4200, primaries represent 52% of all branches, incoming branches represent 20%, outgoing ones, 27%, and connectors, 1%. For the vortex clusters, primaries are 43%, incomings are 16%, outgoings are 39% and connectors are 2%. The results for M950 and M2000 are qualitatively similar. Note that the unbalance between the number of incoming and outgoing branches can be interpreted as a measure of the predominance of the direct cascade towards smaller structures over the inverse one towards larger ones. This point will be addressed in more detail in chapter 5.

4.4 Classification and geometry of branches

Graphs and branches can be classified in much the same way as instantaneous structures. For example, we saw in §4.2.2 that the structures that are attached to the wall and tall enough to reach the logarithmic layer play an important role in the dynamics of the flow. Branches are intended to represent the temporal evolution of individual structures but, since eddies cannot be expected to remain attached or detached during their whole evolution, we will classify a branch as attached if its structure is attached to the wall at some point in its life. Similarly, a branch is classified as tall attached if it contains at least a tall attached structure ($y^+_{max} \geq 100$); detached branches are never attached to the wall; and buffer-layer ones spend all their lives within the buffer layer ($y^+_{max} < 100$). The same nomenclature applies to graphs, even if each graph represents the evolution of a more complex group of related structures.

Branches of Qs are assigned quadrants in the same way as individual structures. It was shown in chapter 3 that all the points within a given Q belong to the same quadrant, essentially because moving from one quadrant to another involves a discontinuous change in the velocity fluctuations that is unlikely to occur between neighboring points in a spatially well-resolved flow field. In the same way, a discontinuous change in the quadrant of a structure is unlikely to happen in a temporally resolved simulation, and branches and graphs retain their quadrant classification over their evolution. In fact, no discontinuous change of quadrant was found in any of the branches of our data base, even if no effort was made in the tracking step to connect Qs with structures of the same quadrant.

To continue our study of branches we define their geometrical properties as temporal averages over their constituent structures. Thus, the length l_x of a branch is taken to be the temporal average over the branch lifetime, $\langle \Delta_x \rangle_B$, of the length of the single structure it tracks, and the same is true of its height l_y, and width l_z. A similar definition is used for the volume V_b of a branch, which is the temporal mean of the volume of its constituent structure, and the height of its center of gravity, which is the temporal mean, y_c, of the instantaneous centers, $Y_c = (y_{min} + y_{max})/2$.

	By number				By volume			
	Q2	Q4	Q^+	Clusters	Q2	Q4	Q^+	Clusters
buffer layer	**0.167**	**0.161**	**0.177**	**0.509**	0.023	0.026	0.055	**0.323**
detached	**0.169**	**0.148**	**0.175**	**0.471**	0.034	0.050	0.053	**0.490**
tall attached	0.002	0.001	0.000	0.021	**0.476**	**0.284**	0.016	0.188

Table 4.4: Fractional contribution of different types of branches, expressed both by number and by volume. All the entries for clusters and for Qs sum to unity independently. The most important contributions are highlighted in bold. Case M4200.

Table 4.4 summarizes the fractional contribution of each kind of branch with respect to all the branches of its same type (i.e., Qs or clusters), expressed both in terms of number of branches and of total volume. It is seen that most branches are small, either detached or confined to the buffer layer, which is also true for individual structures (del Álamo *et al.*, 2006; Lozano-Durán *et al.*, 2012). On the other hand, the distribution of the volumes is different for clusters than for Qs. While 76% of the volume of the Q-branches is concentrated in tall attached sweeps and ejections, even if they represent less than 1% of the total number, 81% of the volume of clusters is in relatively small detached or buffer-layer branches. This distribution is consistent with the different spectra of the two quantities. While the small-scale vorticity is dominated by Kolmogorov-scale vortices, momentum transfer is associated with large-scale features of the order of the integral scale. Although compiled for a single Reynolds number, table 4.4 is representative of the results for our three cases.

Average values taken over branches are relatively good representations of the instantaneous structures. We will see below that the lifetime of a structure is roughly proportional to its size, so that the most abundant small Qs and vortex clusters also have relatively short lives. They emerge momentarily above the thresholding intensity, and their properties change little before they disappear again. This is shown in figure 4.7 by the probability density functions of the heights of the individual structures in a primary branch, normalized by the mean branch height. Both for Qs and for clusters, the p.d.f.s for detached or buffer-layer branches are concentrated around unity, and only those of the larger tall attached branches show a wider spread. The easiest interpretation is that even large branches are necessarily created and destroyed as small structures, and that their longer lives gives them the opportunity of scanning a wider range of sizes. There is relatively little skewness of the distributions towards smaller or larger sizes, suggesting a relatively

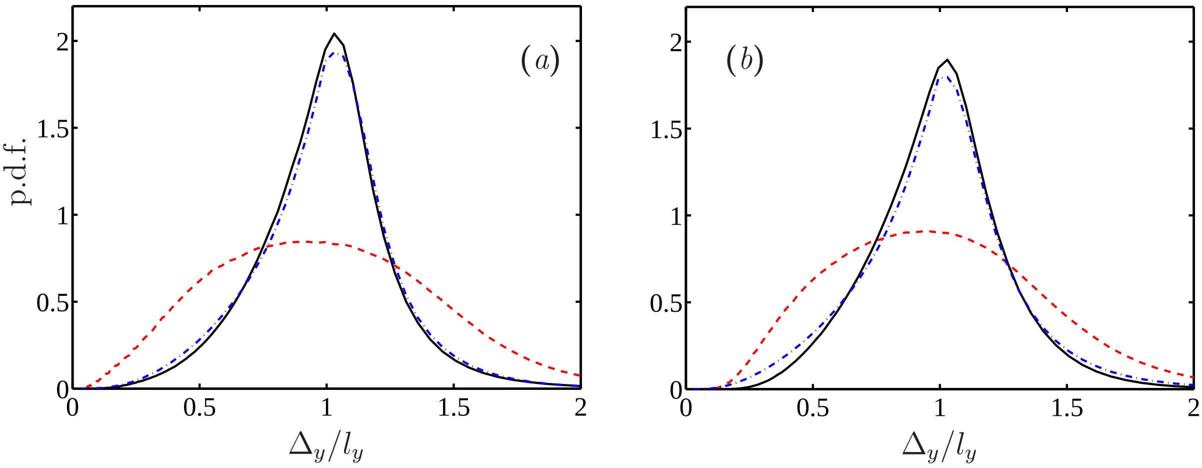

Figure 4.7: (*a*) P.d.f. of the height of the structures in primary branches, Δ_y, normalized with the mean height of their branch, l_y. ——, Detached; -·-·-, buffer-layer; – – –, tall attached. Case M4200. (*a*) Q$^-$s. (*b*) Vortex clusters.

smooth size variation. This is confirmed by the temporal evolution of the p.d.f.s of the dimensions of the structures (not shown), which reveals that their lives are approximately evenly divided into a relatively uniform initial growth, an intermediate constant phase, and an equally smooth final decay.

Figures 4.8(*a*,*b*) show the joint p.d.f.s. of the spanwise size of the detached primary branches and the height of their center of gravity, y_c. As mentioned in §4.2.2, most detached structures are small objects of the order of the Kolmogorov scale, and it is significant that the average size of the branches follows the same trend, $l_z \approx 15\eta$, mentioned in §4.2.2 for individual objects. This agrees with the narrow p.d.f.s for the detached branches in figure 4.7.

The joint p.d.f.s. of the sizes of the tall attached primaries are given in figures 4.8(*c*,*d*). Both the Q$^-$s and the vortex clusters follow self-similar aspect ratios

$$l_x \approx 2l_y, \quad \text{and} \quad l_z \approx l_y, \tag{4.4}$$

although the latter is not shown in the figure. The streamwise aspect ratio is somewhat lower than for individual tall structures, in which $\Delta_x \approx 3\Delta_y$ (see chapter 3). That difference is consistent with the evidence in figure 4.7 that tall branches contain many smaller structures that bias their aspect ratio towards isotropy. Since even large structures are roughly isotropic in the cross-stream plane, $\Delta_z \approx \Delta_y$ (del Álamo *et al.*, 2006; Lozano-Durán *et al.*, 2012), their spanwise aspect ratio is maintained by the branches.

Note that the self-similarity of vortex clusters is less clear-cut than for the Qs. In particular, while the maximum size of the Q$^-$ primaries scales in outer units, and keeps

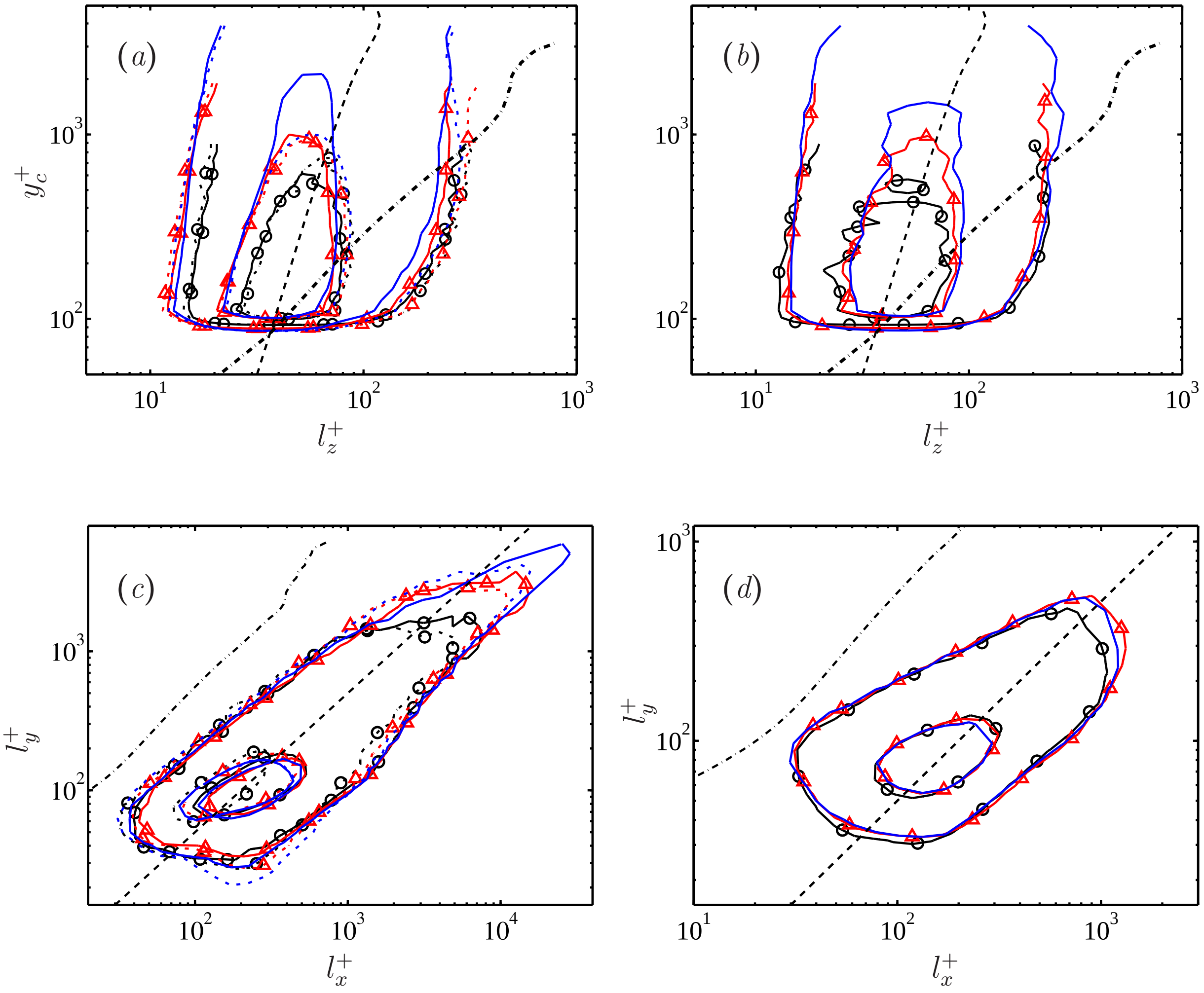

Figure 4.8: Joint p.d.f.s of the logarithm of the streamwise or spanwise average length of branches. Contours enclose 50% and 98% of the data. (*a*) Spanwise width of detached primary Q⁻s, as a function of the wall-normal distance of their center of gravity, y_c. The dashed diagonal is $l_z = 15\eta(y_c)$. ——, Ejections; – – –, sweeps. (*b*) As in (*a*), for detached vortex clusters. (*c*) Streamwise length of tall attached primary Q⁻s, as a function of their wall-normal size, l_y. The dashed diagonal is $l_x = 2l_y$. ——, Ejections; – – –, sweeps. (*d*) As in (*c*), for tall attached clusters. The dashed-dotted line in all the figures is the Corrsin scale $l_C(y) = (\varepsilon/S^3)^{1/2}$ with $y = l_y/2$ or $y = y_c$, and $S = \partial_y U$. Symbols as in table 4.1.

growing with the Reynolds number when scaled in wall units, the vortex clusters do not go beyond $l_y^+ \approx 700$. This was already noted by del Álamo *et al.* (2006) and Lozano-Durán *et al.* (2012) (and in chapter 3), who remarked that, although vortex clusters tend to be associated with Q2s, they also tend to be restricted to their near-wall roots.

In the buffer layer (not shown), most of the branches are small, with sizes of the order of the well-known quasi-streamwise vortices in that region, $l_x^+ \approx 150$ and $l_z^+ \approx 80$ (Kim *et al.*, 1987; Robinson, 1991).

The four panels of figure 4.8 include the length $l_C = (\varepsilon/S^3)^{1/2}$, where $S = \partial_y U$, which was introduced by Corrsin (1958) as the size limit below which structures should not feel the effect of shear and remain essentially isotropic. This was shown to be the case for the E_{uv} cospectrum by Saddoughi & Veeravalli (1994) in a high-Reynold-number boundary layer, and for the velocity and vorticity isotropy tensors in several shear flows by Jiménez (2013). Figure 4.8 is probably the first time that the effect is documented for individual structures. Small detached branches are approximately isotropic because they have sizes of the order of, or below the Corrsin scale, while tall attached ones are elongated in the streamwise direction because they are larger than l_C.

4.5 Temporal evolution.

4.5.1 Lifetimes

The lifetime, T, of a structure is the time elapsed between its first and last appearance in a branch, but that definition is only unambiguous for graphs or for primary branches. Secondary branches begin or end in splits or mergers, and it is unclear whether their lifetimes should be continued into the branch from where they split or into which they merge. In this section, we will mostly concern ourselves with primary branches. Figure 4.9(a) shows the relation between lifetimes and sizes of detached primary sweeps and ejections, which scale well with the Kolmogorov times at the height of their centers of gravity, $T = 5t_\eta(y_c)$. This supports the interpretation that they are essentially viscous structures with short lifetimes, although it is interesting that there is, at all heights, a tail of longer lives suggesting enhanced coherence. It was already noted by Jiménez (2013) that there is a continuous transition between large detached objects and coherent attached ones. Although figure 4.9(a) refers only to Q$^-$s, no significant differences are found between the lifetimes of detached Qs of any kind, or of vortex clusters.

Q$^-$s in the buffer layer have lifetimes of $T^+ \approx 30$ (not shown), with extreme cases in

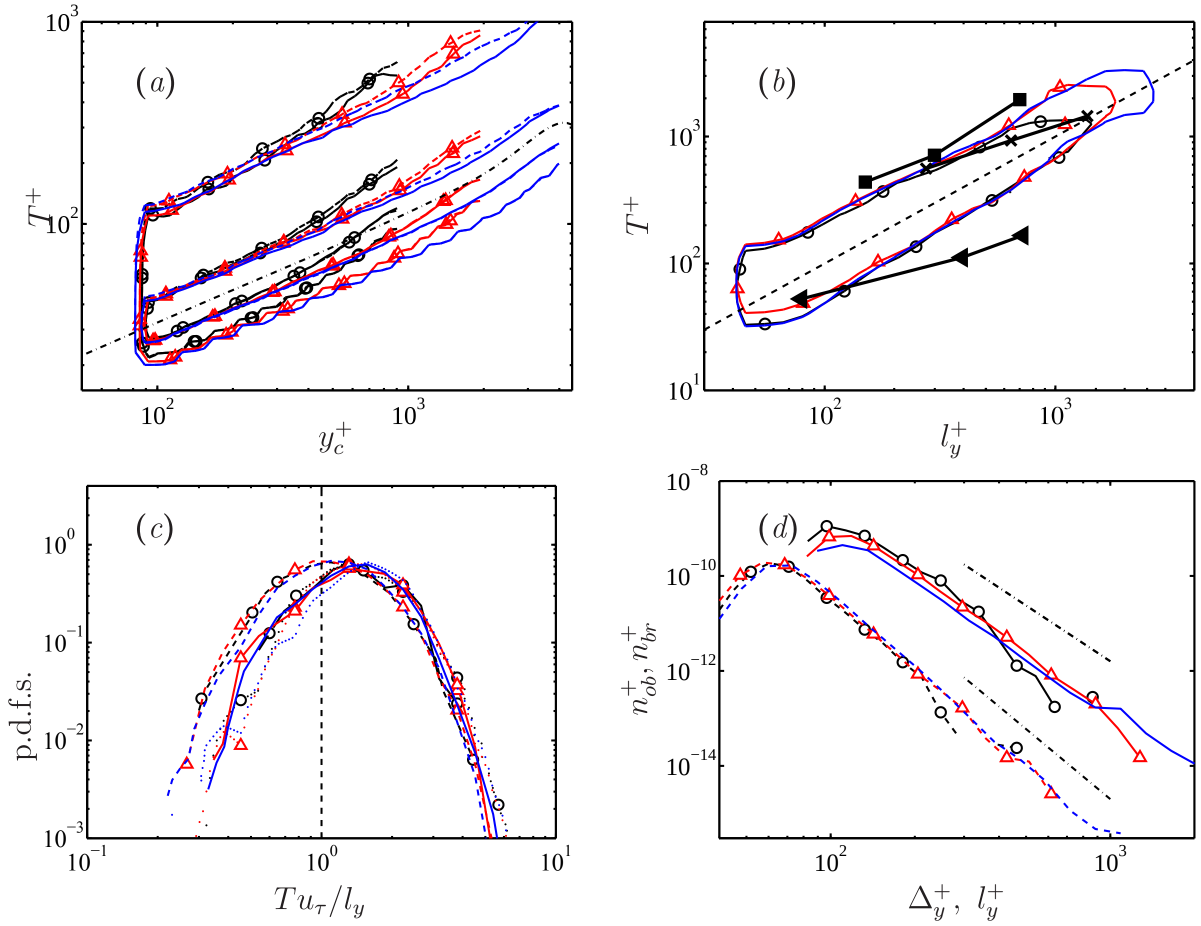

Figure 4.9: (*a*) P.d.f.s of the lifetimes of detached Q$^-$ primaries as a function of the height of their mean center of gravity, y_c. Each vertical section is a p.d.f., and contours are 50% and 98% of the maximum at each height. ———, Ejections; – – –, sweeps; –·–·–, $T = 5t_\eta(y_c)$. (*b*) P.d.f.s of the lifetimes of tall attached Q$^-$ primaries, as a function of the mean branch height, l_y. Each vertical section is a p.d.f., and contours are 50% of the maximum at each height. The dashed straight line is $T^+ = l_y^+$. ◀, Lifetimes defined by the decay of the frequency–wavenumber spectrum of v, as computed by del Álamo *et al.* (2006) for $Re_\tau = 550 - 2000$; (×,■), bursting time scale in a minimal box for the range $y/h = 0.1 - 0.3$, at $Re_\tau = 1880$. ■, From the temporal spectrum of the energy-production balance (Flores & Jiménez, 2010*a*); ×, from the temporal autocorrelation of v^2 (Jiménez, 2013). (*c*) P.d.f.s of the lifetimes of tall attached primaries, normalized with the local eddy turnover. ———, Ejections; – – –, sweeps; ········, clusters. The vertical dashed line is $Tu_\tau/l_y = 1$. (*d*) Number density per unit height, wall area and total time, of objects belonging to tall attached Q$^-$ branches as a function of Δ_y (solid), and of the branches themselves, as a function of their height l_y (dashed). The chain-dotted lines are $n_{ob} \propto \Delta_y^{-3.7}$, and $n_{br} \propto l_y^{-4.7}$. Symbols as in table 4.1.

which $T^+ \approx 400$, comparable to the bursting period of the buffer layer (Jiménez *et al.*, 2005), and to the vortex decay times in that region, $T^+ \approx 200$ (Jiménez & Moin, 1991; Jiménez & Pinelli, 1999). The lifetime distributions for buffer-layer clusters have similar tails, but many of them live very little, near the temporal resolution limit of the present simulations.

Figure 4.9(*b*) shows that the lives of the tall attached Q⁻s are proportional to the local eddy-turnover time, $Tu_\tau/l_y \approx 1$. This makes those branches self-similar not only in space, but also in time. Estimates for the lifetime of the structures have been reported before, and some of them are included in figure 4.9(*b*), for comparison. All of them refer to the temporal evolution of some flow quantity as a function of the wall distance, not to individual structures, and we have used the correspondence $y = l_y/2$. The two lines representing temporal correlations in minimal channels agree relatively well with the present estimates, which is to be expected since they were both computed from box-averaged data, which should represent the characteristics of the largest structure present in those small boxes. The best agreement is with the line marked with crosses (Jiménez, 2013), which represents the width of the temporal autocorrelation function of the box-averaged v^2, and should thus be closest to the lifetime of individual sweeps or ejections. All the points in the line fall within the levels selected for the p.d.f.s but with a lower slope. Since only three points are available for the line, it is difficult to quantified the importance of such a difference. The solid squares were obtained from the temporal spectrum of the integrated instantaneous energy balance, and are slightly longer than the present results ($3l_y/u_\tau$ versus l_y/u_τ), presumably reflecting the difference between the life of a given structure and the average period between the generation of consecutive ones (Flores & Jiménez, 2010*a*). On the other hand, the times represented by solid triangles are shorter than the present estimates. They were obtained by del Álamo *et al.* (2006) from the decorrelation time of the frequency-wavenumber spectrum of v (Wills, 1964), and thus include contributions from small scales that are bound to decay faster than the larger attached structures. It was already noted by Flores & Jiménez (2010*a*), in discussing the same data, that the definition of lifetime depends on the particular quantity being analyzed, and should only be taken as indicative. The present lifetimes are shorter than the periods reported by Elsinga & Marusic (2010) for the average orbits in the plane of Q–R invariants. These differences are not so important if we take into account that the periods of the orbits and the lifetimes presented here are computed using very different methods. In any case, the results are comparable if our structures are not expected to live for a full revolution of the orbit but just a fraction of it.

Other estimates are harder to compare. The increase of the lifetimes with the distance from the wall was noted qualitatively by LeHew *et al.* (2013), who tracked swirling structures with dimensions comparable to individual vortices in wall-parallel sections of a relatively low-Reynolds-number boundary layer ($Re_\tau = 410$). Their lifetime distributions are dominated by very short values that the authors attribute to structures moving out of the observation plane. If they are disregarded, their distributions have longer exponential tails whose decay rate imply average lifetimes that increase from $T^+ = 11$ at $y^+ = 33$ to $T^+ = 16$ at $y^+ = 200$. Even though those distributions include lifetimes up to ten times longer than their means, these values are quite shorter than ours, especially above the buffer layer. Our distributions are also far from exponential, and the conclusion by LeHew *et al.* (2013) that the lifetimes of the detached eddies are longer than those of the attached ones contradicts the present ones. However, it should be stressed that LeHew *et al.* (2013) could only distinguish attached from detached structures indirectly.

Note that, since the local mean shear in the logarithmic layer is $S(y) \approx u_\tau/\kappa y$, where κ is the von Kármán constant, the linear growth of the lifetime with the height of the structures can be interpreted as $ST \approx 5$, which is consistent with our interpretation in figure 4.8 that tall branches are controlled by their interaction with the local shear (Jiménez, 2013). If we take this to mean that the interaction with the wall is only indirect, it would suggest that sweeps and ejections should be essentially mirror images of one another. Figure 4.9(*b*) is an accumulated distribution for both types of structures, but they are separated in figure 4.9(*c*), which reveals that the long end of the two p.d.f.s is actually very similar, but that sweeps are somewhat more likely to have short lifetimes than the ejections do. It turns out that this difference is restricted to the neighborhood of the buffer layer. Figure 4.9(*d*) shows that most attached structures live near the wall, so that most of those classified as tall ($y^+_{max} > 100$) barely exceed that height. We will see below that sweeps generally approach the wall, while ejections move away from it, so that a sweep born near the top of the buffer layer tends to move near the wall and is dissipated by viscosity, while a similar ejection tends to move away from the wall and survives longer. The short-end tail of the p.d.f.s in figure 4.9(*c*) is due to this effect. When only taller branches are considered, the difference between sweeps and ejections decreases, and it essentially disappears for $l^+_y > 200$. Vortex clusters behave very similarly to ejections.

In addition to the distribution of the number of structures associated with tall attached branches, figure 4.9(*d*) also shows the distribution of the number of branches as a function of l_y. It follows from the previous discussion that, if the number of objects decays as $n_{ob} \sim \Delta_y^{-n}$, and the lifetime of a branch is $T \sim l_y$, the number of branches should decay

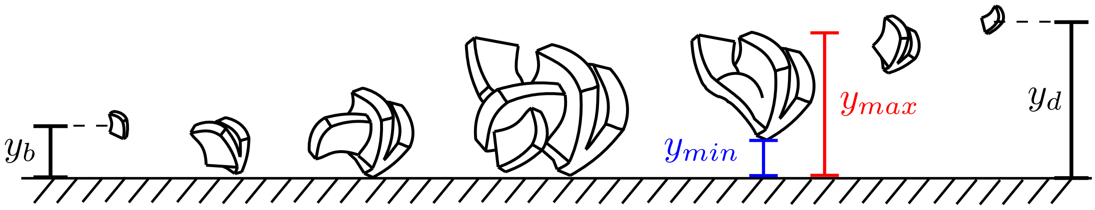

Figure 4.10: Sketch of the temporal evolution of a primary branch and the wall-normal position of its birth and death, respectively y_b and y_d, and the time-dependent maximum and minimum heights, y_{max} and y_{min}, of the instantaneous structure.

like $n_{br} \sim l_y^{-(n+1)}$, because each branch contributes T objects to n_{ob}. This estimate, which also assumes that the distribution of object sizes within a branch is described by the single parameter l_y, is tested in figure 4.9(d), and works well. That figure also shows that the number density of branches and objects is independent of the Reynolds number when expressed in consistent units.

As a final remark, the simulations presented here were run for at least $10h/u_\tau$, whereas the longest lifetime identified for the structures in the logarithmic layer is five times shorter, giving us some confidence on the statistical relevance of our results.

4.5.2 Birth and death, and vertical evolution

The distribution of branch births and deaths is interesting, even if only because there are at least two competing models for the genesis of tall attached structures. They differ mostly in their view of the importance of the wall. One view is that the buffer layer is the source of attached coherent motions, from where they rise into the outer region (Adrian *et al.*, 2000; Christensen & Adrian, 2000; Adrian, 2007; Cimarelli *et al.*, 2013). A different view, with some support from the discussion in the previous section, is that structures are controlled by the shear, and can be born at any height. In this view, the wall is mainly a source of shear, and the structures attach to it as part of the natural growth of eddies in any shear flow (Rogers & Moin, 1987). Because the shear is strongest near the wall, that is also where most structures are born and are strongest, but large structures would predominantly be expected to arise farther away (del Álamo *et al.*, 2006; Flores *et al.*, 2007; Lozano-Durán *et al.*, 2012). Figures 4.11(a,b) show the p.d.f.s of the height of the centers of primary Q^-s at the beginning and the end of their lives, classified as a function of the mean branch height (see sketch in figure 4.10). It turns out that Q2s are born in the buffer layer, and rise, while Q4s are born away from the wall, and drop. Moreover, it appears that ejections die and sweeps are born near their mean branch height, which for attached branches is essentially $l_y \approx 2y_c$.

The evolution of the maximum and minimum structure heights during the life of a branch is given in figures 4.11(*c*,*d*). As we just saw, the Q2s are born attached to, or very near, the wall. They remain attached for about 2/3 of their lives, after which they detach and rise quickly. Their maximum height grows steadily during that time. The evolution of the Q4s is the opposite. Their bottom moves down relatively quickly, attaches to the wall at roughly 1/3 of the branch live, and stays attached thereafter. Their top moves down steadily. The details of the distribution into attached and detached behavior change slightly when considering very tall branches, or those closer to the buffer layer, but the overall behavior is always just as described. Clusters behave approximately as Q2s, although, as already mentioned, their range of heights is more limited (figures 4.11*e*,*f*).

The wall-normal velocity of the individual eddies is shown in figures 4.12(*a*,*b*), defined from the vertical displacement of their center of gravity between consecutive times separated by $\Delta t^+ \approx 30$ (to avoid spatial and temporal resolution issues) during which merging or splitting is not taking place. Consistent with the previous discussion, ejections move upwards on average, and sweeps move towards the wall, and it is interesting that both move within fairly narrow ranges of wall-normal velocities close to $\pm u_\tau$. This agrees with the results in Flores & Jiménez (2010*a*), who noted that strong sweeps and ejections in a small channel move across the logarithmic layer with surprisingly constant velocities. Note that these velocities are also consistent with a total vertical excursion of order l_y (figures 4.11*a*,*b*) during a lifetime of order l_y/u_τ (figure 4.9*b*). Vortex clusters have both positive and negative vertical velocities. Apparently, although most clusters follow ejections as they rise, some of them also move with the sweeps as they drop. The shapes of the velocity distributions do not depend much on the attached or detached character of the structures being tracked, although the velocities decrease somewhat in the buffer layer, as expected (not shown).

It was speculated in Flores & Jiménez (2010*a*) that bursts and ejections are parts of a single underlying structure, because they tend to burst and ebb concurrently in channels whose dimension has been adjusted to be minimal in the logarithmic layer, and also because their symmetric vertical velocities suggest a common cause. It is also known that they tend to occur in side-by-side pairs (chapter 3) and that the conditional mean flow field of such pairs is a large-scale streamwise roller whose up- and down-welling edges contain the Q^-s, both in the buffer layer (Guezennec *et al.*, 1989) and farther from the wall (Jiménez, 2013). The symmetry of the distributions in figures 4.9(*c*) and 4.12(*a*) further supports that view.

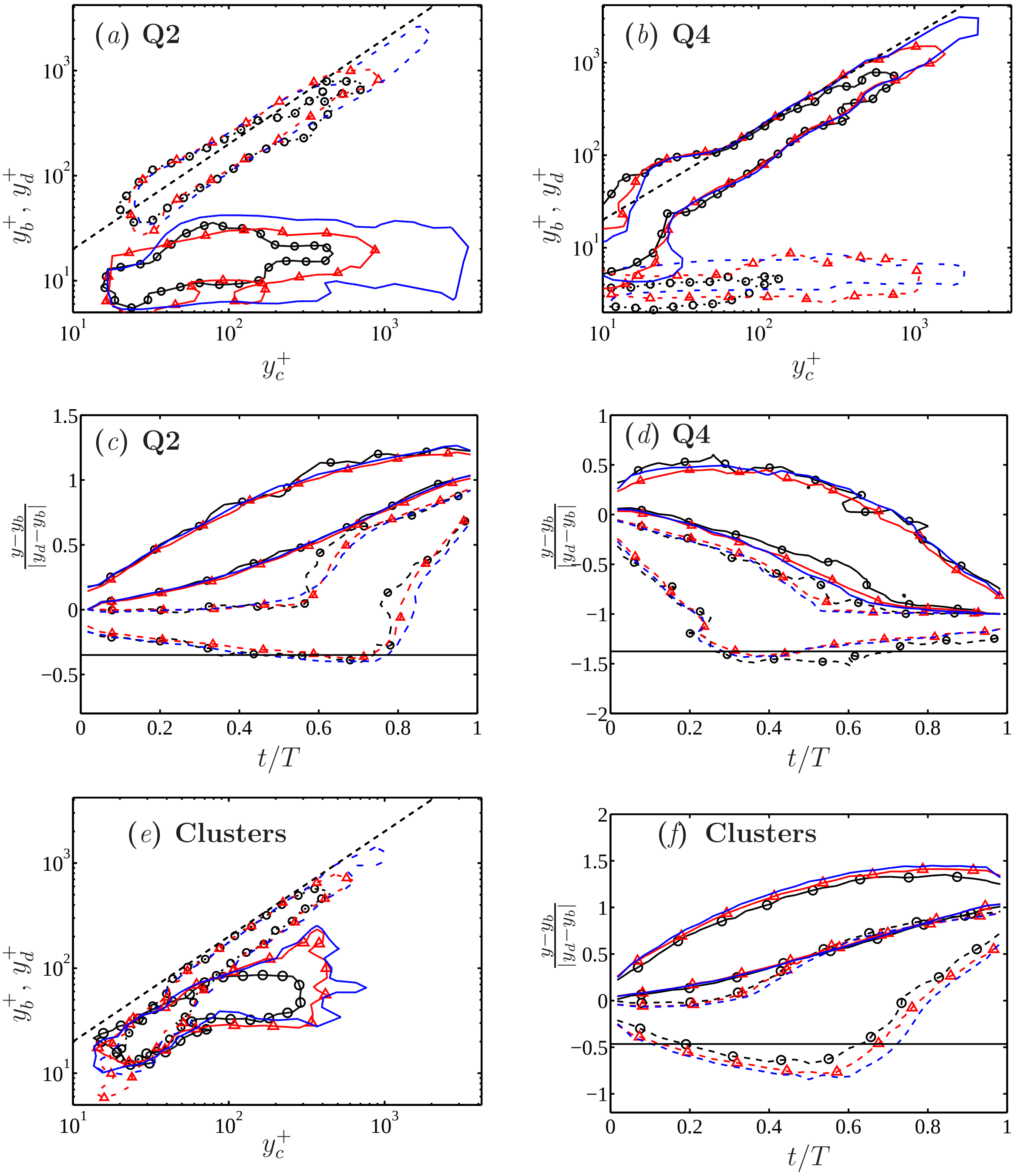

Figure 4.11: (a, b and e) P.d.f.s of the wall-normal height of births, y_b (——), and deaths, y_d (– – –) of tall attached primary branches, as a function the mean height of their center of gravity, y_c. The dashed straight line is $y_{b,d} = 2y_c$. (c, d and f) P.d.f.s of the minimum (– – –) and maximum (——) heights of tall attached primary branches, as functions of the time elapsed from their birth. Time is normalized with the lifetime of each branch, T, and y_{min} and y_{max} with the heights, y_b and y_d, at its birth and death, respectively (see figure 4.10). The solid horizontal lines are the average position of the wall. (a, c) Ejections. (b, d) Sweeps. (e, f) Vortex clusters. In all cases, each vertical section is a p.d.f., and the contours are 0.5 of its maximum. Symbols as in table 4.1.

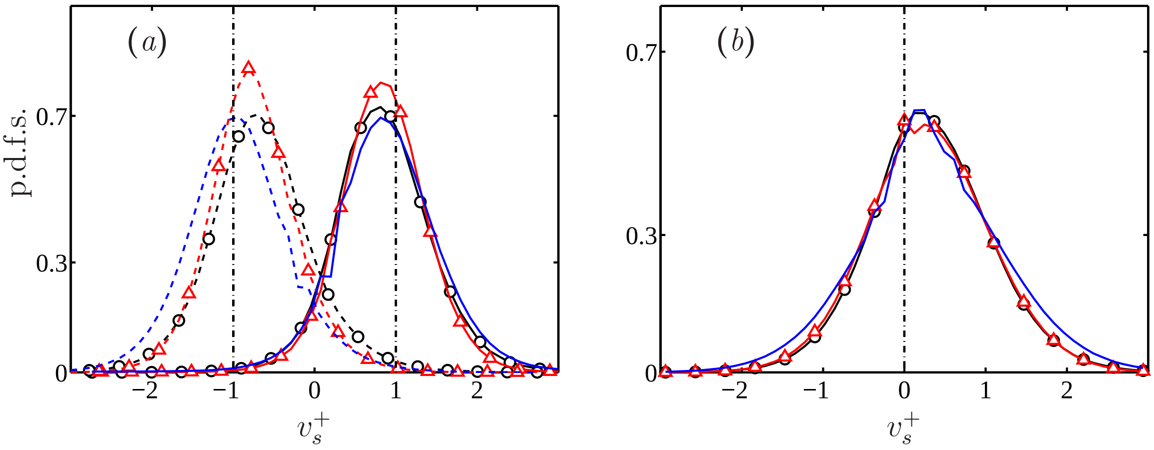

Figure 4.12: P.d.f.s of the wall-normal velocity of the center of gravity of the structures. The vertical lines are $\mathrm{d}y_c/\mathrm{d}t = \pm u_\tau$ in (a) and $\mathrm{d}y_c/\mathrm{d}t = 0$ in (b). (a) ———, Ejections; − − −, Sweeps. (b) Vortex clusters. Symbols as in table 4.1.

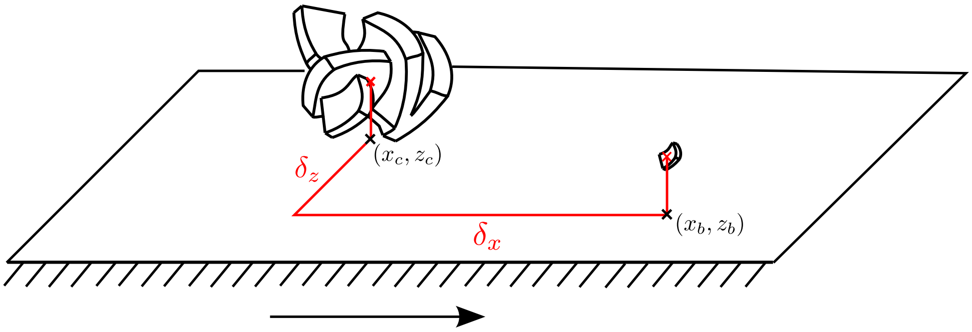

Figure 4.13: Sketch of the relative streamwise and spanwise distances of births with respect to existing tall attached structures. Points (x_c, z_c) and (x_b, z_b) are the wall-parallel coordinates of the centers of gravity of the existing and newborn structures respectively.

4.5.3 Relative position of branch creation

We next consider whether the birth of new tall attached branches is influenced by pre-existent structures in their neighborhood, such as would be the case, for example, in the vortex-packet propagation mechanism proposed by Tomkins & Adrian (2003). Note, however, that such an association would not necessarily imply causation, and could rather be due to the presence of a larger undetected common structure, as discussed above.

For that purpose, we look at the location with respect to existing structures of the birth of branches that will eventually become tall attached. At each moment, a frame of reference is defined at the center of gravity of existing tall attached structures, and the relative positions of births taking place at that moment are computed. Figure 4.13

sketches the procedure. The relative distances are defined as

$$\delta_x = \frac{x_b - x_c}{\sqrt{\Delta_x^2 + \Delta_z^2}}, \tag{4.5}$$

$$\delta_z = \frac{z_b - z_c}{\sqrt{\Delta_x^2 + \Delta_z^2}}, \tag{4.6}$$

where x_c and z_c are the coordinates of the center of the existing structure, and x_b and z_b the position of the newborn one. The distances are normalized with the length of the x–z diagonal of the circumscribed box of the existing structure, and only births between the wall and the maximum height of the existing structure are considered.

The resulting p.d.f.s are shown in figures 4.14(*a*–*d*). In all cases, the central part of the p.d.f.s has a low probability of finding births, because that region is already occupied by the existing structure. Figures 4.14(*a*,*b*) show that existing ejections trigger new ejections ahead of themselves, while existing sweeps trigger new sweeps predominantly behind. The p.d.f.s of the relative wall-normal position of births (not shown) reveal that the new ejections tend to appear in the buffer layer (consistently with figure 4.11*a*) whereas sweeps are born roughly at same height as the center of gravity of the already existing ones. Figure 4.14(*c*) displays the birth of sweeps with respect to existing ejections, and a symmetric figure can be drawn for ejections with respect to sweeps. It shows that Qs of different quadrants are not created aligned to each other, but side by side. Note that, in this case, the probability map is oriented in such a way that the closest newborn structure is always to the left ($\delta_z > 0$) of the existing one. An un-oriented p.d.f. would show new structures appearing symmetrically at both sides of the center. Note also that, for that reason, the minimum birth probability of this case is not at the center of the p.d.f. but to its right ($\delta_z < 0$). Births in that location have been transferred to the peak on the left ($\delta_z > 0$). Finally, figure 4.14(*d*) shows that vortex clusters are born downstream of existing ones, as in the case of ejections.

The p.d.f.s in figure 4.14 are self-similar plots normalized with the size of the 'parent' structure, and therefore have no absolute dimensions associated with them. If we consider them as reflecting a causal relation, they show that larger structures influence regions farther from their centers than small ones do. The p.d.f.s in figure 4.14 are highly reminiscent of the p.d.f.s of the relative location of neighboring structures in figure 3.14, including similar distances between the different peaks, suggesting that the geometric relations between existing structures reflect their process of formation. We have already mentioned that Q2s and Q4s are organized into streamwise trains of pairs each of which contains a Q2 and a Q4 side by side, which can be interpreted to mean that sweeps and

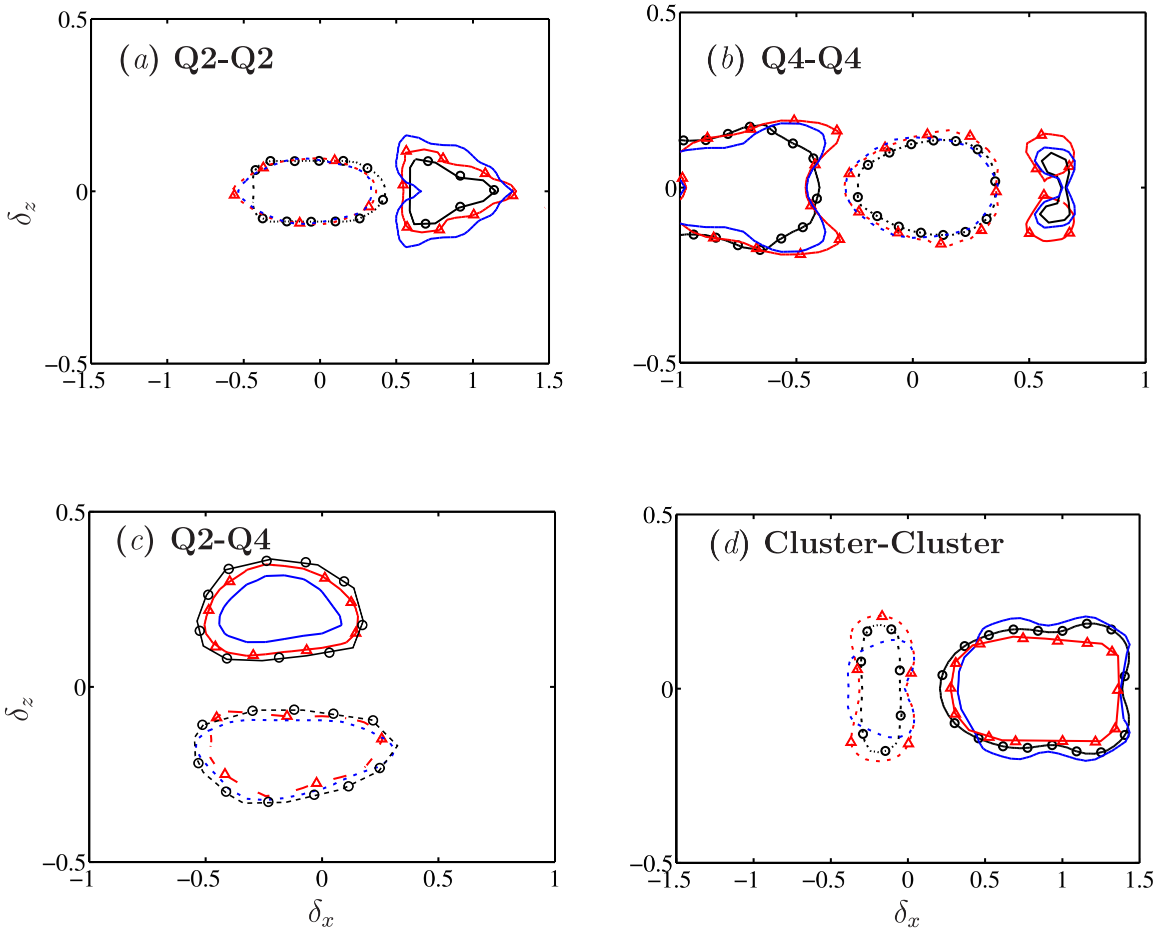

Figure 4.14: Joint p.d.f.s of the relative streamwise, δ_x, and spanwise, δ_z, distances of births with respect to existing tall attached structures whose height is $\Delta_y^+ \geq 200$ (see sketch in figure 4.13). (*a*) New ejections with respect to existing ejections. (*b*) New sweeps with respect to sweeps. (*c*) New sweeps with respect to ejections. (*d*) New vortex clusters with respect to existing clusters. Contours are 1.2 (——) and 0.8 (– – –) the probability in the far field. Symbols as in table 4.1.

ejections are reflections of quasi-streamwise large-scale rollers, embedded in the longer streaks of the streamwise velocity; sweeps in the high-velocity side of the streak, and ejections in the low-speed part. Figure 4.14(*c*) and its counterpart in chapter 3 (figure 3.14) would then reflect the spanwise separation between the high- and low-velocity component of the streaks. The streamwise separation in figures 4.14(*a*,*b*) would correspond to the streamwise wavelength of the inhomogeneity of the streak, which is known to take predominantly the form of meandering, both near the wall (Jiménez *et al.*, 2004) and in the logarithmic layer (Hutchins & Marusic, 2007*a*).

However, the front-to-back asymmetry in figures 4.14(*a*,*d*) provides additional information beyond that contained in the relative position of the instantaneous structures. It shows that trains of ejections and clusters grow streamwise by extending downstream, but that sweeps grow towards their backs. This difference is difficult to interpret, since it was shown in the previous chapter that there are very few unpaired Q^-s in the channel, and the Q4s triggered behind the pre-existing Q4 in figure 4.14(*b*) would eventually require the formation of new Q2s, and vice versa. It is not clear from figure 4.14(*a*) where those Q2s are coming from. Some possibilities suggest themselves, although they are unfortunately difficult to test statistically. The simplest one is probably that the pairs are completed by un-triggered structures. The probability contours in figure 4.14 are only 20% higher or lower than the uniform background probability of finding a newborn structure anywhere, but it is difficult to see why only one component of the organized pairs in figure 4.14(*c*), should be created randomly. A more likely possibility is that the missing trailing Q2s are created too far from the origin to show in figure 4.14(*a*). A plausible variant of that scenario starts by assuming that the triggering Q2s and Q4s are always in the form of pairs. They would also trigger new pairs, but only (or predominantly) with the opposite orientation to that of the existing one. A triggering Q2 from 4.14(*a*) with a Q4 to its right would create ahead of itself a new Q2 with a Q4 to its left, which would be too far from the existing Q4 to appear in the conditional probability distribution in 4.14(*b*). A similar scenario would account for the formation of a companion Q2 for the new Q4 in figure 4.14(*b*). Thus, a clockwise quasi-streamwise roller, with the sweep to the right of the ejection (see figure 9 in Jiménez, 2013) would only trigger anticlockwise rollers ahead or behind itself. This process would not be too different from the self-propagation of hairpin packets in Tomkins & Adrian (2003), although it should be made clear that the objects being discussed here live predominantly in the logarithmic layer, and that none of the evidence in this chapter, or in the previous one, suggests the presence of hairpins in that region. Note that the generation of rollers of alternating sign along a streak leads naturally to the observed streak meandering. It also agrees with the staggered-vortex models proposed by Schoppa & Hussain (2002) for the buffer layer, and with the majority of the equilibrium and periodic exact solutions more recently found in wall-bounded flows, and reviewed, for example, in Kawahara *et al.* (2012).

4.5.4 Advection velocities

How structures deform during their evolution, and presumably what determines their lifetime, is in part controlled by the vertical gradient of their advection velocity. It is well-known that most flow variables advect roughly with the local mean streamwise velocity (Kim & Hussain, 1993; Krogstad *et al.*, 1998), and are thus deformed by the mean shear.

The advection velocity of the wall-parallel sections of the structures is measured in two independent ways. In the first one, the set of points within the section of the structure is correlated between consecutive times separated by $\Delta t^+ \approx 10$ (to avoid grid resolution issues), and the velocity is estimated from the shift away from the origin of the maximum correlation peak (Kuglin & Hines, 1975; Sutton *et al.*, 1983). This is the method typically used in particle-image velocimetry (Willert & Gharib, 1991). The second method tracks the center of gravity of the circumscribing rectangle to the section of the structure. Both velocities need not coincide if, for example, the structure moves by accreting new elements from the front and shedding them from behind. The difference is akin to the distinction of phase and group velocity in wave packets, with the correlation method representing the phase velocity. Non-dispersive structures in which the phase and group velocities coincide can be considered as 'coherent' objects advected by the flow, while dispersive ones are probably better understood as being 'footprints' continuously destroyed and re-formed by some global influence, such as pressure.

The results are shown in figures 4.15(*a*,*b*), which displays phase velocities from snapshots not involved in mergers or splits. All structures move approximately with the mean profile, $U(y)$, above the buffer layer. Ejections move slightly slower than $U(y)$, roughly by $-1.5u_\tau$, while sweeps move faster by roughly the same amount. This agrees with previous results (Guezennec *et al.*, 1989; Krogstad *et al.*, 1998), and with the idea that ejections live in low-velocity streaks, and sweeps in high-velocity ones. Vortex clusters can be either faster or slower than $U(y)$, although the latter is slightly more probable, presumably reflecting their preferential association with ejections. This was also seen in their vertical velocities in figure 4.12(*b*). Their mean advection velocity is $U(y) - 0.8u_\tau$. Close to the wall, all structures advect roughly at $10u_\tau$, in agreement with Kim & Hussain (1993) and Krogstad *et al.* (1998). Figure 4.15(*b*) also includes the p.d.f.s of the advection velocities

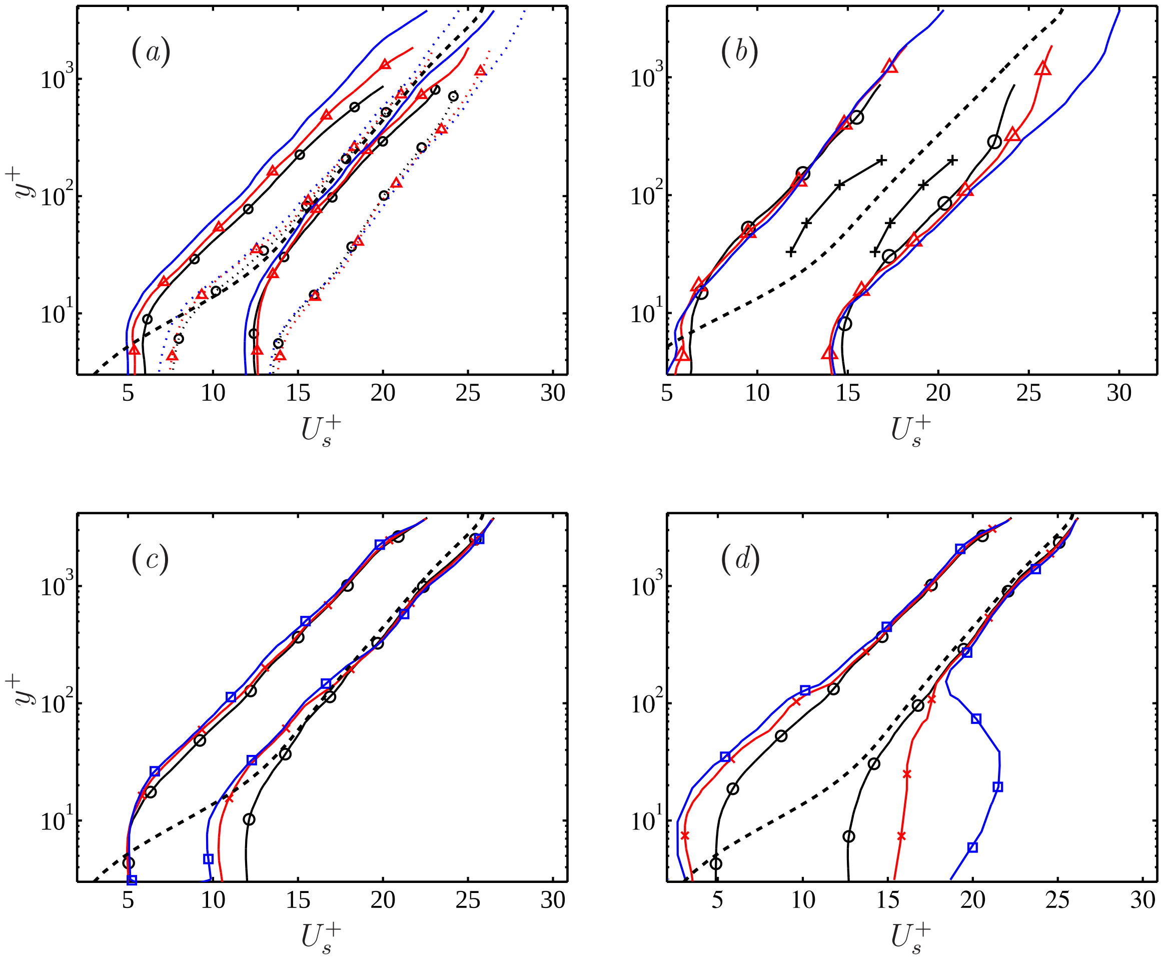

Figure 4.15: P.d.f.s of the streamwise advection velocities of wall-parallel sections of the individual structures, as functions of their wall-normal distances. (*a*) Phase velocity. ——, Q2s; – – –, Q4s. (*b*) Phase velocity. Vortex clusters. Symbols as in table 4.1. +, advection velocity of the swirling coherent structures adapted from figure 10(b) in LeHew *et al.* (2013). (*c*) Phase velocity. Q2s in M4200. ∘, all structures; ×, $\Delta_y^+ > 400$; □, $\Delta_y^+ > 1000$. (*d*) As in (*c*), but group velocity. In all panels, each horizontal section is a p.d.f., and contours are 40% of its maximum. The thicker dashed line is the mean streamwise velocity profile for case M4200.

reported by LeHew *et al.* (2013) which shows shorter tails though reasonable considering the differences between both methods. Elsinga *et al.* (2012) observed a mean advection velocity of $0.78U_\infty$ at $y = 0.2h$, with U_∞ the free steam velocity of the boundary layer, which also agrees with the value of $0.776U_c$ obtained for vortex clusters at $y = 0.2h$ in the present study, being U_c the mean channel velocity at the centerline.

On the other hand, these results are not entirely consistent with those in del Álamo & Jiménez (2009), who showed that large structures with wavelengths $\lambda_x \gtrsim 2h$ advect at all heights with the bulk velocity of the mean profile, including near the wall, where that velocity is very different from the local one. Their method computes a phase velocity, and this dependence on the wavelength suggests that, at least for large attached structures near the wall, turbulence should be dispersive. The same conclusion could be drawn from the attached-eddy model of Townsend (1976), who proposed that large structures near the wall are passive ("inactive"), controlled by active cores farther away from the wall. Bradshaw (1967) later showed that the interaction between the outer active part and the inactive inner one was most likely due to the pressure induced by the active cores. This was even more vividly shown by Tuerke & Jiménez (2013) by means of a numerical experiment in which the y-distribution of the total tangential stress in a channel was modified by a distribution of volume forces. They expressed the average stress at a given distance from the wall as a y-dependent friction velocity, $u_\tau(y)$, and showed that, while the intensity of the velocity fluctuation spectrum $k_x E_{uu}(\lambda_x, y)$, where $k_x = 2\pi/\lambda_x$, scale with $u_\tau^2(y)$ for relatively short wavelengths, $\lambda_x \approx y$, the longer wavelengths scale everywhere much better with u_τ^2 at the height of the active cores, $y = \lambda_x/10$. The suggestion in all these cases is that, while the smaller scales contained within the attached root of a large structure may move approximately with the local mean velocity, the structure itself should advect with a velocity closer to that of the active core near its center of gravity. For a graphic representation of this process, see the different behaviors of the root and body of the structure in figure 4.5(*c*). Note that this observation reinforces and refines the evidence for the modulation of the inner layer by the outer one documented by Mathis *et al.* (2009).

This is confirmed in figures 4.15(*c*,*d*), which show the advection velocity separately for structures of three different size ranges. Figure 4.15(*c*), shows the phase velocity as a function of y. All the size ranges agree, showing that the motion of the small scales traced by the correlation method is indeed independent of the size of their 'host' structure. On the other hand, the group velocities in 4.15(*d*), computed by tracking the circumscribing box, depend on the structure size. All the structures travel with the mean velocity for

$y^+ \gtrsim \Delta_y/4$, but they decouple from the mean flow below that level, and move with what can be interpreted as the advection velocity of the base of the active part of the structure. Note that, since both the shear time, $(\partial_y U)^{-1} \sim \kappa y/u_\tau$, and the local eddy-turnover time, y/u_τ, decrease as we approach the wall, such a decoupling between the top and bottom parts of the attached structures, with very different local time scales, should probably have been expected.

The conclusion that only the upper part of the tall attached structures can be considered as coherent is interesting, because the lifetime of a structure is most probably limited by its deformation by the shear. Whenever a structure is sheared by much more than its length, it should disappear as a coherent object. The difference between the phase velocities at the top and bottom of an attached structure is approximately $\Delta U \approx u_\tau \kappa^{-1} \log \Delta_y^+$, which would shear it by an amount roughly equal to its length in a time of the order of $\Delta_x/\Delta U \sim \Delta_x/(u_\tau \log \Delta_y^+)$. This estimate differs from the data in §4.5.1 by the non-trivial logarithmic denominator. On the other hand, if the only deformation that counts is that between $y = \Delta_y$ and $y = \Delta_y/4$, or some other constant factor, the shear time would be proportional to $(\Delta_x/u_\tau)\log 4$, i.e., $T \sim \Delta_x \sim \Delta_y$, which agrees better with the observations.

4.6 Conclusions

We have presented a novel approach to the study of the kinematics and dynamics of wall-bounded turbulent flows, and applied it to temporally and spatially well-resolved simulations of turbulent channels in the range of Reynolds numbers $Re_\tau = 930$–4200. The fields were stored often enough, and the simulated time was long enough, for several millions of structures to be individually tracked from birth to death. Two types of structures were analyzed, vortex clusters (del Álamo *et al.*, 2006), and the quadrant structures of the tangential Reynolds stress (chapter 3 and Lozano-Durán *et al.*, 2012), both of them presented and studied in chapter 3. Although it was found that most structures stay small and live short lives, special emphasis was put on the tall attached sweeps and ejections with longer lifetimes stretching from the wall into the logarithmic layer. In agreement with previous investigators, those structures were found to carry most of the wall-normal momentum transfer.

The tracking procedure resulted in the organization of the structures into primary branches, representing the evolution of a single structure from birth to death, and a complicated set of secondary branches that either merge into, or split from them. Primary tall attached structures were shown to be geometrically self-similar, with roughly constant aspect ratios for branches taller than $l_y^+ > 100$–200, and equally self-similar lifetimes, $T^+ \approx l_y^+$. This was true for sweeps, ejections and vortex clusters, and it is striking that branches of sweeps and ejections were found to be essentially mirror images of each other. Both have essentially identical lifetimes, and their vertical advection velocities are antisymmetric: $+u_\tau$ for the ejections, and $-u_\tau$ for the sweeps. Moreover, ejections are born near the wall and rise until they disappear near their maximum height, and sweeps are born away from the wall and move towards it. This, together with the observation by previous investigators that sweeps and ejections are typically found in side-by-side pairs, strongly suggests that both structures are manifestations of a single quasi-streamwise roller lying between them, whose height does not change much during its evolution. Vortex clusters, which are typically found between sweeps and ejections, tend to follow the ejections, and are probably partial manifestations of the roller. Tall attached sweeps and ejections are found more often in the high-shear region near the wall, but they appear often enough at all heights for the largest structures to be responsible for most of the momentum transfer. Several observations were shown to imply that the largest structures at each height are large enough to be controlled by the shear, and their antisymmetry suggests that they are not necessarily created near the wall, but are rather a general consequence of the mean shear itself. On the other hand, detached structures are much smaller than the tall attached ones and have sizes and lifetimes of the order of the local Kolmogorov scales.

It was found that new structures form predominantly ahead or behind structures of the same kind, but the details of that process were found to be difficult to reconcile with the rest of the available evidence unless sweeps and ejections were again considered part of side-by-side pairs that trigger new pairs of opposite polarity. A clockwise roller would thus follow a counterclockwise one, and vice versa. Although our study deals mostly with large structures in the logarithmic and outer layers, the resulting model of alternating vortices flanking a streak agrees qualitatively with older ones of the buffer layer, and with transitional exact structures at much lower Reynolds numbers.

The streamwise advection velocity of individual structures was measured, and found to depend on the distance to the wall, implying that the structures are deformed enough by the mean shear that their lifetime is controlled by that deformation. It was moreover found that their group and phase velocities only coincide in the top part of the tall attached structures ($y > \Delta_y/4$). This is the only part of the structure that can be considered coherent. The ‘root’ below that height is dispersive, and is probably just the ‘pressure shadow' of the upper core. We have noted that restricting coherence to the upper part of the attached structures also makes their observed lifetimes consistent with a model in which they are created and eventually destroyed by their deformation by the mean velocity profile.

The model proposed shares a few properties with the hairpin's packet paradigm (Adrian, 2007) but also shows fundamental differences that will be discussed in chapter 5.

4.A Details and validation of the tracking method

4.A.1 Spurious connections and branches

This section expands the discussion about the tracking method detailed in section 4.3. For all the results presented, those branches in which none of the structures attain a volume higher than 20^3 wall units are excluded to avoid grid resolution issues. Besides, branches crossing the edges of the temporal domain are also dismissed since their histories are incomplete.

In order to remove spurious connections, four particular cases are corrected (see figure 4.16). Sometimes the branches do not clearly split or merge but they rather touch each other as shown in figures 4.16(*a*,*b*). In these cases, the connection between both branches is dismissed when the difference of volume between the structures labeled as (1) and (2) is less than 5% (figure 4.16*a*). On the other hand, the structures (1) and (2) are disconnected when such difference is larger than 90% (figure 4.16*b*). The same corrections are applied to the cases obtained reversing the time in figures 4.16(*a*,*b*). The third case is sketched in figure 4.16(*c*). When the beginning and the end of a branch belong to the same branch, it is considered that both represent the evolution of a single coherent structure and, hence, are gathered together as a single branch. The last correction is done when two branches are connected with the same node of a third branch as shown in figure 4.16(*d*). In this case, the first two branches are disconnected from the third one and reconnected together to form a single branch. The modification is applied only when the difference of volumes as well as the difference of the y–z centers of gravity of (1) and (2) are less than 10%. All the percentages given above are computed with respect to the largest magnitude involved.

Finally, we address the effect of the spatial shifting of the structures employed in the tracking step. As discussed in section 4.3, in order to maximize the connections between structures at contiguous times, t_n and t_{n+1}, the points of the objects at time t_{n+1} are

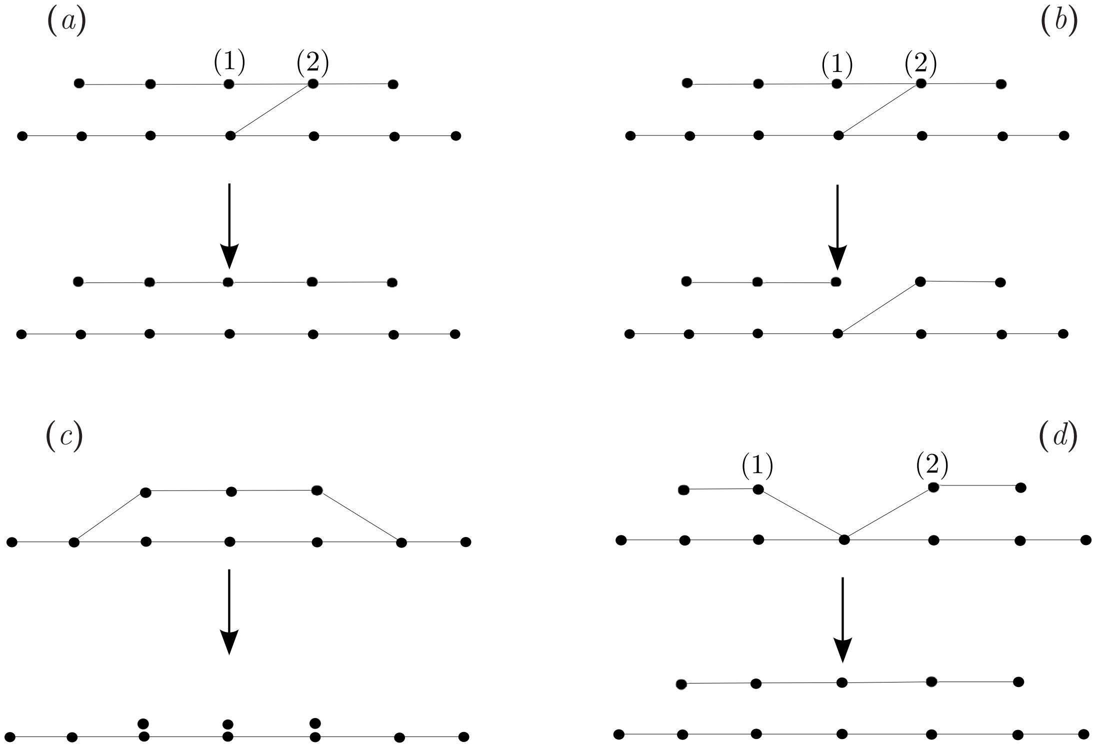

Figure 4.16: Sketches of the four types of connections corrected. For each graph, time is going from left to right. (*a*) Case I: two branches touch each other. The contact between them is dismissed. (*b*) Case II: two branches touch each other. One branch is disconnected in two. (*c*) Case III: a branch begins and ends at the same branch. Both of them are grouped into a single one. (*d*) Case IV: two branches are connected backward and forward with a third one at the same node. The two branches are disconnected and linked together to form a new one. See text for details of when the corrections are applied.

shifted by a distance $-U(y)\Delta t_s$ in the streamwise direction. This may lead to spurious connections, especially between small structures. Most of the results presented above were also computed without applying any shifting for case M950 and no important differences were observed. Some results are shown in table 4.5. Almost the same amount of branches and graphs are obtained, and the main consequence of removing the shifting is to increase the number of isolated structures, although their total volume remains negligible compared to the total volume of the non-isolated ones. The ratio of direct and inverse cascade, as will be defined in section 5.4, changes roughly by 3%.

4.A.2 Validation of the tracking method

In order to verify that the tracking method is properly working, graphs and branches extracted from the actual turbulent flow were visualized (see, for instance, figure 4.5a). In addition, three tests were performed with synthetic data. They are shown in figure 4.17 which also includes the corresponding graphs. The first test consists of three eddies moving in the streamwise direction with different advection velocities. The second test is an initial eddy that first splits into two fragments of different sizes, then, each of them split again following the same process, and finally all the objects merge in reverse order. The third test does not have any physical meaning and is intended to check rare connections. All the cases were correctly captured by the tracking method.

To discard any bias of the method related to the arrow of time, Q graphs and branches were computed with data from case M950 that were previously reversed in time. The results are shown in table 4.5. The same number of branches and graphs are obtained, and the role of mergers and splits is exchanged, as expected.

4.B Effect of the threshold and time step

Two new cases derived from M950 are defined to study the effect of the threshold and the time step between consecutive fields. The parameters are summarized in table 4.6. For case Ms950, the threshold H is almost doubled, and for case Mt950, the time step is increased roughly by a factor of four. All the results presented above were recomputed for cases Ms950 and Mt950, and no significant differences appeared. Some results are collected in figures 4.18(a,b,c,d) and table 4.6. The number of branches and graphs decreases for cases Ms950 and Mt950, although the total volume of isolated structures remains smaller than 0.01% with respect to the total volume of objects. The only remarkable change is a 10% increment of the ratio of direct and inverse cascade (see chapter 5) for intense Q^-s

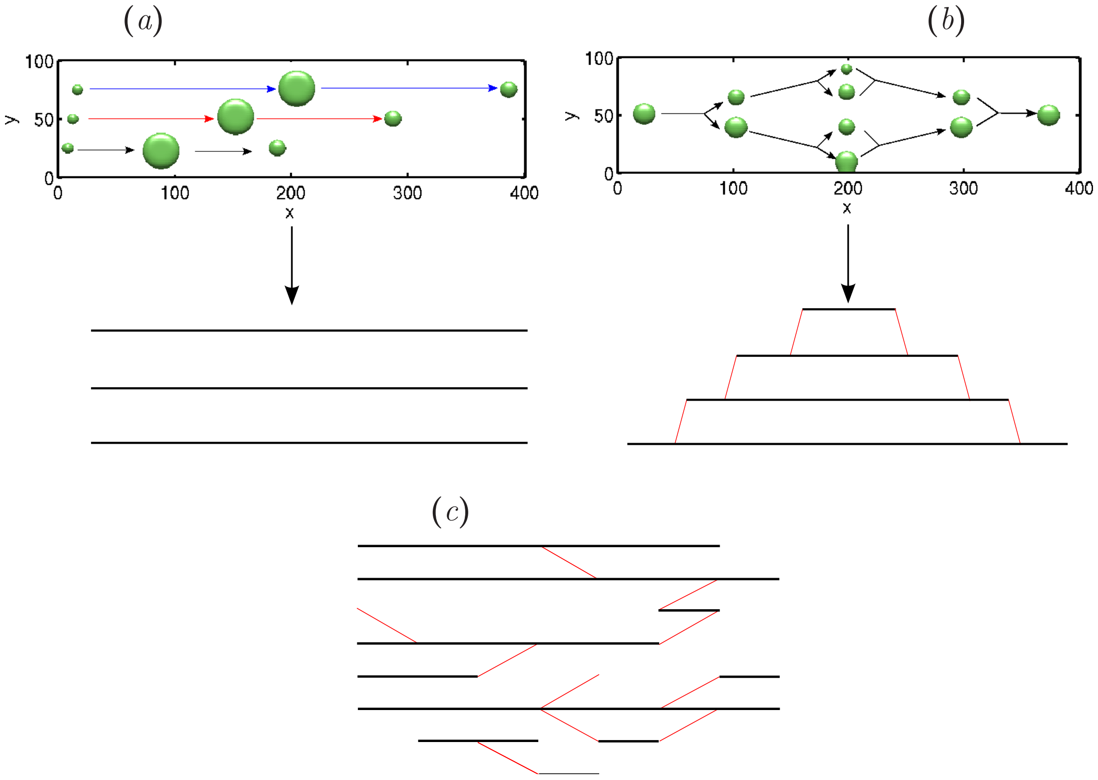

Figure 4.17: Synthetic test cases in arbitrary units. (*a*) Three objects moving with different advection velocities. (*b*) Objects splitting and merging. (*c*) Test with no physical meaning intended to check rare connections. For (*a*) and (*b*) the top figure shows the structures (in green) at different times (linked with arrows). The view is a x–y plane. The flow and time are going from left to right. The bottom part shows the corresponding graph with black lines for branches and red lines for mergers and splits. In case (*c*), only the graph is shown.

Case	N_B^Q	N_G^Q	N_S^Q	N_M^Q	N_I^Q	V_I^Q/V_T^Q	r_B
M950	3148888	1805427	570440	415147	153440	2.5×10^{-5}	1.21
M950 *time-reversed*	3148888	1805427	415147	570440	153440	2.5×10^{-5}	0.83
M950 *no shifting*	3154002	1825554	554322	398813	427059	1.6×10^{-4}	1.25

Table 4.5: N_B^Q, number of branches; N_G^Q, number of graphs; N_M^Q, number of mergers; N_S^Q, number of splits; N_I^Q, number of isolated structures; V_I^Q/V_T^Q, ratio of total volume occupied by isolated objects and volume of all the objects; r_B, ratio of direct and inverse cascade as defined in chapter 5. Data for Qs. The results presented in previous sections correspond to case M950. Case M950 *time-reversed* is case M950 with the arrow of time reversed. Case M950 *no shifting* is case M950 but without shifting the structures a distance $-U(y)\Delta t_s$ in the streamwise direction before computing their connections.

Case	H	Δt_s^+	N_B^Q	N_G^Q	N_I^Q	V_I^Q/V_T^Q	r_B	Symbol
M950	1.75	0.8	3.15	1.81	0.15	2.5×10^{-5}	1.21	none
Ms950	3.00	0.8	1.79	0.91	0.09	4.1×10^{-5}	1.32	□
Mt950	1.75	3.8	1.38	0.82	0.21	1.07×10^{-4}	1.24	×

Table 4.6: Summary of the parameters and results from case M950 and the sub-cases derived from from it. H, thresholding parameter; Δt_s, time step between consecutive fields; N_B^Q, number of branches; N_G^Q, number of graphs; N_I^Q, number of isolated structures. All numbers are in millions. V_I^Q/V_T^Q, ratio of total volume of isolated objects and volume of all the objects; r_B, ratio of direct and inverse cascade as defined chapter 5. Data for Qs.

with $H = 3$, compared to those computed with $H = 1.75$. Figure 4.18(a) shows that coarsening the time between consecutive fields does not affect the statistical trends of tall attached branches, and its effects are only visible for detached and buffer layer branches whose lifetimes are close to the time-resolution limit. Sizes and advection velocities are qualitatively similar. More thresholds were tested without any remarkable change for Qs defined within $1.25 < H < 3$. A similar analysis was performed for vortex clusters with no important differences for $0.01 < \alpha_t < 0.04$.

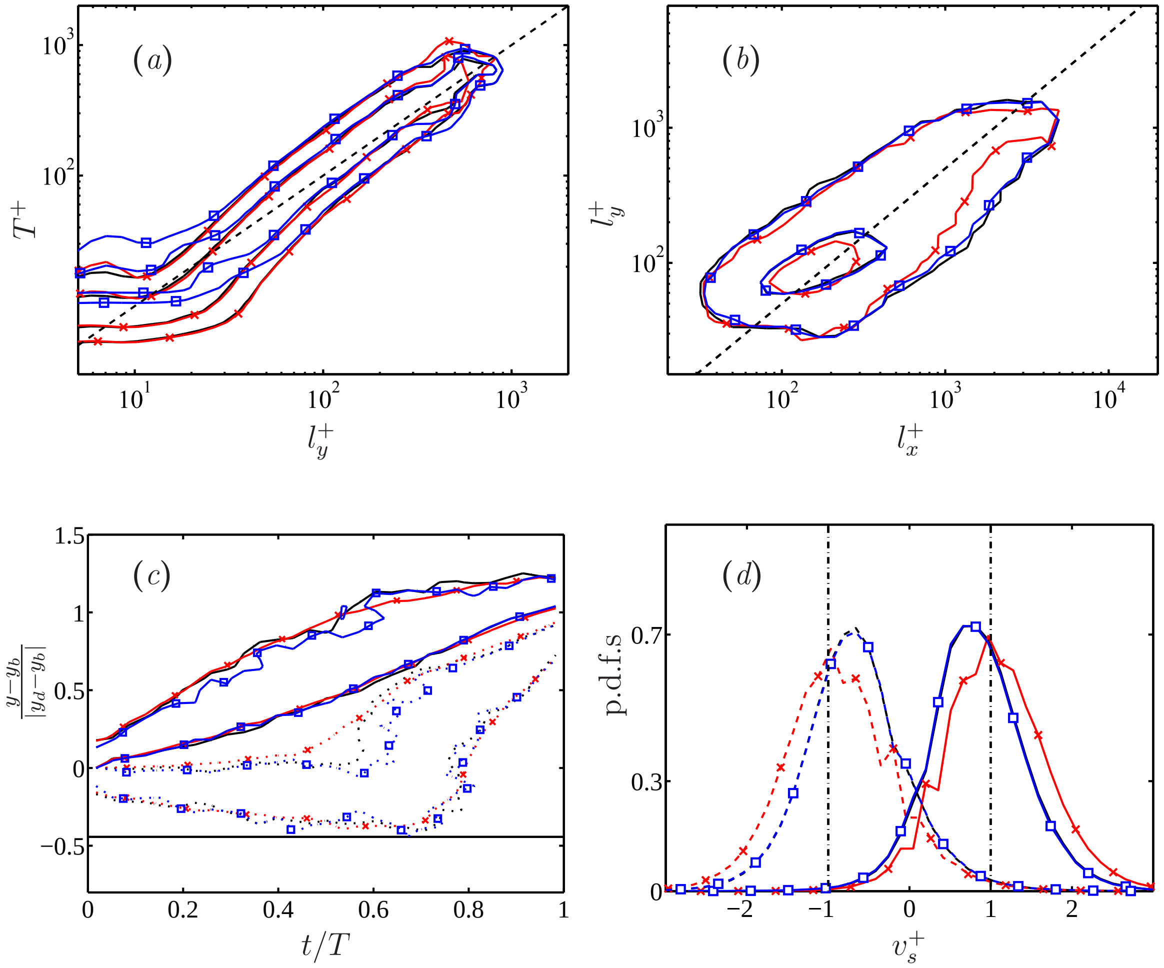

Figure 4.18: (*a*) P.d.f.s of the lifetimes of Q$^-$s primaries as a function of the wall-normal length of the branch, l_y. Each vertical section is a p.d.f.. Contours are 40% and 80% of the maximum. The straight dashed line is $T^+ = l_y^+$. (*b*) Joint p.d.f.s of the logarithm of the streamwise, l_x, and wall-normal, l_y, sizes of tall attached primaries. Data for ejections. The dashed straight line is $l_x = 2l_y$. Contours are 50% and 98% of the data. (*c*) P.d.f.s of the minimum (– – –) and maximum (——) heights of tall attached primary branches, as functions of the time elapsed from their birth. Time is normalized with the lifetime of each branch, T, and y_{min} and y_{max} with the heights, y_b and y_d, at its birth and death, respectively. The solid horizontal lines are the average position of the wall. (*d*) P.d.f.s of the wall-normal velocity of the center of gravity of sweeps (– – –) and ejections (——). The vertical dashed-dotted lines are $v_s = \pm u_\tau$. Symbols as in table 4.6.

Chapter 5

The turbulent cascade in terms of coherent structures [*]

5.1 Introduction

This last chapter is devoted to the turbulent cascade. The phenomenological explanation of the transfer of energy from large to small scales was introduced in the classical paper by Kolmogorov (1941*b*), but the concept of a turbulent cascade in terms of interactions among eddies had been proposed earlier by Richardson (1920), and later by Obukhov (1941). In the present chapter, we focus on the geometrical Richardson-Obukhov model of local-in-space cascade as opposed to the Kolmogorov local-in-scale one, and occasionally refer to the momentum cascade as described in Jiménez (2012). Also, it was shown in chapter 4 that the most important structures have sizes above the Corrsin scale and, hence, are influenced by the injection of energy from the mean shear. As a consequence, these structures are not intended to represent the isotropic energy transfer in the sense of Kolmogorov (1941*b*) but at most its first steps. There have been some attempts to reconcile the two different views described above, and to unravel the physical mechanism behind the cascade. In particular, it has been known for some time that the cascade is not one-directional from large to small scales, but that there is a balance between direct and inverse transfers. Most of the evidence for this backscatter originates from filtering techniques in scale space (Piomelli *et al.*, 1991; Aoyama *et al.*, 2005). Again, the physical details of the process remained unknown, and our goal will be to inquire whether individual structures can be observed to break or merge in ways that can be related to a cascade

---

[*] Part of the contents of this chapter have been published in the Journal of Fluid Mechanics, volume 759, pages 432–471, with Javier Jiménez as coauthor.

process.

The chapter is organized as follows. Section 5.2 studies the statistics of the secondary branches that were not included in the previous chapter. The definitions of a cascade of eddies are presented in §5.3, and section 5.4 describes the evidence for direct and inverse turbulent cascades in terms of coherent structures. Finally, the conclusions are presented in §5.5.

5.2 Secondary branches and graphs

The discussion in the previous chapter deals mostly with primary branches. Here we describe the behavior of the secondary branches that interact with them. The underlying goal is to describe, if possible, the inertial cascade as a spatially localized process in which individual eddies merge and split, as implied in the original descriptions by Richardson (1920) and Obukhov (1941), rather than simply as the conceptual scale-by-scale model introduced by Kolmogorov (1941*b*). Our tool will be the identification of such interactions within the organization of the structures into branches and graphs.

As discussed in §4.3, graphs are collections of branches that interact with each other at some point in their life. It is difficult to define unique descriptors for the geometry of the graphs, which can be quite complex objects (see figure 4.5*a*,*b*), but they can be classified in the same way as branches. For example, a graph is tall attached if that is the case for at least one of the structures in one of its branches. For the same reasons as in the case of structures and branches, graphs can be given a unique type. For example, a Q2 graph is exclusively formed by Q2 structures, and there are no mixed graphs.

Throughout the chapter we will use the same cases compiled in table 4.1. Figure 5.1 shows the normalized histogram of the number of branches per graph, and gives an idea of their complexity. The mode of the histogram is located at one branch per graph, but these cases correspond to simple small structures that evolve without splitting or merging. On the other hand, the tails of the histograms include large graphs with thousands of branches which represent groups of eddies (either Qs or clusters) that merge and split often, as in the example in figure 4.5(*a*).

Graphs are mostly made of primary, incoming and outgoing branches, with very few connectors (see the classification in figure 4.6 and the discussion in §4.3). When only incoming and outgoing branches are considered, the results obtained in previous sections are little affected for detached and buffer-layer branches, but those for tall attached ones change. Roughly 60-70% of the tall attached branches are secondary (either incoming or

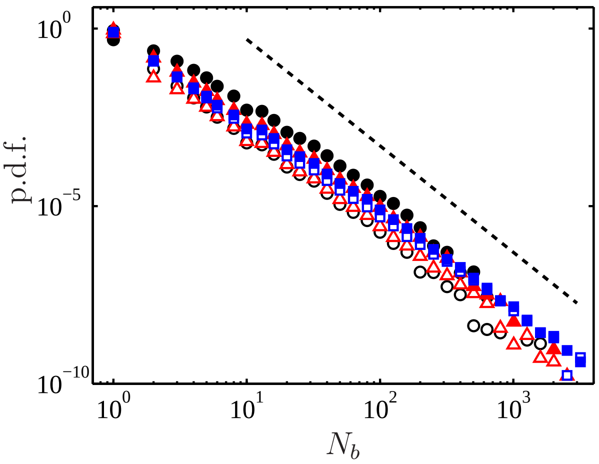

Figure 5.1: P.d.f.s of the number of branches per graph. Open symbols for Q^-s and closed ones for vortex clusters. Symbols as in table 4.1 with squares for case M4200. The dashed line is proportional to N_b^{-3}.

outgoing). Their evolutions are truncated versions of the tall attached primaries, with lifetimes biased towards shorter values and of the order of $l_y/(2u_\tau)$, which is half of that obtained for primaries. Their minimum and maximum wall distances (not shown) behave like the ones presented for primary branches in figures 4.11(*c*,*d*,*f*) but only until they interact (merge or split) with a primary. Hence, the equivalent plots for incoming branches are similar to the first half of figures 4.11(*c*,*d*,*f*) from $t/T = 0$ (when they are born) to $t/T \approx 0.5$ (when they merge with a primary), whereas the plots for outgoing branches resemble the second half, from $t/T \approx 0.5$ (when they split from a primary) to $t/T = 1$ (when they die).

5.3 Definition of a cascade of eddies

Figure 5.2 contains sketches of the two basic interactions among branches, and defines the notation for this section. Each elementary interaction involves three objects. Two of them, b for big and m for medium, are part of the main branch involved in the interaction, while the third one (s for small) is the fragment being lost or gained. Thus, in the split in figure 5.2(a), a structure of characteristic size Δ_b breaks into a fragment of size Δ_m, which continues the branch, and loses a fragment of size Δ_s. We will call this interaction a direct cascade event. Similarly, in the inverse cascade event in figure 5.2(b), two structures of sizes Δ_m and Δ_s merge into a single one of size Δ_b. In both cases, the notation is $(b) \rightleftharpoons (s) + (m)$. Usually, but not always, $\Delta_b > \Delta_m > \Delta_s$. Note that the sketches in

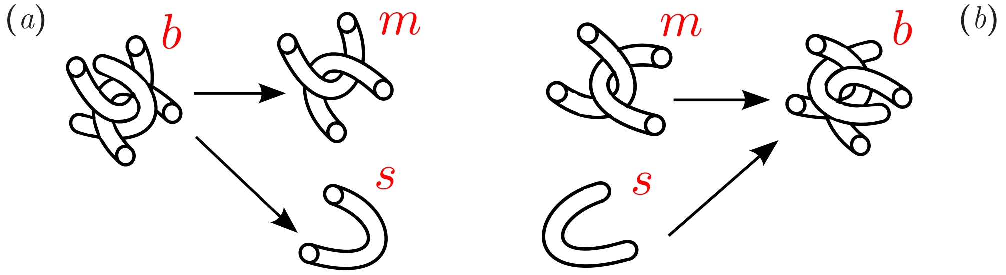

Figure 5.2: Sketch of the process of: (*a*) split or direct cascade, and (*b*) merge or inverse cascade. The structures labeled as b (big) and m (medium) belong to the same branch, and the one denoted by s (small) is the fragment that has split or merged.

figure 5.2 depict the merger or split of a single structure at a given moment, but that it is fairly common to find several mergers or splits, or a mixture of them, coinciding in a single event.

For the purpose of characterizing interactions, we use as eddy size the length, Δ, of the three-dimensional diagonal of its circumscribing box, which is, on average, 1.3 times larger than its streamwise length. This choice was preferred instead of other lengths based on the volume of the structures due to their complicated shapes (see, for example, figure 4.2). For that reason, the split of a structure in two fragments with similar characteristic lengths as defined above do not necessarily imply similar volumes. The length Δ can be generalized to branches by averaging over the branch life, $l = \langle \Delta \rangle_B$, as in §4.4. When normalizing it with the Kolmogorov scale, we use the channel average at the height of the center of gravity of the branch.

Also, since very few differences were found in the cascade statistics of sweeps and ejections, they are treated together for the rest of this chapter.

5.4 Results

We analyze first the prevalence of interactions. Figure 5.3(*a*) shows the fraction of primary vortex-cluster branches that split or merge at least once in their lives, as a function of their mean diagonal length. There is a minimum size, $l \approx 30\eta$, roughly agreeing with the peak of the energy-dissipation spectrum at $\lambda_x \approx 40\eta$ (Jiménez, 2012), below which branches rarely merge or split. In this range, the cascade is presumably inhibited by viscosity, and graphs contain a single branch that evolves without splitting or merging. On the other hand, almost all the branches larger than $l \approx 100\eta$, most of which are tall attached, merge or split at least once. In the transition between these two limits, the

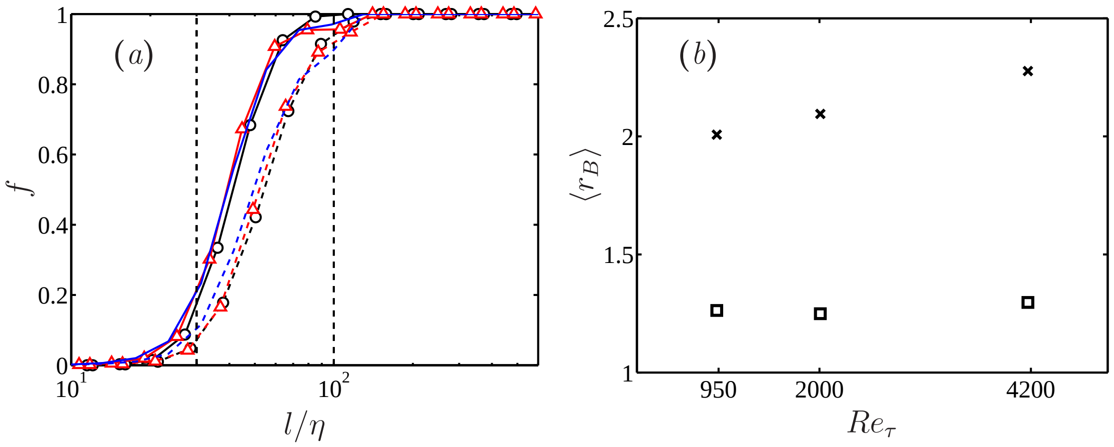

Figure 5.3: (a) Fraction, f, of the number of primary clusters branches that split (——) or merge (– – –) at least once in their lives, as a function of the mean diagonal length of the branch, l. The buffer layer branches are excluded. The vertical dashed lines are $l = 30\eta$ and $l = 100\eta$. Symbols as in table 4.1. (b) Ratio between the volume of direct and inverse cascade as a function of the Reynolds number. □, Q$^-$s; ×, vortex clusters.

direct cascade predominates, and some branches split but never merge. Similar results are obtained for Q$^-$s (not shown), although with less pronounced differences between the direct and the inverse cascades. The buffer layer branches are excluded from figure 5.3(a). They cascade very little and, when they are included in the figure, the cascading fractions increase more slowly and the curves move to the right, reaching unity at $l \approx 180\eta$.

Next, we characterize the part of the growth and decay of the structures that is due to mergers and splits, which can be interpreted as a measure of the contribution of the inverse and direct cascades to the eddy evolution. To do that, we compare the total volume gained or lost by primary branches in their cascade interactions with the average volume of the branch, V_b. For example, the total lost volume (direct cascade), $\sum_B V_{sd}$, is defined as the sum of the volumes of all the fragments lost during the life of the branch, with a similar definition for the volume gained, $\sum_B V_{si}$. Excluding the buffer layer branches, Q primaries with $l > 100\eta$ have on average $\sum_B V_{sd}/V_b \approx 0.72$ and $\sum_B V_{si}/V_b \approx 0.50$ for case M4200. For vortex clusters, the ratios are on average 1.41 and 0.73. In both cases mergers and splits are substantial contributors to the eddy growth and decay.

The ratio

$$r_B = \frac{\sum_B V_{sd}}{\sum_B V_{si}}, \tag{5.1}$$

gives an idea of which of the two cascades dominates in a given branch. Its average, $\langle r_B \rangle$, is plotted in figure 5.3(b) for different Reynolds numbers and branch types. The direct

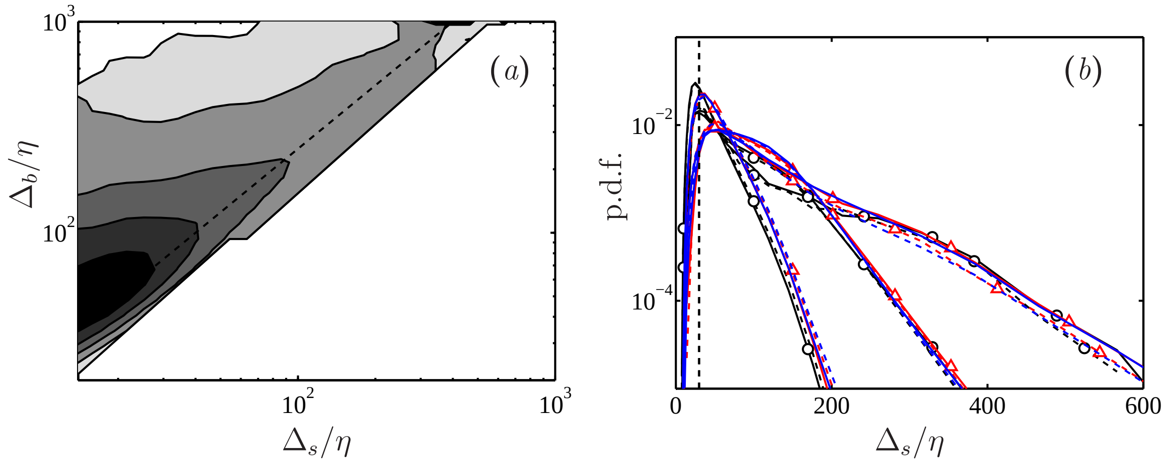

Figure 5.4: (a) Volume ratio between the direct and inverse cascades, as a function of the sizes of the smallest and largest fragments in a given interaction. Data for vortex clusters in M4200. The dashed line is $\Delta_s = 0.4\Delta_b$. Contours are, from dark to light, $3.5, 3, 2.5, 2$ and 1.2. (b) P.d.f.s of the sizes of the fragments merged (– – –) or split (——), Δ_s, for different lengths of the larger eddy involved, $\Delta_b/\eta = 0 - 200, 200 - 500, 500 - 2000$. Data for vortex clusters. The vertical dashed line is $\Delta_s = 30\eta$. Symbols as in table 4.1.

cascade always dominates, especially for vortex clusters, and its dominance increases slightly with the Reynolds number. However, the imbalance is not huge, approximately 1.3 for Q^-s, and 2.2 for vortex clusters, implying that the inverse cascade is not negligible, in accordance with the backscatter observations of Piomelli *et al.* (1991) and others.

To understand better how this imbalance is distributed as a function of scale, we decompose the ratio r_B in terms of the size of the fragments involved, r. Figure 5.4(a) shows the ratio $r(\Delta_s, \Delta_b)$, defined as in (5.1) but restricting the sums and the subsequent averaging to interactions involving a smallest and largest eddy of those sizes. The figure refers to vortex clusters in case M4200, but qualitatively similar ones are obtained for Q^-s and for vortex clusters at different Reynolds numbers.

The direct cascade always prevails, but the imbalance is strongest along a ridge $\Delta_s \approx 0.4\Delta_b$, which corresponds to eddies splitting roughly in halves, or merging with others of similar size. It is also strongest for small structures below $\Delta_b \approx 60\eta$, which tend to split in fragments of $\Delta_s \approx 20\eta$ much more frequently than they merge. This ridge can be interpreted as the preferred locus of a predominantly direct cascade, but note again that the imbalance for inertial structures is at most a factor of two, and that the cascade only really becomes unidirectional when one of the fragments is small enough to be dissipated by viscosity.

Figure 5.4(b) studies in more detail the merging or splitting process by presenting the p.d.f.s of the size of the smallest structure involved in an interaction for different ranges of the size of largest one. Most of the fragments are of the order of $\Delta_s \approx 30\eta$, corresponding to viscous fragments torn from larger eddies or merging into them. However, the tails of the p.d.f.s get longer as the largest structure gets bigger, representing inertial interactions between eddies of comparable sizes. Further analysis of the data (not shown) confirms this trend, and reveals that the size of the largest fragment likely to merge into, or split from, an eddy of size Δ_b is some fixed fraction of Δ_b. Note that the p.d.f.s in figure 5.4(*b*) are almost identical for mergers and splits, and that the previous discussion applies equally well for the direct as for the inverse cascade.

The temporal behavior of the two cascades is studied in figure 5.5. Figure 5.5(*a*) shows the average time, T_I, elapsed before a Q^- of size Δ_b splits into two similar fragments, or a Q^- of size Δ_m merges with another one of similar size (in both cases defined as $|\Delta_m - \Delta_s| < 0.1\Delta_m$). This time may be interpreted as characterizing the inertial cascade and it is defined as the time elapsed between the birth of a primary and its first roughly symmetrical split or merger at sizes Δ_b or Δ_m respectively. In the case of several such events in a single branch, we consider T_I as the time between two consecutive inertial interactions, with the sizes Δ_b and Δ_m belonging to the last one. The results show that $T_I^+ \approx 0.35\Delta_{m,b}^+$ for both merging and splitting, and a further analysis reveals that primaries with $l > 100\eta$ undergo two or three inertial events in its life, counting mergers and splits. In general, if we count any interaction regardless of its size, the average number of splits (or mergers) in a branch is $n \approx 10^{-4}(l/\eta)^2$ for primaries with $l > 100\eta$ and excluding the buffer layer branches.

Figure 5.5(*b*) shows that mergers and splits are asymmetrically distributed during the life of the branch. While splits happen at the end of the life, and contribute to tear the structure apart, mergers take place at the beginning, and enhance the early stages of the growth of the eddy. While the figure is drawn for Q^-s, similar results are obtained for vortex clusters.

Finally, the spatial organization of mergers and splits is studied in figure 5.7 by looking at the relative position of the center of gravity of the smallest fragment with respect to the intermediate one (see the sketch in figure 5.6). Figures 5.7(*a*,*b*) show results for Q^-s. Most of the mergers and splits take place in the streamwise direction. The structures merge predominantly with fragments below and ahead of them, presumably because taller and faster structures overtake smaller ones. The splits occur mostly in the tail of the structure or in its upper-front head. Since we saw in §4.5.4 that tall attached Q^-s are tilted forward by the shear, this distribution of splits seem to reflect the occasional tearing of their heads

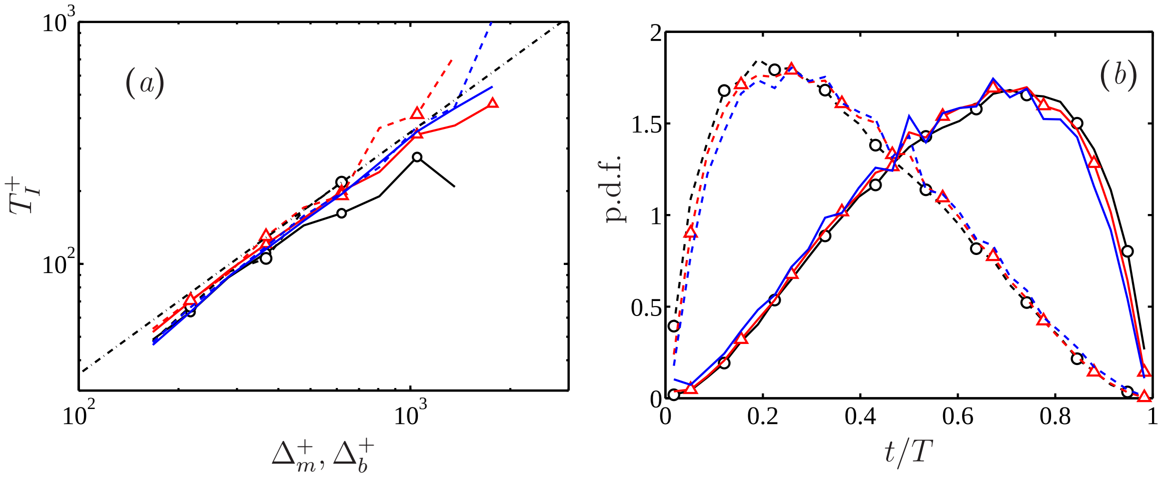

Figure 5.5: (*a*) Average time, T_I, for a Q^- to merge with, or split into, two fragments of similar size ($|\Delta_m - \Delta_s|/\Delta_m < 0.1$), plotted against Δ_m for mergers and Δ_b for splits. ——, splitting; – – –, merging. The dashed-dotted line is $T_I^+ = 0.35\Delta_{m,b}^+$. Data for primary branches. (*b*) P.d.f.s of the time at which mergers and splits take place, normalized with the branch lifetime. ——, splits, – – –, mergers. Primary tall attached Q^-s. Symbols as in table 4.1.

and tails during that process. The results for vortex clusters are not as interesting (figures 5.7*c*,*d*). Most of their interactions take place near the core of the original structure. The reason is probably that vortex clusters are much 'emptier' than Q^-s (see figure 4.2), and there is enough space within them for mergers and splits to happen internally.

With respect to the nature of the participants in an interaction, tall attached structures split 68% of the time into another tall attached structure and either a detached or a short attached one. In 25% of the interactions, neither of the resultant structures is tall attached, while only in 7% of the cases both of them are. Similar results are obtained for mergers and vortex clusters at different Reynolds numbers in this respect.

Taking the evidence in this section at face value, it is difficult not to think of the classical interpretation of the cascade by Leith (1967) or Orszag (1970), according to which the inertial energy transfer is an entropy-driven random process in phase space, in which energy tends to equipartition while drifting either up or down in scale (see the discussion in Lesieur, 1991, p. 295–305). It is only when viscosity breaks the energy conservation at the smallest scales that the energy is unidirectionally drained into heat. However, there are two important caveats.

The first one was already mentioned in the introduction. It should be clearly understood that most of the results in this section refer to the large scales in which energy is being fed into any possible inertial cascade. This should be clear from their associ-

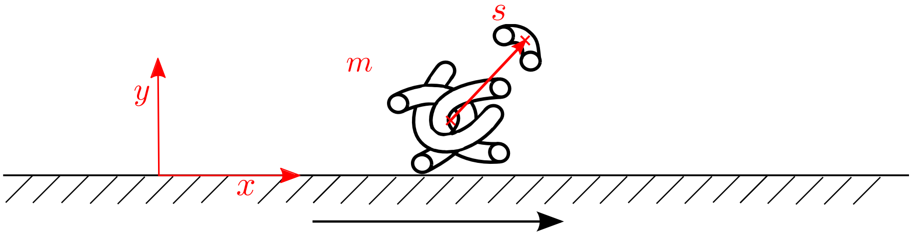

Figure 5.6: Sketch of the relative position of the center of gravity of fragments merged or split (structure s) with respect to the center of gravity of the medium eddy (structure m).

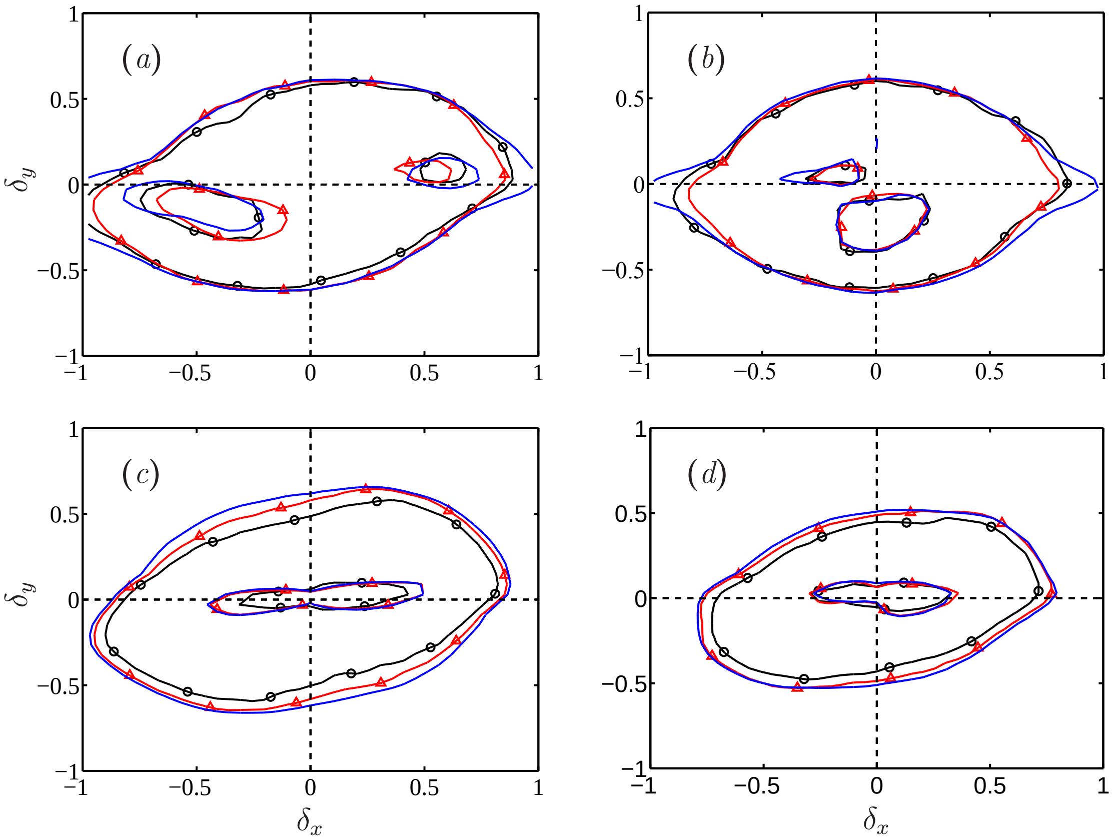

Figure 5.7: Joint p.d.f.s of the relative wall-normal and streamwise distances of the centers of mergers and splits (structures s) with respect to the center of the medium eddy (structure m) normalized with the characteristic size of the latter, l_m. See sketch in figure 5.6. Contours are 20%, and 90% of the data. (*a*) Splits for Q^-s. (*b*) Mergers for Q^-s. (*c*) Splits for vortex clusters. (*d*) Mergers for vortex clusters. Symbols as in table 4.1.

ation with the tangential Reynolds stress, and from the observation in figure 4.8 that the attached structures are larger that the Corrsin scale, and therefore directly coupled with the mean shear. As such, although the cascade process described in this section is probably a good description of how the momentum transfer changes scale across the logarithmic layer, it may not be representative of the behavior of the, presumably universal, Kolmogorov (1941*b*) inertial energy cascade.

In the second place, the description of a structure gaining fragments from its front (or back) while shedding them from the other end, could be interpreted as the definition of a dispersive wave packet, and it was shown in §4.5.4 that the bottom part of the attached structures is dispersive. To test whether this could be a simpler interpretation of the 'reversible' cascade described here, the objects from case M2000 were recomputed and tracked again after discarding all the planes for which $y^+ < 100$. It follows from figure 4.15(*d*) that structures above that level are mostly non-dispersive. The results in this section were then recalculated. The new structures were indeed different from those including the buffer layer. For example, the average structure size decreased somewhat, reflecting the loss of connectivity through the buffer layer, but no qualitative differences were found for the cascade statistics described here.

5.5 Conclusions

In this chapter we have studied the turbulent cascade in terms of coherent structures. It was found that the interactions (merging and splitting) among branches constitute a substantial part of their evolution, and could not be neglected. We have analyzed them as indicators of a cascade of the quantities carried by the structures involved; in this case, the wall-normal momentum transfer by the sweeps and ejections, and the enstrophy by the vortex clusters, even if the latter quantity is not conserved as is the former. Following the geometrical model proposed by Richardson (1920) and Obukhov (1941) in which cascading structures are related locally in space, mergers were taken to indicate an inverse cascade, from smaller to larger sizes, and splits to represent a direct one, from large to small. This process does not necessarily coincide with the energy cascade proposed by Kolmogorov (1941*b*), which is local in scale. The resulting picture is more complex than a simple direct cascade of large eddies into small ones. Eddies smaller than about 30η were found to cascade only rarely, while those larger than 100η, almost always do. In those cases, the total volume gained and lost was found to be a substantial fraction of the total volume of the large structures. Most branch interactions were found to be the shedding or absorption of Kolmogorov-scale fragments by larger structures, but more balanced splits or mergers spanning a wide range of scales were also found to be important. Not surprisingly, mergers are more common during the initial growth part of the evolution of the structures, while splits predominate later in their life, but the contributions from both directions of the cascade are surprisingly balanced. Only those involving small viscous fragments can be described as essentially unidirectional (direct). A typical large attached eddy cascades into comparable fragments two or three times during its life.

The location of the mergers and splits with respect to the largest eddy involved in the interaction was also investigated. New small structures in that region are accreted at the front of the structure, and shed from behind. This was interpreted to be the individual-structure counterpart of the classical active-inactive organization proposed by Townsend (1976). Large attached momentum structures, which can be roughly described as forward-leaning, add fragments from below, probably by overtaking them, and lose them from their upper head and their lower back, probably by shearing. Clusters, which are more disorganized, and with an emptier interior space, tend to cascade from the inside. These behaviors persist even when the buffer layer is discarded from the identification and tracking of individual structures.

Chapter 6

Conclusions and future work

In the present thesis, we have investigated the multiscale dynamics of the logarithmic layer of wall-bounded turbulent flows in terms of three-dimensional time-resolved coherent structures. The main contributions are a novel method to track in time coherent structures and a new structural model of the logarithmic layer based on vortex clusters, sweeps, ejections and streaks, which have been spatially and temporally scrutinized with a degree of detail never achieved before.

The raw data used as starting point, presented in chapter 2, are a set of new time-resolved DNSs of plane turbulent channels with periodic boundaries at $Re_\tau = 932$, 2009 and 4179, in moderate computational domains with streamwise and spanwise sizes of $L_x = 2\pi h$ and $L_z = \pi h$, respectively, where h is the channel half-height. New and previous simulations were used to asses the effect of the domain size on the large scales at all wall-normal distances. We have shown that these moderate domains are large enough to produce one-point statistics of the velocity and pressure fluctuations identical to those obtained in larger domains, suggesting that the infinitely long structures contained in these smaller boxes capture most of the dynamics of the larger ones, or at least of their interactions with scales of sizes up to $O(h)$. This finding is of utmost importance since it justifies the use of moderate boxes to study the dynamics of the logarithmic layer, making the analysis feasible from a computational point of view.

Results from the highest Reynolds number case, $Re_\tau = 4179$, continue the trends observed in previous simulations at lower Re_τ, such as the growth with Re_τ of the near-wall peak of the mean-squared streamwise velocity fluctuations. It also shows an incipient logarithmic region of the mean velocity profile with a Kármán constant $\kappa \approx 0.38$, but no logarithmic range was found for u'^2, in contrast with the clear ones observed for w'^2 and p'^2. We also introduced a new DNS in a very large domain with $L_x = 60\pi h$ and

$L_z = 6\pi h$ at $Re_\tau = 547$, and showed that the largest structures in a turbulent channel attain streamwise sizes of the order of $\lambda_x \approx 100h$ based on the contour of the streamwise velocity spectrum which contains roughly 80% of the streamwise turbulent kinetic energy.

In chapter 3, the quadrant analysis of the intense tangential Reynolds stress in plane turbulent channels was generalized to three-dimensional structures (Qs), with special emphasis on the logarithmic and outer layers. The structures were classified as outward interactions (Q1), ejections (Q2), inward interactions (Q3), and sweeps (Q4). The results suggest a separation of these structures into wall-attached and wall-detached families.

Wall-detached Qs are background stress fluctuations and their contributions to the mean Reynolds stress cancel. Although they span a wide range of scales, from the Kolmogorov to the integral length, most of them are small and isotropically oriented, with sizes of the order of a few Kolmogorov lengths. On the contrary, wall-attached structures are larger and carry most of the mean stress. These structures, predominantly ejections and sweeps, are responsible for roughly 60% of the total Reynolds stresses, but only fill 8% of the volume of the channel at the identification threshold used. They form a family of roughly self-similar objects with sizes $\Delta_x \approx 3\Delta_y$ and $\Delta_z \approx \Delta_y$, and become increasingly complex away from the wall.

The self-similar relations above do not hold for very large Qs. These structures, mostly ejections, extend into the opposite half of the channel across the central plane, and are responsible for 60% of the total volume of the attached Q^-s, and hence, of a substantial fraction of the mean stress. Their streamwise and spanwise lengths are of the order of $20h$ and $2h$, respectively, the same as the very-large-scale structures discussed by several authors. They are visually composite objects, formed by the concatenation of smaller subunits, and do not form part of the self-similar family mentioned above.

From a geometric point of view, Qs can be described as 'sponges of flakes', while vortex clusters are 'sponges of strings', in both cases with a thickness of their shells around 10–15 times the Kolmogorov length. Individual Qs have fractal dimensions of the order of $D_f = 2$, slightly fuller than the clusters, $D_f = 1.7$, and their associated genus density, i.e., number of holes per unit volume, is constant when scaled in Kolmogorov units, suggesting that large attached structures may be formed by smaller Kolmogorov objects similar to the detached ones.

The predominant logarithmic-layer structure is a side-by-side pair (rather than trio) of a sweep and an ejection. Most vortex clusters are associated with at least one Q2, although the converse is not true, and the clusters do not extend as far as the Qs into the logarithmic layer. These Q2-Q4 pairs have self-similar sizes, $\Delta_x \approx 4\Delta_y$ and $\Delta_z \approx 1.5\Delta_y$, and share dimensions and stresses with the conjectured attached eddies of Townsend (1976). Their constituent eddies tend to be aligned streamwise from each other, located near the sidewalls between the low- and high-velocity large-scale streaks, but that organization does not extend far enough to explain the very large structures discussed above.

In chapter 4, a novel approach to the study of the kinematics and dynamics of turbulent flows was presented. The method involves tracking in time coherent structures, and provides all the information required to characterize eddies from birth to death. The spatially and temporally well-resolved DNSs presented in chapter 2 were used to analyze the evolution of several millions of three-dimensional sweeps, ejections and clusters of vortices studied in chapter 3 for instantaneous realizations. The tracking procedure resulted in the organization of the structures in graphs, sub-organized again into primary branches, representing each the full evolution of a single structure, and a complicated set of secondary branches that either merge into, or split from them.

The results show that most of the eddies remain small and do not last for long times, but that some become large, attach to the wall, and extend across the logarithmic layer. The latter group contains the wall-attached structures discussed in chapter 3, and are geometrically and temporally self-similar, with lifetimes proportional to their size (or distance from the wall). This was true for sweeps, ejections and vortex clusters, and it is noteworthy that branches of sweeps and ejections were found to be essentially mirror images of each other. Both have essentially identical lifetimes and sizes, and their vertical advection velocities are antisymmetric: $+u_\tau$ for the ejections, and $-u_\tau$ for the sweeps. Moreover, ejections are born near the wall and rise until they disappear near their maximum height, and sweeps are born away from the wall and move towards it. The symmetry found between sweeps and ejections supports the idea that they are not independent structures, but different manifestations of larger quasi-streamwise rollers in which they are embedded. This reinforces the results in chapter 3, where it was observed that sweeps and ejections tend to appear in pairs.

Large wall-attached eddies were shown to have sizes above the Corrsin' scale and their dynamics to be controlled by the mean shear near their center of gravity. The results suggest that they are not necessarily created near the wall, but are rather a general consequence of the mean shear itself. On the other hand, detached structures are much smaller than the tall attached ones and have sizes and lifetimes of the order of the local Kolmogorov scales.

New structures form predominantly ahead or behind structures of the same kind, and that process was found to be consistent with side-by-side pairs of sweeps and ejections triggering new pairs of opposite polarity. A clockwise roller would thus follow a counter-clockwise one, and vice versa.

The streamwise advection velocity of individual structures was measured, and found to follow the mean velocity profile, $U(y)$. On average, ejections move slightly slower than $U(y)$, roughly by $-1.5u_\tau$, while sweeps move faster by the same amount. Vortex clusters can be either faster or slower than $U(y)$, although the latter is more probable, presumably reflecting their preferential association with ejections. The wall-normal dependence of the advection velocities implies that the structures are deformed enough by the mean shear that their lifetimes are controlled by that deformation, consistently again with a model in which tall attached eddies are created and eventually destroyed by their deformation by the mean velocity profile.

Finally, in chapter 5, spatially localized direct and inverse cascades were respectively associated with the processes of splitting and merging of individual structures, as in the geometric models of Richardson (1920) or Obukhov (1941). Eddies smaller than about 30η were found to cascade only rarely, probably because they are associated with viscous processes, while those larger than 100η, almost always do. In those cases, the total volume gained and lost was found to be a substantial fraction of the total volume of the large structures. It was found that the direct cascade predominates, but that both directions are roughly comparable. Most of the merged or split fragments have sizes of the order of a few Kolmogorov viscous units, but a substantial fraction of the growth and decay of the larger eddies is due to a self-similar inertial process in which eddies merge and split in fragments spanning a wide range of scales, including fragments comparable to the sizes of the eddies themselves.

In summary, the structural model proposed for the logarithmic layer of wall-bounded flows consist of pairs of wall-attached sweeps and ejections located side-by-side, with self-similar sizes and lifetimes, and extending throughout the logarithmic layer. These sweeps and ejections are embedded in longer high- and low-velocity streaks, respectively, and are responsible for most of the wall-normal momentum transfer in the channel. The vortex clusters are embedded within the ejections, and are a consequence of the vertical advection of high vorticity close to the wall carried by the ejections. In this scenario, the dynamics of the eddies are controlled by the mean shear, S, and the importance of the wall is diminished and relegated to maintain S. Wall-attached structures are surrounded by detached structures of little dynamical relevance, with sizes and lifetimes of the order of the local Kolmogorov scales, and whose contribution to the mean stress cancel.

The model proposed above shares a few properties with the hairpin's packet paradigm

(Adrian, 2007) like being consistent with the logarithmic velocity profile and the self-similar nature of the structures involved. Nevertheless, the results reveal crucial differences that make the two models no longer compatible. The scenario proposed here is much more disorganized and the structures involved are complicated multiscale objects. If tall wall-attached vortex clusters are considered to be as markers for hairpin-like structures, most of them would be born close to the wall and rise. However, not all the attached structures appear at the wall. Sweeps are created further away from the wall and only later move towards it. Besides, the symmetries found between tall attached ejections and sweeps with heights well above the buffer layer (i.e., the evolution of their maximum and minimum wall distances, their wall-normal velocities, their grouping in pairs, their lifetimes and sizes, etc) diminish the importance of the wall as the main source of tall wall-attached eddies. Regarding the casual relations between hairpins and ejections, tall attached vortex clusters do not grow in the wall-normal direction as much as the ejections do, suggesting than the latter could not be the consequence of fluid pumped by hairpins' packets but rather their cause. Other differences are also worth mentioning, such as that the merging of our structures takes place mostly in the streamwise direction rather than in the spanwise one, as conjectured for hairpins.

Future works should explore the time-resolved evolution of coherent structures in different turbulent flows, such as in isotropic turbulence and homogeneous shear turbulence. The former, when compared with the present work, would pinpoint the key dynamical differences between flows with and without mean shear, while the latter is particularly interesting to understand shear turbulence in its purest expression, since is the most simple shear flow that allows to remove the trace of the wall. The other natural extension of the present work is its application to the very large scale motions reported for channels and pipes that could not be studied here at high Reynolds numbers owing to the current state-of-the-art in computing power and storage. Besides, the tracking method proposed may be used to analyze other flow quantities that are considered dynamically relevant as those related to the energy transfer, for instance, the sub-grid stress. In particular, the results presented here suggest that sweeps and ejections are just a partial manifestation of the same streamwise roller, and it would be interesting to investigate alternatives structures that group both of them into the same coherent object.

References

Acarlar, M. S & Smith, C. R 1987*a* A study of hairpin vortices in a laminar boundary layer. Part 1. Hairpin vortices generated by a hemisphere protuberance. *J. Fluid Mech.* **175**, 1–41.

Acarlar, M. S & Smith, C. R 1987*b* A study of hairpin vortices in a laminar boundary layer. Part 2. Hairpin vortices generated by fluid injection. *J. Fluid Mech.* **175**, 43–83.

Adrian, R. J 1991 Particle-imaging techniques for experimental fluid mechanics. *Annu. Rev. Fluid Mech.* **23** (1), 261–304.

Adrian, R. J 2005 Twenty years of particle image velocimetry. *Exp. Fluids* **39** (2), 159–169.

Adrian, R. J 2007 Hairpin vortex organization in wall turbulence. *Phys. Fluids* **19** (4), 041301.

Adrian, R. J, Meinhart, C. D & Tomkins, C. D 2000 Vortex organization in the outer region of the turbulent boundary layer. *J. Fluid Mech.* **422**, 1–54.

del Álamo, J. C & Jiménez, J 2003 Spectra of the very large anisotropic scales in turbulent channels. *Phys. Fluids* **15** (6), L41–L44.

del Álamo, J. C & Jiménez, J 2006 Linear energy amplification in turbulent channels. *J. Fluid Mech* **559**, 205–213.

del Álamo, J. C & Jiménez, J 2009 Estimation of turbulent convection velocities and corrections to Taylor's approximation. *J. Fluid Mech.* **640**, 5–26.

del Álamo, J. C, Jiménez, J, Zandonade, P & Moser, R. D 2004 Scaling of the energy spectra of turbulent channels. *J. Fluid Mech.* **500**, 135–144.

del Álamo, J. C, Jiménez, J, Zandonade, P & Moser, R. D 2006 Self-similar vortex clusters in the turbulent logarithmic region. *J. Fluid Mech.* **561**, 329–358.

Antonia, R. A & Atkinson, J. D 1973 High-order moments of Reynolds shear stress fluctuations in a turbulent boundary layer. *J. Fluid Mech.* **58**, 581–593.

Antonia, R. A, Bisset, D & Browne, L 1990 Effect of Reynolds number on the topology of the organized motion in a turbulent boundary layer. *J Fluid Mech* **213**, 267–286.

Antonia, R. A & Pearson, B. R 1999 Low-order velocity structure functions in relatively high Reynolds number turbulence. *Europhys. Lett.* **48**, 163–169.

Aoyama, T, Ishihara, T, Kaneda, Y, Yokokawa, M & Uno, A 2005 Statistics of energy transfer in high-resolution direct numerical simulation of turbulence in a periodic box. *J. Phys. Soc. Japan* **74**, 3202–3212.

Balakumar, B. J & Adrian, R. J 2007 Large- and very-large-scale motions in channel and boundary-layer flow. *Phil. Trans. R. Soc. A* **365**, 665–681.

Batchelor, G. K 1953 *The theory of homogeneous turbulence*. Cambridge U. Press.

Batchelor, G. K & Townsend, A. A 1949 The nature of turbulent motion at large wave numbers. *Proc. R. Soc. London A* **199**, 513 – 520.

Bermejo-Moreno, I & Pullin, D. I 2008 On the non-local geometry of turbulence. *J. Fluid Mech.* **603**, 101–135.

Bernard, P. S 2013 Vortex dynamics in transitional and turbulent boundary layers. *AIAA Journal* **51** (8), 1828–1842.

Blackburn, H. M, Mansour, N. N & Cantwell, B. J 1996 Topology of fine-scale motions in turbulent channel flow. *J. Fluid Mech* **310**, 269–292.

Blackwelder, R. F & Kaplan, R. E 1976 On the wall structure of the turbulent boundary layer. *J. Fluid Mech.* **76**, 89–112.

Bogard, D. G & Tiederman, W. G 1986 Burst detection with single-point velocity measurements. *J. Fluid Mech.* **162**, 389–413.

Boussinesq, J 1877 Essai sur la théorie des eaux courantes. *Mem. de L'Académie des Sciences* **23**.

Bradshaw, P 1967 Inactive motions and pressure fluctuations in turbulent boundary layers. *J. Fluid Mech.* **30**, 241–258.

Brown, G. L & Roshko, A 1974 On density effects and large structure in turbulent mixing layers. *J. Fluid Mech.* **64**, 775–816.

Cadot, O, Douady, S & Couder, Y 1995 Characterization of the low-pressure filaments in a three-dimensional turbulent shear flow. *Phys. Fluids* **7** (3), 630–646.

Chong, M. S, Perry, A. E & Cantwell, B. J 1990 A general classification of three-dimensional flow fields. *Phys. Fluids* **2** (5), 765–777.

Chong, M. S, Soria, J, Perry, A, Chacin, J, Cantwell, B & Na, Y 1998 Turbulence structures of wall-bounded shear flows found using dns data. *J Fluid Mech* **357**, 225–247.

Christensen, K. T & Adrian, R. J 2000 Statistical evidence of hairpin vortex packets in wall turbulence. *J. Fluid Mech.* **431**, 433–443.

Cimarelli, A, de Angelis, E & Casciola, C. M 2013 Paths of energy in turbulent channel flows. *J. Fluid Mech.* **715**, 436–451.

Corino, E. R & Brodkey, R. S 1969 A visual investigation of the wall region in turbulent flow. *J. Fluid Mech.* **37**, 1–30.

Corrsin, S 1958 Local isotropy in turbulent shear flow. Res. Memo 58B11. NACA.

Darcy, H 1857 *Recherches expérimentales relatives au mouvement de l'eau dans les tuyeaux*. Mallet-Bachelier, Paris.

Deardorff, J. W 1970 A numerical study of three-dimensional turbulent channel flow at large Reynolds numbers. *J. Fluid Mech.* **41**, 453.

Dennis, D. J. C & Nickels, T. B 2011*a* Experimental measurement of large-scale three-dimensional structures in a turbulent boundary layer. Part 1. Vortex packets. *J. Fluid Mech.* **673**, 180–217.

Dennis, D. J. C & Nickels, T. B 2011*b* Experimental measurement of large-scale three-dimensional structures in a turbulent boundary layer. Part 2. Long structures. *J. Fluid Mech.* **673**, 218–244.

Elsinga, G. E & Marusic, I 2010 Evolution and lifetimes of flow topology in a turbulent boundary layer. *Phys. Fluids* **22** (1), 015102.

Elsinga, G. E, Poelma, C, Schröder, A, Geisler, R, Scarano, F & Westerweel, J 2012 Tracking of vortices in a turbulent boundary layer. *J. Fluid Mech.* **697**, 273–295.

Flores, O & Jiménez, J 2010*a* Hierarchy of minimal flow units in the logarithmic layer. *Phys. Fluids* **22** (7), 071704.

Flores, O & Jiménez, J 2010*b* Log-layer dynamics in smooth and artificially rough turbulent channels. In *IUTAM Symp. Phys. of Turbulence over Rough Walls* (ed. T.B. Nickels), pp. 93–98. Springer.

Flores, O, Jiménez, J & del Álamo, J. C 2007 Vorticity organization in the outer layer of turbulent channels with disturbed walls. *J. Fluid Mech.* **591**, 145–154.

Frisch, U 1995 *Turbulence*. Cambridge U. Press.

Frisch, U, Sulem, P & Nelkin, M 1978 A simple dynamical model of intermittent fully developed turbulence. *J. Fluid Mech.* **87**, 719 – 736.

Ganapathisubramani, B 2008 Statistical structure of momentum sources and sinks in the outer region of a turbulent boundary layer. *J Fluid Mech* **606**, 225–237.

Ganapathisubramani, B, Longmire, E. K & Marusic, I 2003 Characteristics of vortex packets in turbulent boundary layers. *J Fluid Mech* **478**, 33–46.

Guala, M, Hommema, S. E & Adrian, R. J 2006 Large-scale and very-large-scale motions in turbulent pipe flow. *J. Fluid Mech.* **554**, 521–542.

Guezennec, Y. G, Piomelli, U & Kim, J 1989 On the shape and dynamics of wall structures in turbulent channel flow. *Phys. Fluids* **1** (4), 764–766.

Hagen, G 1839 Über die Bewegung des Wassers in engen cylindrischen Röhren. *Poggendorfs Ann. Physik Chemie* **16**.

Hagen, G 1854 Über den Einfluss der Temperatur auf die Bewegung des Wassers in Röhren. *Math. Abh. Akad. Wiss Berlin* **17**, 17 – 98.

Haidari, A. H & Smith, C. R 1994 The generation and regeneration of single hairpin vortices. *J. Fluid Mech.* **277**, 135–162.

HEAD, M. R & BANDYOPADHYAY, P 1981 New aspects of turbulent boundary-layer structure. *J. Fluid Mech.* **107**, 297–338.

HOYAS, S & JIMÉNEZ, J 2006 Scaling of the velocity fluctuations in turbulent channels up to $Re_\tau = 2003$. *Phys. Fluids* **18** (1), 011702.

HOYAS, S & JIMÉNEZ, J 2008 Reynolds number effects on the Reynolds-stress budgets in turbulent channels. *Phys. Fluids* **20** (10), 101511.

HULTMARK, M, VALLIKIVI, M, BAILEY, S. C. C & SMITS, A. J 2012 Turbulent pipe flow at extreme Reynolds numbers. *Phys. Rev. Lett.* **108**, 094501.

HUTCHINS, N & MARUSIC, I 2007*a* Evidence of very long meandering features in the logarithmic region of turbulent boundary layers. *J. Fluid Mech.* **579**, 1–28.

HUTCHINS, N & MARUSIC, I 2007*b* Large-scale influences in near-wall turbulence. *Phil. Trans. Roy. Soc. A* **365**, 647–664.

HUTCHINS, N, MONTY, J. P, GANAPATHISUBRAMANI, B, NG, H. C. H & MARUSIC, I 2011 Three-dimensional conditional structure of a high-Reynolds-number turbulent boundary layer. *J. Fluid Mech.* **673**, 255–285.

JIMÉNEZ, J 1998 The largest scales of turbulence. In *CTR Ann. Res. Briefs*, pp. 137–154. Stanford Univ.

JIMÉNEZ, J 2000 Turbulence. In *Perspectives in Fluid Dynamics* (ed. G. K. Batchelor, H. K. Moffat & M. G. Worster), pp. 231 – 288. Cambridge U. Press.

JIMÉNEZ, J 2012 Cascades in wall-bounded turbulence. *Annu. Rev. Fluid Mech.* **44**, 27–45.

JIMÉNEZ, J 2013 How linear is wall-bounded turbulence? *Phys. Fluids* **25**, 110814.

JIMÉNEZ, J, DEL ÁLAMO, J. C & FLORES, O 2004 The large-scale dynamics of near-wall turbulence. *J. Fluid Mech.* **505**, 179–199.

JIMÉNEZ, J & HOYAS, S 2008 Turbulent fluctuations above the buffer layer of wall-bounded flows. *J. Fluid Mech.* **611**, 215–236.

JIMÉNEZ, J, HOYAS, S, SIMENS, M. P & MIZUNO, Y 2010 Turbulent boundary layers and channels at moderate Reynolds numbers. *J. Fluid Mech.* **657**, 335–360.

Jiménez, J, Kawahara, G, Simens, M. P, Nagata, M & Shiba, M 2005 Characterization of near-wall turbulence in terms of equilibrium and bursting solutions. *Phys. Fluids* **17** (1), 015105.

Jiménez, J & Moin, P 1991 The minimal flow unit in near-wall turbulence. *J. Fluid Mech.* **225**, 213–240.

Jiménez, J & Pinelli, A 1999 The autonomous cycle of near-wall turbulence. *J. Fluid Mech.* **389**, 335–359.

Jiménez, J & Wray, A. A 1998 On the characteristics of vortex filaments in isotropic turbulence. *J. Fluid Mech.* **373**, 255–285.

Jiménez, J, Wray, A. A, Saffman, P. G & Rogallo, R. S 1993 The structure of intense vorticity in isotropic turbulence. *J. Fluid Mech.* **255**, 65–90.

Johansson, A. V, Alfredsson, P. H & Kim, J 1991 Evolution and dynamics of shear-layer structures in near-wall turbulence. *J. Fluid Mech.* **224**, 579–599.

Kailas, S. V & Narasimha, R 1994 Similarity in vita-detected events in a nearly neutral atmospheric boundary layer. *Proc. Royal Soc. London, A* **447**, 211–222.

von Kármán, T 1930 Mechanische Ahnlichkeit und Turbulenz. In *Proceedings Third Int. Congr. Applied Mechanics, Stockholm*, pp. 85 – 105.

von Kármán, T & Howarth, L 1938 On the statistical theory of isotropic turbulence. *Proc. Royal Soc. London* **A 164**, 192 – 215.

Katul, G, Poggi, D, Cava, D & Finnigan, J 2006 The relative importance of ejections and sweeps to momentum transfer in the atmospheric boundary layer. *Bound. Layer Met.* **120** (3), 367–375.

Kawahara, G, Uhlmann, M & van Veen, L 2012 The significance of simple invariant solutions in turbulent flows. *Annu. Rev. Fluid Mech.* **44** (1), 203–225.

Kim, H. T, Kline, S. J & Reynolds, W. C 1971 The production of turbulence near a smooth wall in a turbulent boundary layer. *J. Fluid Mech.* **50**, 133–160.

Kim, J 1985 Turbulence structures associated with the bursting event. *Phys. Fluids* **28**, 52–58.

Kim, J & Hussain, F 1993 Propagation velocity of perturbations in turbulent channel flow. *Phys. Fluids* **5** (3), 695–706.

Kim, J, Moin, P & Moser, R. D 1987 Turbulence statistics in fully developed channel flow at low Reynolds number. *J. Fluid Mech* **177**, 133–166.

Kim, K & Adrian, R. J 1999 Very large-scale motion in the outer layer. *Phys. Fluids* **11** (2), 417–422.

Klewicki, J. C 2010 Reynolds number dependence, scaling, and dynamics of turbulent boundary layers. *J. Fluids Eng. Trans. ASME* **132** (094001).

Kline, S. J, Reynolds, W. C, Schraub, F. A & Runstadler, P. W 1967 The structure of turbulent boundary layers. *J. Fluid Mech.* **30**, 741–773.

Kolmogorov, A. N 1941*a* On degeneration of isotropic turbulence in an incompressible viscous liquid. In *Dokl. Akad. Nauk SSSR*, , vol. 31, pp. 538–540.

Kolmogorov, A. N 1941*b* The local structure of turbulence in incompressible viscous fluid for very large Reynolds' numbers. In *Dokl. Akad. Nauk SSSR*, , vol. 30, pp. 301–305.

Kolmogorov, A. N 1962 A refinement of previous hypotheses concerning the local structure of turbulence in a viscous incompressible fluid at high Reynolds number. *J. Fluid Mech.* **13**, 82–85.

Krogstad, P.-A, Kaspersen, J. H & Rimestad, S 1998 Convection velocities in a turbulent boundary layer. *Phys. Fluids* **10** (4), 949–957.

Kuglin, C. D & Hines, D. C 1975 The phase correlation image alignment method. *Proc. IEEE Int. Conf. on Cyber. and Soc.* pp. 163–165.

Lee, S.-H & Sung, H. J 2011 Very-large-scale motions in a turbulent boundary layer. *J. Fluid Mech.* **673**, 80–120.

LeHew, J, Guala, M & McKeon, B 2013 Time-resolved measurements of coherent structures in the turbulent boundary layer. *Experiments in Fluids* **54** (4), 1–16.

Leith, C. E 1967 Diffusion approximation to inertial energy transfer in isotropic turbulence. *Phys. Fluids* **10**, 1409–1416.

Lele, S. K 1992 Compact finite difference schemes with spectral-like resolution. *J. Comput. Phys.* **103** (1), 16 – 42.

Lesieur, M 1991 *Turbulence in fluids*, 2nd edn. Springer.

Lorenz, E. N 1963 Deterministic nonperiodic flow. *J. Atmos. Sci.* **20**, 130 – 141.

Lozano-Durán, A & Borrell, G 2015 An efficient algorithm to compute the genus of discrete surfaces and applications to turbulent flows. *ACM. Transaction on mathematical software.* –, (submitted).

Lozano-Durán, A, Flores, O & Jiménez, J 2012 The three-dimensional structure of momentum transfer in turbulent channels. *J. Fluid Mech.* **694**, 100–130.

Lozano-Durán, A & Jiménez, J 2010 Time-resolved evolution of the wall-bounded vorticity cascade. In *Proc. Div. Fluid Dyn.*, pp. EB–3. Am. Phys. Soc.

Lozano-Durán, A & Jiménez, J 2011 Time-resolved evolution of the wall-bounded vorticity cascade. *J. Phys. Conf. Series* **318** (6), 062016.

Lu, S. S & Willmarth, W. W 1973 Measurements of the structure of the Reynolds stress in a turbulent boundary layer. *J. Fluid Mech.* **60**, 481–511.

Martín, J, Ooi, A, Chong, M. S & Soria, J 1998 Dynamics of the velocity gradient tensor invariants in isotropic turbulence. *Phys. Fluids* **10** (9), 2336–2346.

Marusic, I 2001 On the role of large-scale structures in wall turbulence. *Phys. Fluids* **13** (3), 735–743.

Marusic, I, McKeon, B. J, Monkewitz, P. A, Nagib, H. M, Smits, A. J & Sreenivasan, K. R 2010 Wall-bounded turbulent flows at high Reynolds numbers: recent advances and key issues. *Phys. Fluids* **22** (6), 065103.

Marusic, I, Monty, J. P, Hultmark, M & Smits, A. J 2013 On the logarithmic region in wall turbulence. *J. Fluid Mech.* **716**, R3.

Mathis, R, Hutchins, N & Marusic, I 2009 Large-scale amplitude modulation of the small-scale structures in turbulent boundary layers. *J. Fluid Mech.* **628**, 311–337.

McComb, W. D 1990 *The physics of fluid turbulence*. Clarendon Press Oxford.

McKeon, B & Sreenivasan, K 2007 Introduction: scaling and structure in high Reynolds number wall-bounded flows. *Phil. Trans. R. Soc. London Ser. A* **365** (1852), 635–646.

Meinhart, C. D & Adrian, R. J 1995 On the existence of uniform momentum zones in a turbulent boundary layer. *Phys. Fluids* **7**, 694–696.

Metzger, M. M & Klewicki, J. C 2001 A comparative study of near-wall turbulence in high and low Reynolds number boundary layers. *Phys. Fluids* **13** (3), 692–701.

Millikan, C. B 1938 A critical discussion of turbulent flows in channels and circular tubes. In *Proceedings* 5^{th} *Int. Congr. Applied Mechanics, New York* (ed. J. P. Den Hartog & H. Peters), pp. 386 – 392. Wiley.

Mizuno, Y & Jiménez, J 2013 Wall turbulence without walls. *J. Fluid Mech.* **723**, 429–455.

Moisy, F & Jiménez, J 2004 Geometry and clustering of intense structures in isotropic turbulence. *J. Fluid Mech.* **513**, 111–133.

Monty, J. P, Stewart, J. A, Williams, R. C & Chong., M. S 2007 Large-scale features in turbulent pipe and channel flows. *J. Fluid Mech.* **589**, 147–156.

Nagasoa, R & Handler, R. A 2003 Statistical analysis of coherent vortices near a free surface in a fully developed turbulence. *Phys. Fluids* **15** (2), 375–135.

Nakagawa, H & Nezu, I 1977 Prediction of the contributions to the Reynolds stress from bursting events in open-channel flows. *J Fluid Mech* **80**, 99–128.

Narasimha, R, Kumar, S, Prabhu, A & Kailas, S. V 2007 Turbulent flux events in a nearly neutral atmospheric boundary layer. *Phil. Trans. Roy. Soc. A* **365** (1852), 841–858.

Nickels, T. B & Marusic, I 2001 On the different contributions of coherent structures to the spectra of a turbulent round jet and a turbulent boundary layer. *J. Fluid Mech.* **448**, 367–385.

Nikuradse, J 1932 Turbulente str omung in nichtkreisf ormigen rohren. *Forshg. Arb.* **Ing.–Wes**, 356.

Obukhov, A. M 1941 On the distribution of energy in the spectrum of turbulent flow. *Izv. Akad. Nauk USSR, Ser. Geogr. Geofiz.* **5** (4), 453–466.

Orszag, S. A 1970 Analytical theories of turbulence. *J. Fluid Mech.* **41**, 363–386.

Orszag, S. A & Patterson, G. S 1972 Numerical simulation of turbulence: statistical models and turbulence. *Lecture Notes in Physics* **12**, 127 – 147.

Panton, R. L 2001 Overview of the self-sustaining mechanisms of wall turbulence. *Prog. Aerosp. Sci.* **37** (4), 341 – 383.

Perry, A & Chong, M 1994 Topology of flow patterns in vortex motions and turbulence. *Appl. Sci. Res.* **53** (3-4), 357–374.

Perry, A. E & Chong, M. S 1982 On the mechanism of wall turbulence. *J. Fluid Mech.* **119**, 173–217.

Perry, A. E, Henbest, S & Chong, M. S 1986 A theoretical and experimental study of wall turbulence. *J. Fluid Mech.* **165**, 163–199.

Piomelli, U, Cabot, W. H, Moin, P & Lee, S 1991 Subgrid-scale backscatter in turbulent and transitional flows. *Phys. Fluids* **3** (7), 1766–1771.

Pirozzoli, S 2011 Flow organization near shear layers in turbulent wall-bounded flows. *J. Turbul.* p. N41.

Poincaré, H 1899 *Les Methodes Nouvelles de la Mécanique Celeste*. Gauthier Villars, Paris.

Poiseuille, J. L. M 1846 Recherches expérimentales sur le mouvement des liquides dans les tubes de très petits diamètres. *Mem. Acad. Sci. Paris* **9**, 433 – 545.

Pope, S. B 2000 *Turbulent flows*. Cambridge U. Press.

Prandtl, L 1925 Bericht über die Entstehung der Turbulenz. *Z. Angew. Math. Mech.* **5**, 136 – 139.

Raupach., M. R 1981 Conditional statistics of Reynolds stress in rough-wall and smooth-wall turbulent boundary layers. *J. Fluid Mech.* **108**, 363–382.

Reichardt, H 1951 Vollst andige Darstellung der Turbulenten Geschwindigkeitsverteilung in glatten Leitungen. *ZAMM* **31**, 208–219.

Reynolds, O 1894 On the dynamical theory of incompressible viscous fluids and the determination of the criterion. *Proc. London Math. Soc.* **56**, pp. 40–45.

Richardson, L. F 1920 The supply of energy from and to atmospheric eddies. *Proc. R. Soc. A,* **97** (686), pp. 354–373.

Robinson, S. K 1991 Coherent motions in the turbulent boundary layer. *Annu. Rev. Fluid Mech.* **23** (1), 601–639.

Rogers, M. M & Moin, P 1987 The structure of the vorticity field in homogeneous turbulent flows. *J. Fluid Mech.* **176**, 33–66.

Saddoughi, S. G & Veeravalli, S. V 1994 Local isotropy in turbulent boundary-layers at high Reynolds number. *J Fluid Mech* **268**, 333–372.

Schlatter, P, Li, Q, Örlü, R, Hussain, F & Henningson, D 2014 On the near-wall vortical structures at moderate reynolds numbers. *Eur. J. Mech. - B/Fluids* **48** (0), 75 – 93.

Schlatter, P & Örlü, R 2010 Assessment of direct numerical simulation data of turbulent boundary layers. *J. Fluid Mech.* **659**, 116–126.

Schlichting, H & Gersten, K 2000 *Boundary layer theory*, 8th edn. Springer.

Schoppa, W & Hussain, F 2002 Coherent structure generation in near-wall turbulence. *J. Fluid Mech.* **453**, 57–108.

Schultz, M. P & Flack, K. A 2013 Reynolds-number scaling of turbulent channel flow. *Phys. Fluids* **25** (2), 025104.

Sillero, J. A, Jiménez, J & Moser, R. D 2013 One-point statistics for turbulent wall-bounded flows at Reynolds numbers up to $\delta^+ \approx 2000$. *Phys. Fluids* **25** (10), 105102.

Singer, B. A & Joslin, R. D 1994 Metamorphosis of a hairpin vortex into a young turbulent spot. *Phys. Fluids* **6** (11), 3724–3736.

Smits, A. J, McKeon, B. J & Marusic, I 2011 High-Reynolds number wall turbulence. *Annu. Rev. Fluid Mech.* **43** (1), 353–375.

Spalart, P. R 1988 Direct simulation of a turbulent boundary layer up to $Re_\theta = 1410$. *J. Fluid Mech.* **187**, 61–98.

Spalart, P. R, Moser, R. D & Rogers, M. M 1991 Spectral methods for the Navier-Stokes equations with one infinite and two periodic directions. *J. Comput. Phys.* **96** (2), 297 – 324.

Suponitsky, V, Avital, E & Gaster, M 2005 On three-dimensionality and control of incompressible cavity flow. *Phys. Fluids* **17** (10), 104103.

Sutton, M. A, Wolters, W. J, Peters, W. H, Ranson, W. F & McNeill, S. R 1983 Determination of displacements using an improved digital correlation method. *Image Vision Comput.* **1** (3), 133–139.

Tanahashi, M, Kang, S, Miyamoto, T & Shiokawa, S 2004 Scaling law of fine scale eddies in turbulent channel flows up to $Re_\tau = 800$. *Int. J. Heat Fluid Flow* **25**, 331–341.

Taylor, G. I 1935 Statistical theory of turbulence. Parts I to IV. *Proc. Royal Soc. London* **A 151**, 421 – 478.

Taylor, G. I 1938 The spectrum of turbulence. *Proc. R. Soc. Lond.* **164**, 476–490.

Tennekes, H & Lumley, J. L 1972 *A first course on turbulence*. MIT Press.

Theodorsen, T 1952 Mechanism of turbulence. *Proc. 2nd Midwestern Conf. of Fluid Mechanics, Ohio State University.* .

Thompson, A. C 1996 *Minkowski geometry*, 1st edn. Cambridge: Cambridge University Press,.

Tomkins, C. D & Adrian, R. J 2003 Spanwise structure and scale growth in turbulent boundary layers. *J. Fluid Mech.* **490**, 37–74.

Townsend, A 1976 *The structure of turbulent shear flow*. Cambridge University Press.

Townsend, A. A 1961 Equilibrium layers and wall turbulence. *J. Fluid Mech.* **11**, 97–120.

Tuerke, F & Jiménez, J 2013 Simulations of turbulent channels with prescribed velocity profiles. *J. Fluid Mech* **723**, 587–603.

Van Atta, C. W & Wyngaard, J. C 1975 On higher-order spectra of turbulence. *J. Fluid Mech.* **72**, 673–694.

VILLERMAUX, E, SIXOU, B & GAGNE, Y 1995 Intense vortical structures in grid-generated turbulence. *Phys. Fluids* **7** (8), 2008–2013.

WALLACE, J. M, ECKELMANN, H & BRODKEY, R. S 1972 The wall region in turbulent shear flow. *J. Fluid Mech.* **54**, 39–48.

WARK, C. E & NAGIB, H. M 1991 Experimental investigation of coherent structures in turbulent boundary layers. *J Fluid Mech* **230**, 183–208.

WILLERT, C. E & GHARIB, M 1991 Digital particle image velocimetry. *Experiments in Fluids* **10**, 181–193.

WILLMARTH, W. W & LU, S. S 1972 Structure of the Reynolds stress near the wall. *J. Fluid Mech.* **55**, 65–92.

WILLS, J 1964 On convection velocities in turbulent shear flows. *J. Fluid Mech.* **20**, 417–432.

WU, X & MOIN, P 2010 Transitional and turbulent boundary layer with heat transfer. *Phys. Fluids.* **22**, 085105.

ZHOU, J, ADRIAN, R. J, BALACHANDAR, S & KENDALL, T. M 1999 Mechanisms for generating coherent packets of hairpin vortices in channel flow. *J. Fluid Mech.* **387**, 353–396.